# MATERIAL MODEL CALIBRATION OF FIBER REINFORCED CONCRETE USING DEEP NEURAL NETWORK

**A Thesis Submitted to**
**the Graduate School of**
**İzmir Institute of Technology**
**in Partial Fulfillment of the Requirements for the Degree of**

**DOCTOR OF PHILOSOPHY**

**in Civil Engineering**

**by**
**Yonca YAŞAYANLAR**

**July 2023**
**İZMİR**

We approve the thesis of **Yonca YAŞAYANLAR**

**Examining Committee Members:**

**Prof. Dr. Alper TAŞDEMİRCİ**
Department of Machine Engineering, İzmir Institute of Technology

**Prof. Dr. Engin AKTAŞ**
Department of Civil Engineering, İzmir Institute of Technology

**Asst. Prof. Dr. Selçuk SAATCI**
Department of Civil Engineering, İzmir Institute of Technology

**Assoc. Prof. Dr. İ. Serkan MISIR**
Department of Civil Engineering, Dokuz Eylül University

**Assoc. Prof. Dr. S. Can GİRGİN**
Department of Civil Engineering, Dokuz Eylül University

**14 July 2023**

**Asst. Prof. Dr. Selçuk SAATCI**
Supervisor,
Department of Civil Engineering
İzmir Institute of Technology

**Assoc. Prof. Dr. T. Kemal ERDEM**
Co-Supervisor,
Department of Civil Engineering
Marmara University

**Prof. Dr. Cemalettin DÖNMEZ**
Head of the Department of
Civil Engineering

**Prof. Dr. Mehtap EANES**
Dean of the Graduate School

# ACKNOWLEDGEMENTS

This doctoral dissertation contains a lot of hard work and many sleepless nights, and it would not have been possible without my advisor Asst. Prof. Dr. Selçuk Saatcı. I am beyond grateful for his guidance and support. He has always been very patient and reasonable with me while making sure I take the necessary steps to get where I am. He has been a great mentor during my PhD, as well as my master's degree.

I would also like to thank my thesis monitoring committee Prof. Dr. Engin Aktaş and Prof. Dr. Alper Taşdemirci. They were very generous with their contributions, time, and availability during my studies. Additionally, I would like to thank my defense jury Assoc. Prof. Dr. İ. Serkan Mısır and Assoc. Prof. Dr. S. Can Girgin for their valuable commentary and contributions to my thesis. I also would like to thank my co-advisor Assoc. Prof. Dr. T. Kemal Erdem for his support during my thesis study.

My appreciation goes to my professors and research colleagues at İYTE who were always dear to my heart for their support. Fellow graduates Bekir and Petek Kaçmaz especially have been there for me and have encouraged me during this stressful time.

I would also like to thank Sema and Ferit Arsan, my mother and father. I have been very fortunate to be their daughter and their support made all the difference during my academic journey. I also would like to thank my extended family, my mother-in-law Sema Yaşayanlar, and my brother-in-law Serkan Yaşayanlar for their invaluable support and encouragement.

Lastly, and more importantly, I would like to thank my husband and life partner, Süleyman. There aren't enough words to express my appreciation for his support and mentorship during this stressful journey. I love and appreciate you more than words.

# ABSTRACT


## MATERIAL MODEL CALIBRATION OF FIBER REINFORCED CONCRETE USING DEEP NEURAL NETWORK

The numerical modeling of fiber reinforced concrete (FRC) structures is quite challenging due to the material's heterogeneous and anisotropic nature. The majority of material models that are suitable for regular concrete are not able to account for the FRC material's increased tensile capacity and ductility. In this study, a calibration method is proposed that is simple and effective for modeling FRC structures using a selected concrete material model. The Karagozian and Case (K&C) material model in LS-DYNA is capable of representing the ductile nature of FRC, and its parameters related to tensile behavior were calibrated to reflect the tensile-softening behavior.

The calibration process was executed using the uniaxial direct tension test results of two different FRC mixtures. In addition, single element numerical models were constructed using LS-DYNA under uniaxial tension. The tensile parameters of K&C were varied over a wide range using single elements to form a database. Then, a Deep Neural Network (DNN) was constructed to pass the database through and find the K&C parameters that best matched the experimental uniaxial test results.

The proposed methodology was tested under static and high-strain rate loading conditions, and the results were compared to the experimental findings. The performance of the DNN-achieved parameters was found to be satisfactory. The results showed that the DNN-calibrated parameters were able to accurately predict the behavior of FRC structures under static and dynamic loading conditions.

# ÖZET

## DERİN SİNİR AĞI KULLANILARAK LİF TAKVİYELİ BETON MALZEME MODELİ KALİBRASYONU

Fiber takviyeli beton yapıların sayısal modellemesi, normal betona göre daha zordur. Normal beton için uygun olan malzeme modellerinin çoğu, fiber takviyeli beton malzemenin yüksek çekme kapasitesini ve arttırılmış sünek davranışını hesaba katamaz.

Bu çalışmada, fiber takviyeli beton yapılarının modellenmesi için basit ve etkili bir malzeme modeli kalibrasyon yöntemi önerilmiştir. Bunun için LS-DYNA'daki normal beton malzeme modeli olan Karagozian ve Case (K&C) malzeme modeli seçilmiştir. Fiber takviyeli betonun sünek doğasını yansıtabilecek çekme davranışıyla ilgili K&C parametreleri, çekme yumuşatması davranışını yansıtacak şekilde kalibre edilmiştir.

Kalibrasyon işlemi, iki farklı fiber takviyeli beton karışımının direk çekme testi sonuçları kullanılarak gerçekleştirilmiştir. Ayrıca, LS-DYNA ile direk çekme gerilimi altında tek eleman sayısal modelleri oluşturulmuştur. Bir veri tabanı oluşturmak amacı ile K&C'nin çekme parametreleri geniş bir aralıkta değiştirilmiştir. Veri tabanı, oluşturulan Derin Sinir Ağı'ndan geçirilip deneysel tek eksenli test sonuçlarına en iyi uyan K&C parametrelerini bulunmuştur.

Önerilen metodoloji statik ve yüksek şekil değiştirme yükleme koşulları altında test edilmiş ve sonuçlar deneysel bulgularla karşılaştırılmıştır. Derin Sinir Ağı tarafından elde edilen parametrelerin performansının kabul edilebilir olduğu bulunmuştur. Sonuçlar, Derin Sinir Ağı ile kalibre edilen parametrelerin, statik ve dinamik şekil değiştirme yükleme koşulları altında fiber takviyeli beton yapılarının davranışını doğru bir şekilde tahmin edebildiğini göstermiştir.

# TABLE OF CONTENTS

# LIST OF FIGURES

**Figure** **Page**

**Figure** **Page**

**Figure** **Page**

# LIST OF TABLES

**Table** **Page**

# CHAPTER 1

# INTRODUCTION

As a heterogeneous and anisotropic material, predicting the behavior of concrete has always been a challenge. Specifically, concrete's weaker and brittle behavior under tensile stresses makes the analytical and numerical modeling of concrete structures more difficult compared to ductile and isotropic materials such as metals. Despite these difficulties, there has been considerable progress in this area over the years. Numerous analytical and numerical methodologies were developed for modeling the behavior of reinforced concrete structures, some of which proved to be quite successful. However, a relatively new development in the industry posed a new challenge in this area. To improve the tensile behavior characteristics of reinforced concrete, the use of fibers, steel, natural or synthetic, started to gain popularity in concrete structures. Research at the material level in this area had gone a long way over the past two decades, and fiber reinforced concrete (FRC) is increasingly finding new application areas to improve the durability, ductility, and energy absorption capacity of reinforced concrete structures. On the other hand, numerical modeling of fiber reinforced concrete structures lacked behind those developments in the industry. The majority of the material models that were proved to be satisfactory for ordinary reinforced concrete were not suitable for direct inclusion of the increased tensile capacity and ductility of FRC. Hence, considerable new research was required to either develop new models or adapt existing models to include the characteristics of FRC.

Developing entirely new models for FRC is a challenging issue since the mechanical behavior of FRC varies considerably depending on fiber properties and proportions. The use of different types and ratios of fibers in the same concrete mix, called hybrid fiber reinforced concrete (HYFRC), even further complicates the problem, since this type of usage virtually yields infinite number of possibilities for the material. Therefore, manipulating existing concrete models by calibrating its parameters according to a specific FRC mix of interest can be considered a more practical way to model FRC structures. However, calibrating the parameters of a concrete model has its own challenges. Some concrete models may have certain numerical parameters that

were determined for ordinary concrete through experience and extensive experimental data collected over years of research, while others may require complicated testing systems to determine its parameters. Moreover, these concrete models may have several parameters that may require calibration, each of which may have a significant effect on the outcome. As a result, complicated and quite costly parameter determination efforts may be required for modeling FRC, which need to be repeated for every different FRC material.

In this study, a simpler and more effective calibration methodology is proposed for a selected concrete material model to model FRC structures. For this purpose, Karagozian and Case (Malvar et al., 1997) (K&C) concrete model, available in finite element software LS-DYNA, was selected. Parameters of K&C model directly related to the tensile behavior of concrete were calibrated to model the tension-softening behavior of FRC. To facilitate the calibration procedure, uniaxial direct tension test results of two different FRC mixes were used. A single element model was built in LS-DYNA and subjected to tensile stresses. Related tensile parameters were changed over a wide range and the tensile stress-displacement behavior of each model was obtained. Later, a Deep Neural Network (DNN) methodology was developed to obtain the most suitable parameter set that gives a tensile stress-displacement behavior that is closest to experimentally obtained ones through uniaxial tension tests. By this methodology, calibrated parameters were obtained using results obtained from a simple test method and a numerical analysis procedure that can be extensively automatized.

At the following stage of the study, parameter sets obtained through the mentioned parameter calibration procedure were employed in different structural elements under different loading conditions to test their applicability. Results of an experimental program conducted by Aloui (2020) were used to test the performance of the calibration procedure under static loading conditions. In this study, one-way FRC panels cast with the same mixes used for calibration were tested under four-point bending loads. These bending tests were modeled in LS-DYNA using K&C concrete model with parameters found from DNN calibration and results were compared with experimental results. To test the performance of the DNN calibrated parameters under high strain rate conditions, two-way panels tested under blast loads using a shock tube by Alkabbani (2021) were used. These panels were also modeled in LS-DYNA using K&C concrete model with parameters found from DNN calibration and obtained results were compared with experimental results. Through these studies, efficiency of this

calibration methodology was tested and verified for different FRC members under different loading scenarios.

Following chapter of this thesis presents a literature review outlining current practice in numerical modeling of FRC structures. In Chapter 3, the basic principles of used DNN methodology were presented along with the developed parameter calibration methodology of K&C concrete model for selected FRC mixes. Chapter 4 presents verification studies of the found parameter sets under static loading conditions, whereas Chapter 5 presents similar verification studies conducted for high strain rate conditions. Overall discussions and conclusions were presented in Chapter 6.

# CHAPTER 2

# LITERATURE REVIEW

## 2.1. Introduction

Fiber-induced concrete has a high tensile capacity under direct tension loading and can exhibit strain-hardening behavior under bending. The need for numerical investigation of these materials is usually met by performing large amounts of experimental tests to obtain a full numerical representation to write a new material model. Another method is to calibrate an existing material model that can represent this behavior; however, concrete materials are pressure sensitive, and experiments under varying pressures are required. With machine learning algorithms, material model calibration can be done without complex experimental testing. In this Chapter, a literature review regarding the material model used for fiber reinforced concrete, and the parameter search methodology with machine learning is presented. The numerical modeling of fiber reinforced concrete under high-strain loading conditions is investigated here as well.

## 2.2. Modeling FRC with Karagozian and Case Material Model

The FRC material improves tensile and flexural strength and increases energy absorption and impact resistance (Naaman and Reinhardt 2007; Martinelli, Caggiano, and Xargay 2015; Rahmani et al., 2012). The numerical simulation of fiber-reinforced concrete requires fracture properties (Farnam, Mohammadi, and Shekarchi 2010; Lin and Gravina 2017). To investigate this, researchers have generally used uniaxial tension, and four-point bending tests (Sorelli, Meda, and Plizzari 2005; Maalej et al., 2005; Li, Wang, and Wu 2001).

The Karagozian and Case (K&C) material model in LS-DYNA is a capable material model that can represent the ductile nature of FRC. The current version is the third release (Material 72 - Release III) of the Karagozian and Case material model and it has the ability to include strain-rate effects (Magallanes et al., 2010). Another

improvement made to the new release is to handle strain-softening without mesh dependency. Additionally, the K&C material model includes an automatic parameter generator that calculates the required parameters through interpolation given the compressive strength.

The K&C was explicitly developed for concrete material. Levi-Hevroni et al. (2018) used K&C for regular concrete but modified it with dynamic tension experimental tests. For that purpose, they have used a novel vertical tension split Hopkinson bar. L. Y. Xu, Xu, and Wen (2019) aimed to numerically represent the penetration and perforation of reinforced concrete targets using modified K&C. Experimental impact tests were conducted to determine the performance of the modified K&C material model. Additionally, the Holmquist Johnson Cook (HJC) concrete material model was used in the numerical modeling. The predicted impact crater sizes and residual projectile velocities were in agreement with the experimental findings for both numerical material models.

Some researchers selected to modify it to fit concrete-like material. Kucewicz et al. (2022) and Kucewicz et al. (2020) modified the material model to fit the brittle fracture behavior of dolomite rock. Mardalizad et al. (2017) and Mardalizad et al. (2019) used modified K&C to model quasi-brittle material Pietra Serena sandstone.

Under high-strain rates, fiber reinforced concrete (FRC) can exhibit different ductility, strain hardening, and energy absorption behavior compared to regular concrete. Numerical modeling is an efficient tool to investigate the structural behavior of FRC material. The numerical prediction of ultra-high performance concrete behavior under low-velocity impact loading was done by (S. Xu, Wu, and Wu (2020). For this purpose, K&C was calibrated through experimental data fitting. Triaxial compression tests were used to modify the material model. Calibrated material model was validated with drop-weight experimental tests.

Mao et al. (2014) examined the ultra-high performance concrete behavior under field blast loading with a modified version of the K&C and an accompanying experimental test for verification. The strain rate and strain-softening effects were considered during the calibration process, as the original material model is for regular concrete. The calibrated version of the K&C was found to be successful in generating the maximum deformation and damage aspects of the experimental blast test.

Thai, Nguyen, and Nguyen (2020) used modified K&C for fiber reinforced concrete and calibrated it for static and high-strain rate loadings. Material model

parameters were acquired through axial and triaxial experimental tests. The performance of the modified K&C material model was tested on compression, bending, and blast loading. The achieved results were found to be in a good agreement with the experimental data.

Overall, K&C is a capable material model for a variety of materials including FRC under static and dynamic loading conditions. However, it can be complicated for the average user. The variety of parameters provides the experienced user a way to modify the material model through trial-and-error with the data acquired by experimental tests. Opting out of complex experimental testing was aimed by the author of this thesis and the calibration process was performed through a simple test direct tension. The novel approach of parameter investigation with machine learning was applied. The following subsection includes the machine learning applications, and how they can be applied to material model calibration.

## 2.3. Machine Learning Applications

Machine learning algorithms can be used in many ways. In the manufacturing industry, machine learning applications are preferred for optimizing product quality and process (Weichert et al., 2019; Hürkamp et al., 2021). For the case of metal sheet forming, many complex deformation cases and the material characterizations for the finite element modeling process can be done with convolutional neural network algorithm (Chamekh, Bel Hadj Salah, and Hambli 2009; Hamouche and Loukaides 2018; Cekić and Çavdar 2022; S. Wu, Zhao, and Ji 2022). Misaka et al. (2020) have used experimental metal-cutting image measurements as output for deep learning schemes using convolutional neural networks.

Another sector machine learning has become popular is the automotive industry. The data-driven learning methods for crashworthiness, fuel, and battery efficiency are becoming very important (S. Wu, Zhao, and Ji 2022; Yoo, Park, and Lee 2022; Kohar et al., 2021; Liusko 2021; Kaur et al., 2021). Numerical designs using finite element methods are considered to have higher computational costs compared to deep learning applications (van de Weg et al., 2021). However, the training of learning networks can be time-consuming and expensive to begin with, and experimental validation cases are still required for accurate predictions. Overall, finite element methods are still the gold

standard for crashworthiness analysis, and data-driven methods can be used as a complementary tool.

In the structural health monitoring domain, machine learning applications can provide a faster way to process data. Deep learning systems can predict and classify data and even can locate irregularities and defects (Entezami et al., 2022; Sarmadi et al., 2022; Sarmadi and Karamodin 2020). Some caveats in structural health monitoring such as deterministic approaches of the finite element analysis, adaptive capability based on the predictions, and vulnerability to noise can be surpassed. Image recognition, time-series analysis, feature extraction, and damage identification can be used with deep learning algorithms to make it automated and improve the accuracy of structural health monitoring applications.

Karypidis (2019) aimed to build an anomaly detection system for a reinforced concrete beam. Deep learning was applied to strain data acquired from the bending of RC beams. Optic fiber systems were used to monitor the strain distribution along the steel reinforcements. Entezami et al. (2022) used unsupervised learning to develop a non-parametric approach in anomaly detection for early damage detection. The methodology was verified with two full-scale bridges, and compared with other anomaly detection techniques. Abbassi et al. (2022) intended to detect and locate the position of the damage while considering temperature variations. Intact and damaged carbon fiber reinforced polymer plates were investigated at varying temperatures. The acquired data was processed with unsupervised learning algorithms, where the performance of the autoencoder was found to be best.

Deep learning methods are a powerful tool, but they are not a magic wand. Relying solely on machine learning systems can cause problems, as the quality of the learning architecture depends on the quality of the data and the appropriateness of the learning architecture. However, combining them with finite element methods can provide accurate and computationally fast results. With regard to the numerical and experimental outcomes, the machine learning model can provide insight and give out nonlinear relationships as a grey box.

## 2.4. Estimating Material Properties with Machine Learning

The Deep Neural Network (DNN) is deep learning method more complex than artificial neural networks because it contains multiple hidden layers. More detailed explanation of DNN architectures is presented in Chapter 3.

DNN can be used in numerical and experimental investigations of concrete-like materials owing to their heterogeneity. DNN applications are widely used with concrete materials especially for compression strength estimations (Chou et al., 2014). The variations in the experimental test results for regular concrete, and FRC can be sorted using machine learning algorithms.

The compressive strength of materials such as geopolymer concrete (Gupta and Rao 2022), hybrid fiber reinforced self-compacting concrete (Kina, Turk, and Tanyildizi 2022), lightweight concrete (Nguyen 2019), fiber reinforced concrete (Zheng et al., 2022), ultra-high performance reinforced fiber concrete (Al-shawafi et al., 2023), recycled coarse concrete (Ahmad et al., 2021), and supplementary concrete (with cement replacement) (Mahajan, Bhagat, and Struct 2022) can be estimated using DNN or other deep learning applications as well other material properties.

Kina et al. (2022) aimed to develop a method for estimating the mechanical properties of fiber-induced self-compacting concrete without comprehensive experimental tests. They have used deep learning and support vector regression models to estimate the compressive, splitting tensile, and flexural strengths of 24 design mixtures. The models were trained on the data points generated by 648 experimental tests and then compared with the experimental results. Deep learning performed better in terms of accuracy than support vector regression.

To predict the flexural strength of fiber-reinforced concrete, Zheng et al. (2022) developed a method using supervised machine learning algorithms. A database of flexural strengths was obtained from the literature. The gradient boosting model performed best compared to extreme gradient boosting, and random forest learning algorithms in terms of accuracy. The machine learning algorithms provide an easy and efficient way for material property prediction, particularly on-site in the construction sector.

In addition to material model properties, behavior under dynamic loading conditions can also be examined with machine learning applications. Ibrahim et al.

(2011) developed an artificial neural network scheme to predict the blast cratering size of reinforced concrete panels. A numerical model of a reinforced concrete panel was generated using the Winfrith material model in LS-DYNA, and the numerical procedure was verified using a blast field test. A set of data was produced through numerical modeling with varying parameters of blast charge weight, standoff distance, and slab thickness. Artificial neural networks were trained on 125 numerically produced data points. The numerical and artificially produced results were compared with existing design charts and were found to be agreeable. Additionally, the blast crater size found with artificial neural networks was verified by numerical modeling on a few parameters.

Yuan et al. (2022) used artificial neural networks to predict interface bond strength with 601 data points of normal-strength and ultrahigh-performance concrete. Four interface strength factors were investigated. These are compressive strength, interface roughness, normal stress level, and casting sequence. The casting sequence was explored further and an explicit formula was generated. The generated formula was compared to other calculation methods of interface strength. It was found that the trained artificial neural network produced results in higher accuracy compared to the empirical formulation; nevertheless, the proposed equation was found to be more advantageous compared to existing models.

A maximum crack width estimation of steel material was done by Shehata et al. (2018) using artificial neural networks. To train the algorithm, 79 crack segments were recorded through a laser scanning microscope, and pixel crack data was converted to binary segments of crack width versus segment number. The performances of feed-forward and cascade forward-back propagation artificial neural networks were compared on additional data points. Feed forward back propagation algorithm was found to be performing better in terms of the calculated cost function.

Elshafey et al. (2013) aimed to estimate the crack width within serviceability limits for thick concrete members for ACI 318-08. Thick and thin reinforced concrete plates with compressive stresses varying between 33 to 70 MPa were used as data points to radial basis and feed forward back propagation neural networks. Structural element type, element, thickness, cover length, rebar size, and spacing were investigated as the parameters of the study. The radial basis neural network achieved the best accuracy, whereas existing building codes performed poorly to estimate the crack width.

Aiming to reduce the discrepancies between the impact resistance of ultra-high-performance fiber reinforced concrete, Al-shawafi et al. (2023) used artificial neural

networks and multilinear regression model to estimate the impact absorption capacity at the failure crack stage for U-shaped specimens. The researchers conducted experimental drop-weight tests and used the data to train the machine learning models. Artificial neural network outperformed the regression model in predicting energy absorption capacity with the lowest error.

## 2.5. Parameter Investigation with Machine Learning

Machine learning applications for material model parameter investigation are a useful method and have been used by many researchers. Parameter identification can be seen as a non-linear inverse problem where unknown system parameters are need to be determined (Passarello 2018). The neural network methodology can produce fast estimation compared to optimization or inverse fitting methods provided (Pitz, Rooney, and Pochiraju 2023). However, there are some challenges, such as computational requirements, a big data pool, and technical expertise to overcome problems, such as overfitting, when machine learning algorithms are used.

Schulte et al. (2022) have used artificial neural networks to investigate the material model parameter identification process for the initial guess of the parameters to capture large deformations between isotropic damage and isotropic plasticity under tensile, compression, and torsion conditions. Meißner et al. (2022) have used neural networks-based material parameter investigation with GISSMO in LS-DYNA to take failure into account. Achieved results were compared with classical material parameter investigation with LS-OPT using various FE models such as quasi-static tensile, strain-rate dependent tensile, compression, three-point bending, punch, and shear. Koch and Haufe (2019) have used supervised learning for the material characterization process to predict yield curves using a shell under direct tension.

For structural simulation of additive processed thermoplastics with the least amount of effort and accuracy, Meißner et al. (2020) used neural networks and compared them with conventional iterative optimization methods. Parameter investigation for the acrylonitrile butadiene styrene material was done with elasto-plastic material model in LS-DYNA. Data was generated with shell specimens under uniaxial tension. Damage mechanisms and strain-rate dependencies were neglected to

reduce the number of parameters. Compared to the common iterative optimization method (LS-OPT), the neural network algorithm was found to perform better.

The parameter investigation with deep neural networks provides efficiency compared to parameter fitting by trial-and-error. Current study uses a simple experimental test, uniaxial direct tension, to calibrate K&C for FRC material, and instead of other optimization method, a novel DNN scheme was constructed for parameter investigation. Following chapter presents the DNN algorithm and the process of K&C calibration.

# CHAPTER 3

# CALIBRATION OF KARAGOZIAN AND CASE MATERIAL MODEL THROUGH DEEP NEURAL NETWORK FOR FIBER REINFORCED CONCRETE

## 3.1. Introduction

In this chapter, the details of the Karagozian and Case (K&C) material model are presented. Deep neural networks were used for the calibration of K&C damage parameters, and the specifics of the investigation age are also presented. Several researchers have used similar approaches to model the behavior of concrete-like materials. However, the methodology given below proposes an easier calibration process for the FRC, while providing a certain level accuracy.

## 3.2. Neural Networks

Describing complex materials with constitutive models requires a lot of experimental calibration for the material response. Micromechanical simulations can be helpful here. However, its computational cost is high especially when nonlinear finite element solutions are used with fracture or damage conditions (Masi et al., 2021; Kurumatani et al., 2016; Goyal, Johnson, and Dávila 2004).

Machine Learning is a promising approach where a computer program improves its performance P, on a task T, if it's able to produce more accurate results for the same task with experience E, according to Mitchell (1997). The machine learning system learns from the training data set and its predicted error is measured then minimized.

There are three main categories in machine learning systems. These are supervised/unsupervised learning, batch/online learning, and instance-based/model-based learning depending on the supervision amount, the capability to learn adaptively in real-time, and comparing and detecting new data points through pattern detection, respectively (Géron 2017). The nature of the problem, data and time-availability effects

which categories are to be used. Industries such as automotive, transportation, finance, and healthcare are significantly affected by advances in machine learning and data science (Grigorescu et al., 2019; Ali et al., 2021; Gu, Kelly, and Xiu 2018; Vellido 2020).

An Artificial Neural Network, inspired by the biological neurons in our brains, can manage large and complex data for various problems. The ANNs are versatile and scalable, thus they are at the hearth of Deep Learning. Image recognition, natural language processing, autonomous vehicles, and personalized product recommendations are some of the fields in which ANN are used. With the increase in computational power and advancements in solution algorithms, the training of large networks takes less time. Additionally, when compared to other machine learning techniques, ANN performs exceptionally when big data is concerned (Géron 2017).

The presence of multiple hidden layers in an ANN is called a Deep Neural Network (DNN). A DNN is a simplified version of a human cerebral cortex. The artificial neurons are stacked to form a DNN, which was deemed impossible in the late 1990s (Géron 2017).

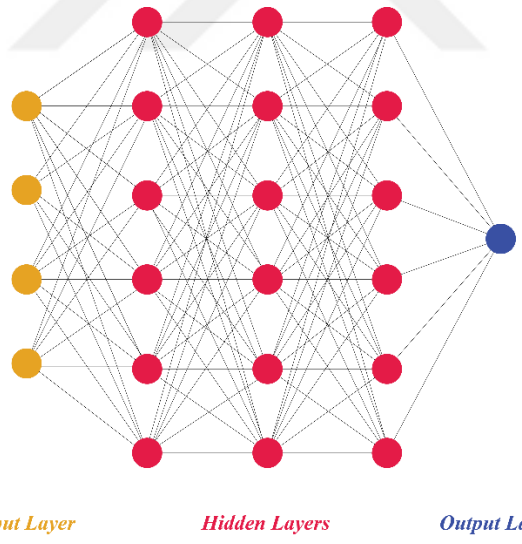


Figure 3.1. A Dense Neural Network scheme with four input parameters, three hidden layers and an output layer

The data set in DNN training is mostly handled in batches and each pass here is called an epoch or iteration. During the forward pass, each batch is passed through from input layer to the first hidden layer and an output is calculated. Then this output is passed to the other hidden layers. This progress is continued until the batch has been

through the last layer which is the output layer. At the end of this forward pass, an error is calculated between the actual output and the output of the first pass, using a loss function. Henceforth, a backpropagation algorithm with chain rule is applied to determine the contribution of each layer to the calculated error. An error gradient is calculated for each neuron connection in each layer. The weights of the connections have random initial values during the first forward pass, and are then reappointed with backpropagation according to the calculated error gradient. The initial weights and biases are appointed randomly to introduce asymmetry and avoid non-zero neurons. Introducing zero or identical weights terms causes backpropagation to appoint the same values throughout progress, even for a complex neural network scheme with hundreds of layers. A general Deep Neural Network scheme with four input parameters, three hidden layers and an output layer with single parameter is given in Figure 3.1.

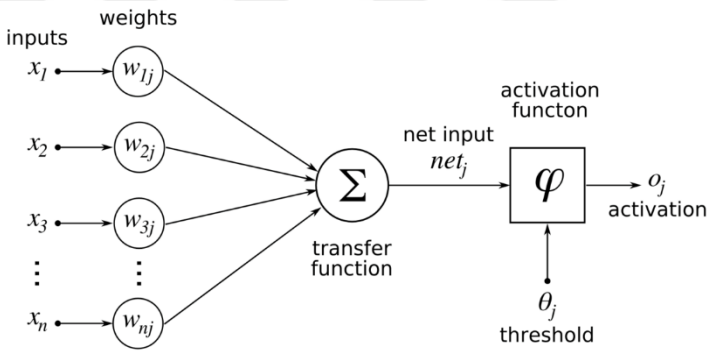


Figure 3.2. Schematic view of a Neural Network

The neuron in a DNN evaluates multiple input signals to decide whether to activate based on the weighting of those signals via an activation function. How well the algorithm is doing is evaluated by a cost function, calculated between the predicted and the actual output data. An optimization algorithm is used to minimize the cost function. The minimized cost function corresponds to a global optimum and the algorithm's convergence to a global optimum is done by calculating the gradients of the cost function with respect to the weights. The nonlinearity of a DNN with feed-forward architecture comes from the backpropagation and the activation function. Schematic view of a Neural Network is given in Figure 3.2.

The optimizer in the neural networks helps to find the appropriate weights that minimize the cost function. The speed of the used optimizer is a problem when dealing with large data sets. The most used optimizer is gradient descent however its

convergence speed is an issue for large models. Momentum-based optimizers can be handy here such as stochastic gradient descent (SGD), Adam (Adaptive Moment Estimation) (Kingma and Ba 2015) and Nadam (Nesterov-accelerated Adaptive Moment Estimation) (Dozat 2016). Additionally, a learning rate is prescribed to the optimizer function to decide on the size of the step when reaching the global optimum. The prescribed learning rate can be a linear, exponential, or step based (changing after certain epochs/iterations) function.

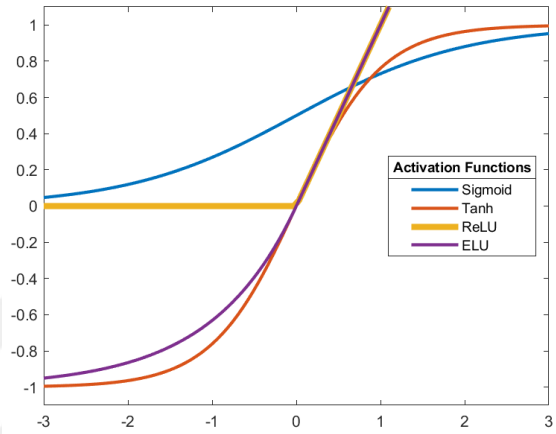


Figure 3.3. Sigmoid, tanh, ReLu and ELU activation functions

Popular activation functions given in Figure 3.3 are exponential linear (ELU), rectified linear (ReLU), logistic (Sigmoid) and hyperbolic tangent activation functions. The ReLU is a continuous function, but it is non-differential at z=0, and its derivative at z<0 is 0. These characteristics can cause some difficulties with certain optimizers such as vanishing or exploding gradients (Ribeiro et al., 2019). However, it is a fast activation function so its commonly chosen in many neural network architectures. Another advantage of ReLU is that does not have a maximum value which allows it to work effectively with Gradient Descend optimization. The sigmoid function is continuous and differentiable. The s-shaped function gives values between 0 and 1. Additionally, the derivatives of the sigmoid function are non-zero for all input values. The hyperbolic tangent function is s-shaped like the sigmoid functions, differentiable and continuous. Its output is between -1 and 1, which makes the output of each layer more centered around 0 making it a fast optimizer. The ELU activation function is a variation of the ReLU activation function. The key differences are that the ELU has

negative values when z<0 and it has nonzero gradients at z<0. Additionally, the shape of the ELU function is smooth which helps with the optimizer's speed.

The complexity of the NN depends on the problem at hand. There are a number of different options when constituting a DNN with different hyperparameters including how many hidden layers, neurons and dropouts to employ, and which activation, and cost function, optimizer and learning rate to use. Above mentioned are hyperparameters and a grid search or randomized search option could be employed to see which works best for the used data set. TensorFlow framework can be used here which is an open-source platform that includes the common training models (Abadi et al., 2016).

Before the input data set is put through the DNN algorithm, it is organized. Normalization is applied to the input parameters by removing the mean value and scaling the unit variance. This makes sure the convergence points in the correct direction, toward the global optimum, and so that it does not take too much time during the optimization. Ready-to-use Python library Scikit-learn can be used for this purpose. The normalization is done to each feature separately. Predictions of the fitted DNN model require a scale-back function thus each parameter is returned to its sort. After normalization, the data set is split into training, validation and test sets. Splitting progress can be done using the Scikit-learn library as well.

Machine learning organizations for parameter investigation are a useful method and have been used by many researchers. Schulte et al. (2022) have used artificial neural networks to investigate the material model parameter identification process for the initial guess of the parameters to capture large deformations between isotropic damage and isotropic plasticity under tensile, compression and torsion conditions. Meißner et al. (2022) have used neural networks-based material parameter investigation with GISSMO in LS-DYNA to take failure into account, then compared the results with classical material parameter investigation with LS-OPT using various FE models such as quasi-static tensile, strain-rate dependent tensile, compression, three-point bending, punch, and shear. Misaka et al. (2020) have used experimental metal cutting image measurements as output for deep learning schemes using convolutional neural networks. Koch and Haufe (2019) have used supervised learning for the material characterization process to predict yield curves using a shell under direct tension.

Compared with classical optimization-based iterative parameter investigation, machine learning applications can provide a faster and more automated approach. However, there are some challenges, such as computational requirements, a big data

pool, and technical expertise to overcome problems, such as overfitting, when machine learning algorithms are used. The DNN scheme can be used in numerical and experimental investigations of concrete-like materials for categorizing purposes. The variations in the experimental test results for regular concrete, and FRC can be sorted using machine learning algorithms.

The current study uses Deep Neural Networks to calibrate a material model in LS-DYNA to utilize it when modeling FRC with varying steel fiber and polyvinyl alcohol synthetic fiber additions. Subsequently, the strain-softening behavior of FRC materials under tension-dominated conditions was used for calibration and validation. Direct tension and four-point bending tests were chosen as the tension-dominated conditions.

The main aim in this study is to use a simple test, such as direct tension, during material model calibration and use the calibrated material model for complex loading conditions. Thus, other extensive experimental tests were made redundant, other than the simple compressive and tension strength tests. The tensile strength is more critical because its lower than its compressive strength, thus compression-dominated behavior was not investigated. As a future study, FRC material's behavior with primary stresses in compression can be studied through material model parameter investigation using DNN.

The K&C material model in LS-DYNA was selected to represent the ductile nature of FRC. The damage function of ($\lambda$ & $\eta$) and the tensile damage parameter (b2) were selected to be investigated with the DNN scheme. Single elements under uniaxial tension were generated to form the input database. Single element numerical testing is a cost-effective way to demonstrate the behavior of given material model parameters.

The output feature of the DNN was selected as a single parameter. This single parameter is a ratio that represents the ductility behavior of FRC material during direct tension testing. It was selected as the ratio of the numerical to experimental displacement values corresponding to 70 % of maximum tensile strength from single element numerical analysis and direct tension experimental test results (Figure 3.6, from Çetin, 2020). Thus, the DNN learns the relationship between the numerical input and how well the numerical input is doing compared to experimental behavior. An important factor here was to use a database generated by the numerical analysis and an experimental characteristic as output. The numerical input and experimental output parameter investigation method is a novel approach to the author's knowledge. The

nonlinear relationship formed by the DNN scheme provides an important insight into the context of FRC modeling.

## 3.3. Karagozian and Case Material Model

Karagozian and Case (K&C) is a material model initially used for concrete impact, blast, and large deformation modeling (Malvar et al., 1997). Originally modified from the material model MAT_16, the currently used version of K&C material model is the third version, labeled as K&C (Release 3). The new release of K&C incorporates an automatic parameter generator that relies on the uniaxial compression strength of concrete given by the user. Thus, the complete set of 49 parameters of the K&C material model can be acquired. Current study calibrates 27 parameters of K&C with DNN that are presented in Table 3.1 to represent FRC behavior. Other parameters and their brief definitions are provided in Table 3.2.

Table 3.1. K&C parameters that were calibrated with DNN for FRC behavior

| **Parameter** | **Description** |
|---|---|
| $b_2$ | Tensile damage parameter |
| $\lambda 1$ through $\lambda 13$ | Damage function,<br>1 through 13 |
| $\eta 1$ through $\eta 13$ | Internal damage parameter,<br>1 through 13 |

Table 3.2. Other K&C parameters and brief definitions

| Parameter | Description |
|---|---|
| ρ | Mass density |
| ν | Poisson's ratio |
| $f_t$ | Uniaxial tensile strength |
| $a_0$ | Maximum failure surface parameter, or compressive strength for parameter generator ($-f_c$) |
| $a_1$ | Maximum failure surface parameter |
| $a_2$ | Maximum failure surface parameter |
| $a_{1f}$ | Residual failure surface parameter |
| $a_{2f}$ | Residual failure surface parameter |
| $a_{0y}$ | Yield surface parameter |
| $a_{1y}$ | Yield surface parameter |
| $a_{2y}$ | Yield surface parameter |
| w (omega) | Associativity Parameter |
| $b_1$ | Compressive damage parameter |
| $b_3$ | Triaxial tension damage parameter |
| sλ | Stretch factor |
| $\delta$ | Scaled damage measure |
| edrop | Post peak dilatancy decay |
| rsize | Unit conversion factor for length |
| ucf | Unit conversion factor for stress |
| lcrate | Curve for strain-rate effects |
| Lw (locwidth) | Three times the maximum aggregate diameter |
| npts | Number of points in $\lambda$ versus $\eta$ damage relation |

K&C was explicitly developed for concrete material. However, some researchers selected to modify it to fit concrete-like material. Kucewicz et al. (2020) modified K&C to model brittle material dolomite rock while Mardalizad et al. (2019) used modified K&C to model quasi-brittle material Pietra Serena sandstone. L. Y. Xu et al. (2019) used default parameters and their modified versions of K&C for modeling penetration and perforation of reinforced concrete under impact. S. Xu et al. (2020) used modified K&C for ultra-high-performance concrete under low-velocity impact loading. Thai et al. (2020) used modified K&C for fiber reinforced concrete and calibrated with static and high strain rate loadings.

There are three failure surfaces in K&C. These are yield, maximum and residual surfaces. As pressure increases, the yield surface is the first one reached. After that, the existing surface is found by interpolating the yield and maximum surfaces. The location of the existing surface depends on the λ; modified effective plastic strain, or internal damage parameter. As λ increases and becomes equal to $\lambda_m$, maximum or critical

effective plastic strain (calibrated from experimental data of (Y. Wu, Crawford, and Magallanes 2012)), the maximum surface is reached. λ continues to increase, and the current surface is interpolated between maximum and residual surfaces.

The general formulation of these surfaces can be defined as such:

$$F_i(p) = a_{0i} + \frac{p}{a_{1i} + a_{2i}\, x\, p} \tag{1}$$

Where

p is the pressure

$a_{ij}$ ( j = 0, 1, 2) are the parameters of failure surfaces generated from experimental tests

$F_i$ (p) is the surface definition

Interpolations between maximum-yield and maximum-residual surfaces can be expressed as the following equation:

$$F(I_1, J_2, J_3) = \begin{cases} r(J_3)\left[\eta(\lambda)\left(F_m(p) - F_y(p)\right) + F_y(p)\right], & \lambda \leq \lambda_m \\ r(J_3)\left[\eta(\lambda)\left(F_m(p) - F_r(p)\right) + F_r(p)\right], & \lambda > \lambda_m \end{cases} \tag{2}$$

Where

η is a user-defined damage function, a function of λ

F ( $I_1$ , $I_2$ , $I_3$) is the failure surface

r( $J_3$ ) is the scale factor in the form of the William-Warnke equation

λ is an ever-increasing parameter. However, η the damage function, is limited between the values of 0 and 1. λ and η both begin at the value of 0. As λ increases and becomes equal to $\lambda_m$, η is equal to 1. After this point, λ continues to increase. However, η begins to decrease until the value of 0. The default λ & η graph is presented in Figure 3.4.

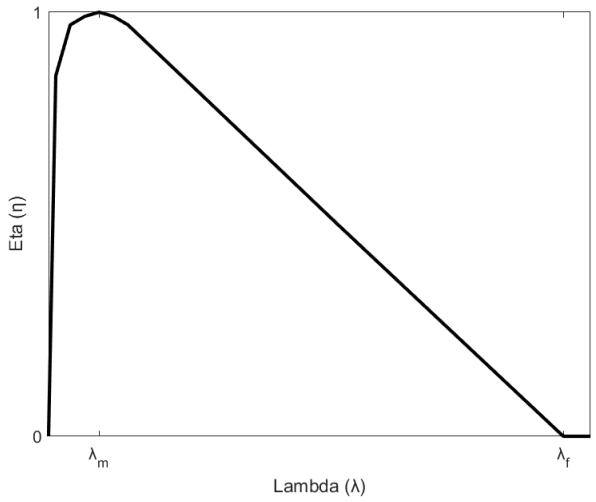


Figure 3.4. Default material model damage function distribution

The material card of K&C requires 26 values for λ & η. Calculation of λ is given at the following function;

$$\lambda = \begin{cases} \int_0^{\overline{\varepsilon^p}} \dfrac{d\overline{\varepsilon^p}}{\mathrm{r}_f\left(1+\dfrac{p}{\mathrm{r}_f \mathrm{f}_t}\right)^{b_1}}, & p \le 0 \\ \int_0^{\overline{\varepsilon^p}} \dfrac{d\overline{\varepsilon^p}}{\mathrm{r}_f\left(1+\dfrac{p}{\mathrm{r}_f \mathrm{f}_t}\right)^{b_2}}, & p < 0 \end{cases} \tag{3}$$

Where

$\mathrm{r}_f$ is the strain rate enhancement factor

$\mathrm{f}_t$ is the concrete tensile strength

$d\overline{\varepsilon^p}$ is the increment of the effective plastic strain

$b_1$ & $b_2$ are the compressive and tensile damage parameters

Damage monitoring is also possible for K&C by the quantity “scaled damage measure, δ” as labeled in LS-DYNA Manual II (LSTC 2007), with the formulation given below;

$$\delta = \frac{2\lambda}{\lambda + \lambda_m} \tag{4}$$

Scaled damage measure can be observed from Effective Plastic Strain (EPS) fringe plots within a range of 0 to 2. The transition from 0 to 1 happens when the existing surface is between yield and maximum surfaces. When the maximum surface is

reached and surpassed, it is between 1 and 2, between the maximum and residual surfaces.

Additionally, K&C includes an Automatic Parameter Generator (APG). Generated parameters are based on experimental uniaxial compression and tension tests and triaxial compression tests of a concrete sample with 47 MPa compressive strength (Malvar et al., 1997). These experimental tests were done under different levels of confinement and hydrostatic pressure. Only density, uniaxial compression strength, and SI to Imperial unit conversion factors for stress and length must be entered for the APG to be used. The APG calculates the values for the given compression strength in proportion with the tested calculated strength of 47 MPa. A default set of $\lambda$ & $\eta$ can be used from the APG. Compressive, tensile, and triaxial tension damage parameters (b1, b2, and b3, respectively) can be determined from the APG as well.

K&C controls shear dilatancy behavior with "w", associativity parameter. w = 0 gives a non-associative behavior, yet a fully associative model is achieved with w = 1. K&C developers (Y. Wu and E.Crawford 2015) recommend values between 0.5 and 0.9 for w to capture concrete's expansion through shear dilatation. For well-confined and ultra-high to high strength concretes with fine aggregates, w parameter values between 0.8 and 0.9 can be used.

K&C requires an equation of state (EOS) card to be added to handle pressure and volumetric strain properties. The APG produces the EOS parameters according to the given compressive strength, density, and unit conversion factors.

K&C promotes to be a non-mesh-dependent material model between the mesh sizes of 4 and 25 mm. This is done by relating the fracture energy and localization width. However, the non-mesh-dependency is only provided with the analyses where the automatically generated parameters are used.

Between material parameters of K&C, fracture zone length is chosen together with material parameter b2, damage parameter in tension. Parameter b1 controls the softening in compression, while b2 and b3 govern the softening in tension. Lw parameter is identified as three times the maximum aggregate size in LS-DYNA Manual II (LSTC 2007). However, according to Malvar et al. (1997), if localization occurs in one element, element size is equal to localization width (or crack width, where it is 1-6 times the aggregate size). According to Kong et al. (2017), for the correct presentation of concrete surface crabbing and cratering, element size needs to be smaller

than fracture length. Tu and Lu (2009) and Kong et al. (2016) have used Lw as the element size.

## 3.4. Tensile Damage Parameter and Damage Distribution Calibration

The damage distribution and directly the λ & η calibration is a process done by several researchers to represent concrete-like materials like rock, ultra-high-performance concrete, fiber-reinforced concrete, and strong concrete. Table 3.3 summarizes the coefficients used for the damage distribution. The works of the researchers in Table 3.3 are briefly mentioned.

Table 3.3. Literature investigation of the coefficients of the damage distribution (λ and η) in K&C Material Model

| | **(Kong et al., 2017)** | **(Thai, Nguyen, and Nguyen 2020)** | **(S. Xu, Wu, and Wu 2020)** | **(Markovich, Kochavi, and Ben-Dor 2011)** |
|---|---|---|---|---|
| **a** | 3 | 3 | $\eta = ae^{b\lambda}$ | exponentially decreasing (No equation) |
| **c** | 0.29 | 0.29 | | |
| **d** | 1.86 | 1.86 | | |
| $\lambda_m$ | 8.70E-05 | 6.00E-04 | 8.41E-05 | 9.00E-05 |

Kong et al. (2017) modified the K&C material model to improve its ability to predict concrete's capability to show tensile failure such as scabbing and cratering after dynamic loading. Certain K&C characteristics were aimed to be altered; the sensitivity of the high-pressure behavior was not fully reflected in the limit loading conditions. The material model did not provide an erosion criterion and an external card is needed to be provided. The increase in tensile fracture strain observed in experimental findings (Schuler, Mayrhofer, and Thoma 2006; Weerheijm and Van Doormaal 2007) under high-strain-rate loading was not reflected in the K&C numerical results in terms of fracture strain and fracture energy. In light of these shortcomings, modifications were made by Kong et al. (2017) to the damage distribution of K&C model and as well as to the strength surfaces, dynamic increase coefficients, and tensile damage accumulations. The damage distribution which was given as a 13-pair data point (λ & η), was redefined as the equation (5).

$$\eta(\lambda) = \begin{cases} \frac{a\,\lambda}{\lambda_m} + (3-2a)\left(\frac{\lambda}{\lambda_m}\right)^2 + (a-2)\left(\frac{\lambda}{\lambda_m}\right)^3, \ \lambda \leq \lambda_m \text{ , strain hardening} \\ \frac{\frac{\lambda}{\lambda_m}}{c\left(\frac{\lambda}{\lambda_m}-1\right)^d + \frac{\lambda}{\lambda_m}}, \ \lambda < \lambda_m \text{ , strain softening} \end{cases} \quad (5)$$

The coefficients in the proposed damage distribution function by Kong et al. (2017) are achieved based on trial-and-error. The given coefficients in the Table 3.3 are obtained by matching numerical and experimental uniaxial stress-strain curves. Analytical formulations developed by Attard and Setunge (1996) were used to find the coefficients of the damage distribution. Single element numerical models were used to show the capability of the modified damage distribution.

Additionally, Kong et al. (2017) compared the uniaxial stress-strain curves found from the original and modified K&C material model results. The results indicated that the original K&C damage distributions reflected a stiffer loading phase and has a larger softening phase compared to modified K&C and the experimental results. Also, the stress capacity was found to be higher in the original K&C material model.

Same Kong et al. (2017) study used the modified K&C material model and used it for projectile impact to show the cratering and scabbing capabilities. Even though the primary objective is to catch the experimental damage distribution under perforation, displacement, acceleration and velocity profiles were found to be a good match with the modification made to K&C material model.

Thai et al. (2020) used the K&C damage distribution of Kong et al. (2017) to simulate a calibration model for FRC under static and dynamic loading conditions. The performance of the modified K&C material model parameters was investigated with static bending and single element compression numerical results, as well as dynamic blast loading.

Thai et al. (2020)'s need to modify the K&C material model has risen from its inability to reflect different concrete-like materials without alterations. Calibration was done in accordance with axial and tri-axial experimental tests under tension, compression and high-strain-rate loading conditions. Failure surface, the dynamic enhancement factors, damage function, and evolution, and equation of state parameters were calibrated.

Thai et al. (2020) used Kong et al. (2017)'s damage distribution function and changed the coefficients of strain hardening and softening curves by trial-and-error. The damage distribution of (Kong et al., 2017) provides convenience even for FRC.

Researchers of S. Xu et al. (2020) have modified K&C material model to reflect the Ultra-High Performance Concrete behavior under low-velocity impact loading. Experimental tri-axial compression tests were carried out to use for the modification process.

S. Xu et al. (2020) used single element numerical tests to show the default damage distribution curve ($\lambda$ & $\eta$) has a very steep softening phase under compression and tension. These characteristics were found to be unlike UHPC behavior, and a gradually decreasing exponential curve was prescribed to the strain-softening phase of the damage distribution. The curve's equation is given in Table 3.3. The coefficients of the exponentially decreasing curve were generated by trial-and-error through experimental data fitting. Additionally, strength surface, equation of state and strain-rate parameters of K&C were derived during this process as well.

In addition, S. Xu et al. (2020) generated validation cases with single elements under tri-axial compression tests to reflect the modified parameters' performance. Also, the performance of the modified K&C parameters with UHPC was investigated with drop weight tests. The deflection profile and damage patterns of beam and column UHPC members were shown to be in good agreement with the experimental findings. However, the period of the UHPC column member under forced vibration has been found to be underestimated.

Markovich et al. (2011) have modified K&C material model's damage distribution to reflect strong concrete with compression strengths between 50 and 100 MPa. Calibration of the damage parameters was done by matching the experimental tri-axial compression test results of Attard and Setunge (1996) with their numerical counterparts. Strength surface coefficients, damage scaling parameter for compression (b1), and equation-of state parameters of K&C were calibrated as mentioned.

Researchers continue their investigation process (Levi-Hevroni et al., 2018) with an additional study on the dynamic tensile properties with K&C parameter calibrations. Split-Hopkinson bar test results were used for the numerical modeling and parameter adjustments. Levi-Hevroni et al. (2018) revealed that the damage distribution parameters required additional recalibration when the compressive loading conditions were changed to dynamic tensile loading.

In the current study, the damage distribution proposed by Kong et al. (2017) given with the equation (5) was selected as an appropriate representation for FRC. The c, d, and $\lambda_m$ strain softening parameters in the Kong et al. (2017) damage distribution proposition were selected to be part of the K&C material model parameter investigation study in the DNN algorithm. “a” strain hardening parameter in the proposed function was kept constant as proposed by Kong et al. (2017) as the value of 3 as seen in Table 3.3. Figure 3.5 represents the damage distribution proposed by Kong et al. (2017). with the a, c, d, and $\lambda_m$ parameters proposed by Kong et al. (2017).

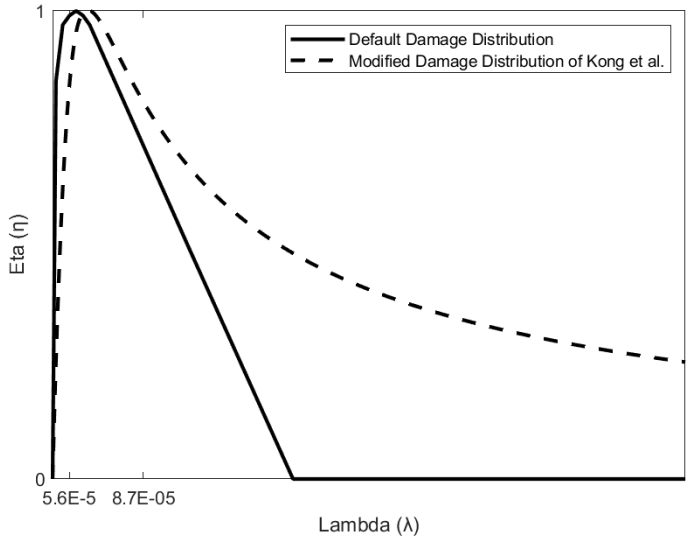


Figure 3.5. Default and Kong et al. damage distribution functions (Kong et al., 2017)

K&C damage distribution can be defined by a 13-pair curve represented by λ & η values. Damage distribution equations of c, d, $\lambda_m$ parameters were selected to be part of this study. Schulte et al. (2022) have used artificial neural networks for scanning through initial parameter determination and to select an interval range for each parameter search. Such examination was omitted for the current study. The parameter ranges for $\lambda_m$ were selected from the literature, and c and d parameters were selected according to the shape of the material model damage distribution.

Even though the material model parameter search is easy with the proposed DNN method, the algorithm can derive many local maxima that are irrelevant to the desired behavior. The researcher applying this methodology must select reasonable and efficient ranges for the input parameters. This comes from getting familiar with the selected material model and its possible capabilities. Thus, the b2, c, d and $\lambda_m$ parameters were selected keeping the mentioned in mind.

The ranges of $\lambda_m$ parameter are limited between 5E-5 and 5E-4. The first $\lambda_m$ value is the default value. Increasing $\lambda_m$ too many yields unrealistic behavior results for the FRC material investigated here. The latter $\lambda_m$ was selected according to literature research (Table 3.3).

K&C material model also includes a tensile damage parameter of b2, with a default value of 1.35, and its effect on the damage distribution is highly important. For that reason, b2 parameter was selected as an input parameter of the DNN algorithm for the data-driven model.

## 3.5. Application of Deep Neural Network

DNN input data was selected as K&C parameters that highly affect the damage distribution and energy absorption capacity. The output of DNN was selected as an experimentally derived output instead of a numerical output. The purpose of this is to generate a material model parameter set that fits the required experimental behavior, and not to use DNN instead of numerical analysis. By including an experimentally derived (Figure 3.6) output, accuracy and complexity of the K&C material model parameter investigation method were increased. Additionally, using a single parameter as the output feature increases the DNN algorithm's speed. DNN input parameters to reflect FRC behavior were selected as b2, c, d and $\lambda_m$. The material properties of the investigated FRC mixtures were given in Table 3.4.

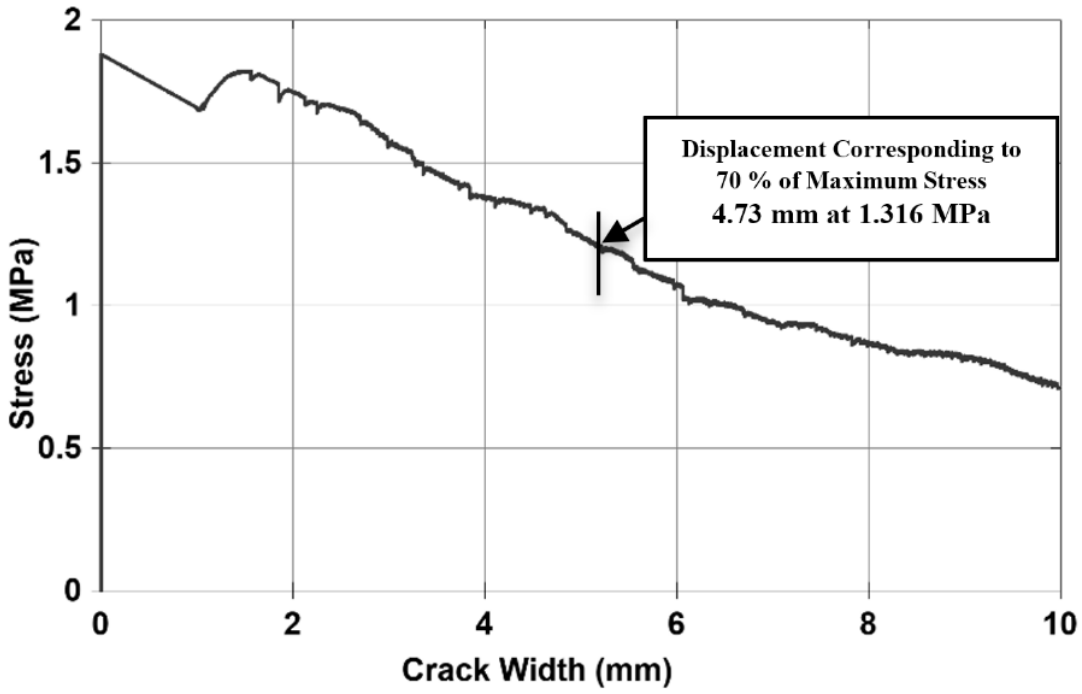


a)

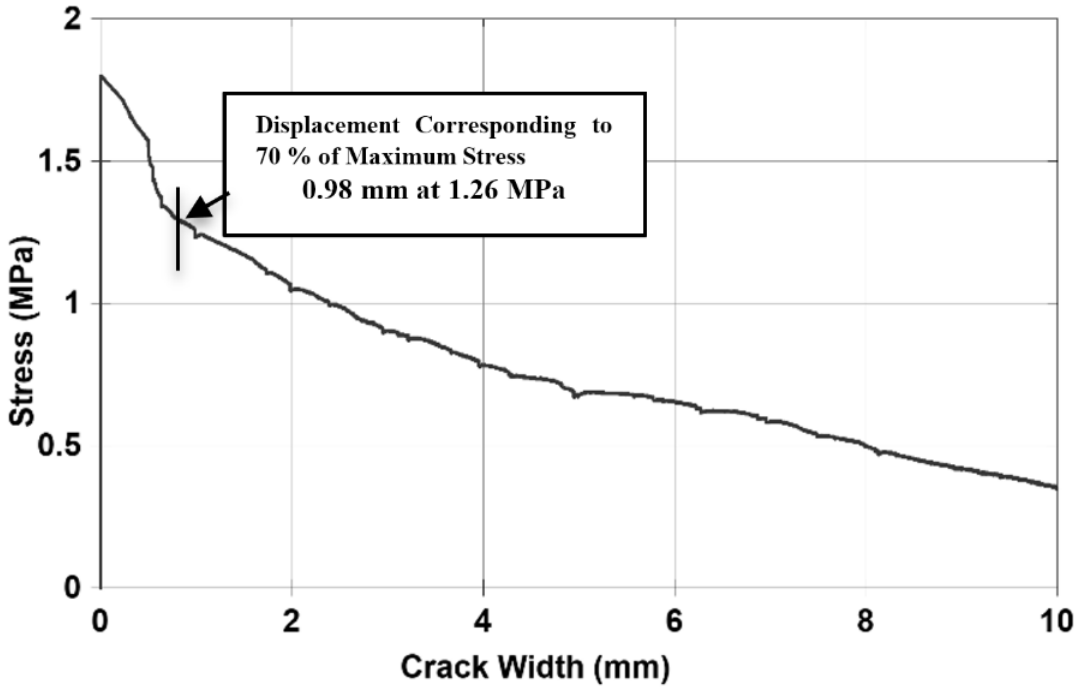


b)

Figure 3.6. Experimental direct tension result of the a) DT-M2 and b) DT-M1+PVA material (Çetin, 2020)

Table 3.4. Mixture properties of FRC mixtures of Çetin (2020)

| Specimen Name | Steel Fiber Ratio (%) | Steel Fiber Type | PVA Ratio (%) | Compressive Strength (MPa) |
|---|---|---|---|---|
| DT-M2 | 0.75 | 65/60 3D | - | 30.98 |
| DT-M1+PVA | 0.75 | 35/45 3D | 0.25 | 30.02 |

Data for the DNN was generated with single element numerical model under direct tension loading. Repeated analyses were done on a single cube element with a length of 10 mm and symmetrical boundary conditions as given in Figure 3.7. Data generation was proceeded following the steps displayed in Figure 3.8. K&C material model requires the entry of an λ & η curve with 13 pairs. The required curve was generated with the Numpy library of Python, using the selected c, d, $\lambda_m$ parameters. Thus, even though only 3 inputs were selected for the damage distribution, a total of 26 parameters were altered in each analysis file. Tensile damage parameter b2 was also changed in each analysis file. As a result, a total of 27 material model parameters were replaced with each analysis file for each FRC mixture.

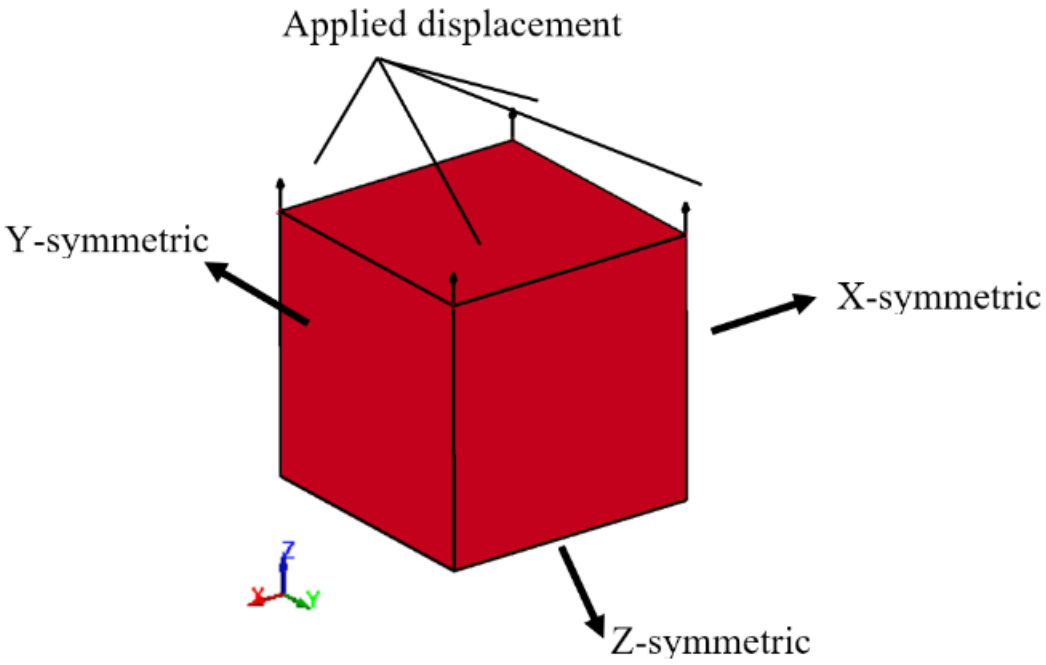


Figure 3.7. Single element numerical model under direct tension

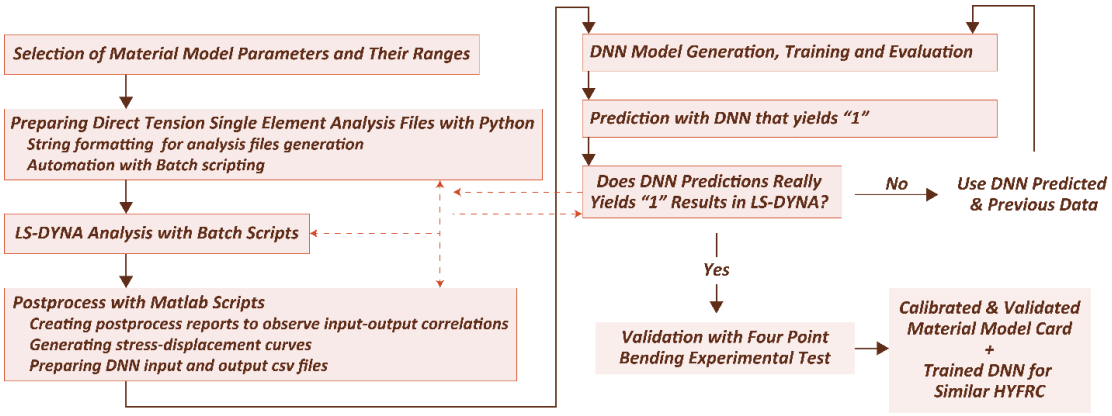


Figure 3.8. Workflow on the DNN

String formatting was done with the Python OS module to generate numerical analysis files in specific folders. Additionally, a batch file was prepared with Python scripting to enter the folder in the directory and initialize LS-DYNA analysis, then return to the main directory, following this sequence for the whole range of parameters.

The postprocess of the study required generating a stress-displacement curve for each analysis. A MATLAB script was written for this purpose that automatically goes into each folder in the working directory and saves the resulting stress-displacement into a comma-separated values (csv) file in each folder for visual observation. Thus, MATLAB figures were used to observe a general orientation and select the input parameters accordingly as mentioned in Chapter 3.3.

To generate the outputs for the DNN algorithm, MATLAB scripts were used. The displacement corresponding to 70 % of the maximum stress was recorded from each folder and divided into the experimentally acquired displacement corresponding to 70 % of the maximum stress. The purpose here was to prepare enough data for the DNN algorithm that gives the 1 as a numerical to experimental displacement ratio at 70 % of the maximum force for accurate prediction.

DNN algorithm was generated with approximately 1500 data points (examples) in each FRC mixture. Even though there were 3 times more data points that were initiated, the numerical to experimental displacement ratios were far from the desired range of 1. The DNN data fitting was only done between the numerical to experimental displacement ratio outputs of 0.5 and 1.5.

DNN algorithm was generated with Python Tensorflow library. The data to be progressed through DNN scheme was normalized within each parameter range and shuffled. The organized data were randomly divided into training, validation, and test

sets. Data organization, normalization, and splitting procedures were done with Python Scikit-learn library. DNN hyperparameters of hidden layers, neuron numbers, dropout percentages, selected activation, and cost functions, optimizer and learning rate functions were prescribed with Tensorflow library. The hyperparameters were selected through a grid search for both mixtures. Detailed descriptions of hyperparameters are given in the Chapter 3.1.

Fitting of the DNN algorithm was checked to see if overfit or underfit has occurred. Overfit occurs when algorithm cannot generalize the predictions for overall data and can only give true predictions for the data on the training set. Underfit is when the algorithm has not learned enough to make predictions with small enough errors.

Generalized and accurate prediction through DNN scheme can come from neither overfit or underfit. The errors of the validation and training should get closer with each iteration (epochs) and the training and validation data set errors should be close to each other at the end. As seen from Figure 3.9, the training and validation set errors are at small loss values for the hyperparameters given in Table 3.5. Thus, the current DNN algorithms can give accurate predictions on a varying data set.

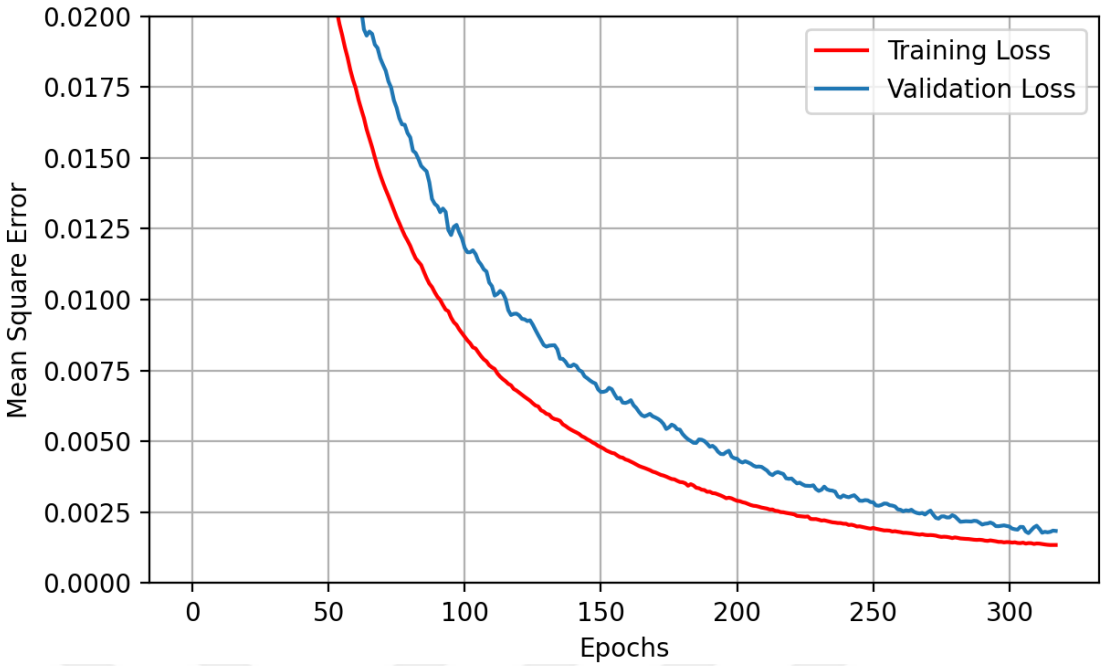


a)

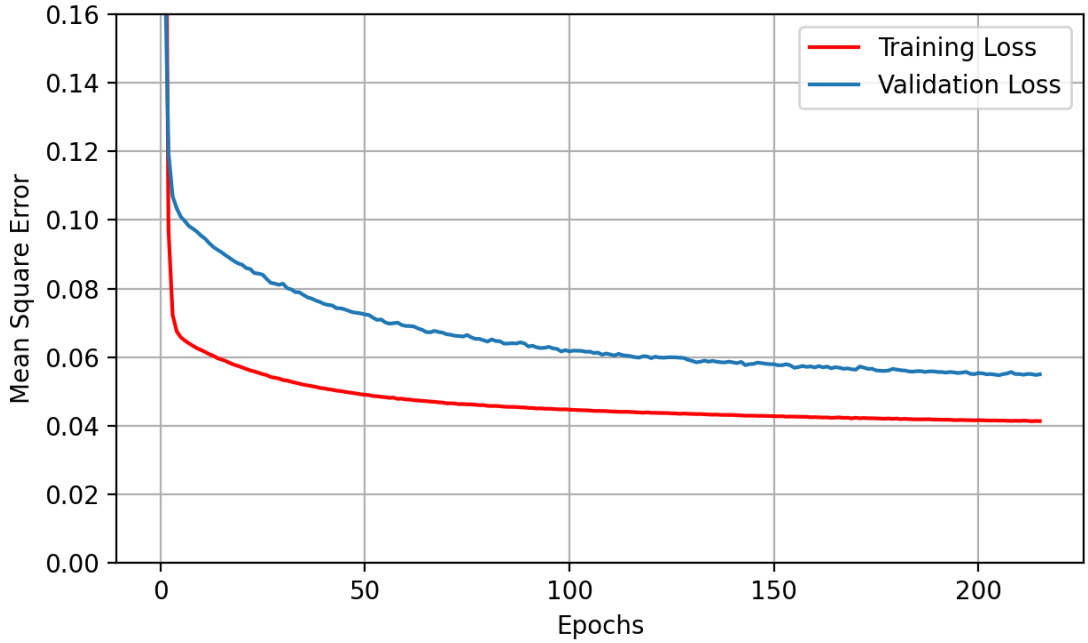


b)

Figure 3.9. DNN cost function progress with respect to epochs (iterations) for a) DT-M2 and b) DT-M1+PVA mixture

The DNN prediction accuracy was checked with numerical analysis as well. After a low-cost generating DNN was constituted, the model was predicted with a range of b2, c, d, $\lambda_m$ parameters and outputs yielding numerical to experimental displacement ratio of 1 were recorded. The recorded output ranges of b2, c, d, $\lambda_m$ were used for LS-

DYNA single element analysis file generation to make sure the DNN produced correct predictions. The input parameter ranges were kept approximately the same during the DNN learning and prediction phases.

Table 3.5. Properties of the current DNN Hyperparameters

| **Hyperparameters** | **Used Setting For DT-M2** | **Used Setting For DT-M1+PVA** |
|---|---|---|
| Neurons | 128 | 64 |
| Activation Function | Elu | Elu |
| Hidden Layers | 7 | 7 |
| Early Stopping Patience | 10 | 10 |
| Maximum Epochs | 5000 | 10000 |
| Cost Function | Mean Square Error | Mean Square Error |
| Optimizer | Adam | Stochastic Gradient Descent |
| Learning Rate | Step Decay: 0.1359E-4 * 0.99 ** (step / 10) | Step Decay: 0.001359 * 0.99 ** (step / 10) |

The disclosed procedure of generating analysis files, doing the single element analysis and getting outputs, putting all the data into DNN to fit the model, and then generating outcomes yielding the numerical to experimental displacement ratio of 1 was repeated until the DNN generated numerical to experimental displacement ratio of 1 output were actually gives the ratio of 1 from the numerical analysis.

Table 3.6. DNN predicted parameters that yield the numerical to experimental displacement ratio of 1 for DT-M2 and DT-M1+PVA mixture

| **Specimen Name** | **b2** | **c** | **d** | **$\lambda_m$** |
|---|---|---|---|---|
| DT-M2 | -11.98 | 0.666 | 2.3 | 4.099E-4 |
| DT-M1+PVA | -9.211 | 1.184 | 2.5 | 5.6E-5 |

The data points were increased with each disclosed procedure because DNN-generated outcomes were used for numerical analysis. After their outcomes were recorded, they were put into the DNN algorithm as input examples. As mentioned previously, approximately 1500 examples were used for the DNN fitting. The hyperparameters for the numerical to experimental displacement ratio of 1 yielding DNN are in Table 3.3. The single element numerical analysis result is in Figure 3.9 while the DNN-predicted material model parameters are in Table 3.4.

Table 3.7. Lambda-Eta parameters found from DNN for DT-M2 mixture

| **DT-M2** | **Lambda** | **Eta** |
|---|---|---|
| 1 | 0.00E+00 | 0 |
| 2 | 1.03E-04 | 0.5781 |
| 3 | 2.05E-04 | 0.875 |
| 4 | 3.07E-04 | 0.9844 |
| 5 | 4.10E-04 | 1 |
| 6 | 1.33E-03 | 0.4323 |
| 7 | 2.25E-03 | 0.2073 |
| 8 | 3.16E-03 | 0.1266 |
| 9 | 4.08E-03 | 0.088 |
| 10 | 5.00E-03 | 0.0661 |
| 11 | 1.00E+00 | 0 |
| 12 | 1.00E+01 | 0 |
| 13 | 1.00E+06 | 0 |

Table 3.8. Lambda-Eta parameters found from DNN for DT-M1+PVA mixture

| DT-M1+PVA | Lambda | Eta |
|---|---|---|
| 1 | 0.00E+00 | 0 |
| 2 | 1.40E-05 | 0.5781 |
| 3 | 2.80E-05 | 0.875 |
| 4 | 4.20E-05 | 0.9844 |
| 5 | 5.60E-05 | 1 |
| 6 | 1.04E-03 | 0.0119 |
| 7 | 2.03E-03 | 0.0041 |
| 8 | 3.02E-03 | 0.0022 |
| 9 | 4.01E-03 | 0.0014 |
| 10 | 5.00E-03 | 0.001 |
| 11 | 1.00E+00 | 0 |
| 12 | 1.00E+01 | 0 |
| 13 | 1.00E+06 | 0 |

It could be said that there was already 1 resulting numerical to experimental ratios from the numerical analysis and can discuss the role of the DNN scheme here. There are several local maxima where a numerical outcome corresponds with an experimental result with a discrete parameter set. The DNN prediction precision is higher than random trial and error material model parameter selection.

The representation of FRC with numerical models includes difficulties, even more for the case of damage or fracture. This study employs a novel method to numerically represent FRC with an experimentally fitted DNN. The fitted DNN was used to make predictions that give the exact results for the single element numerical models. As a validation case, FRC four-point bending experimental test was modeled using the same DNN-acquired material model parameters. Four-point bending was selected as a validation case because it can capture the indirect tension behavior. The same FRC properties, as in fiber types and volume ratios, from the direct tension experimental tests, were selected for the bending case. The results were found to be quite similar considering the complex fracture mechanism of FRC material.

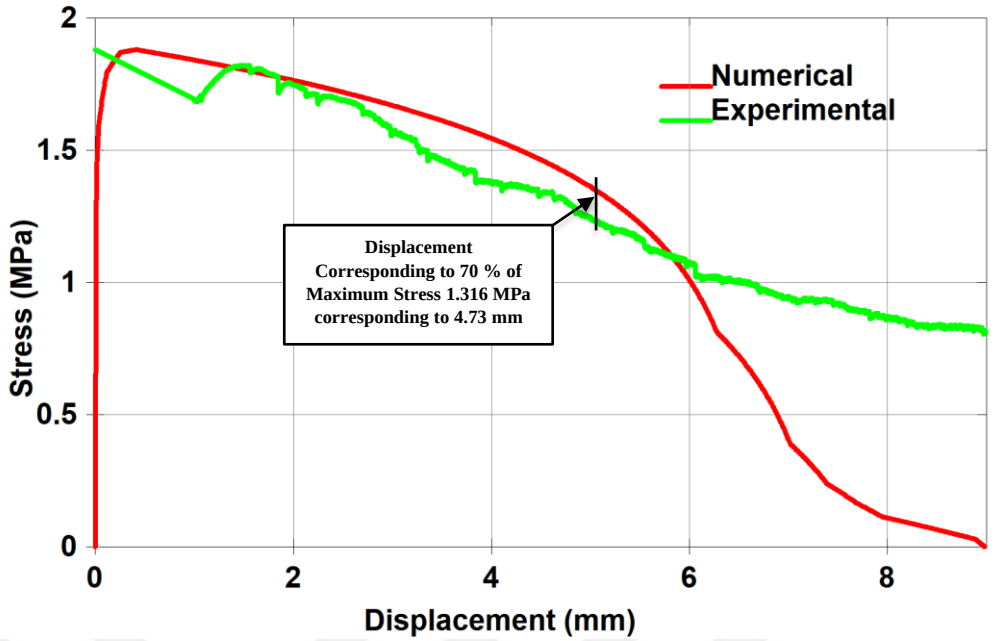


a)

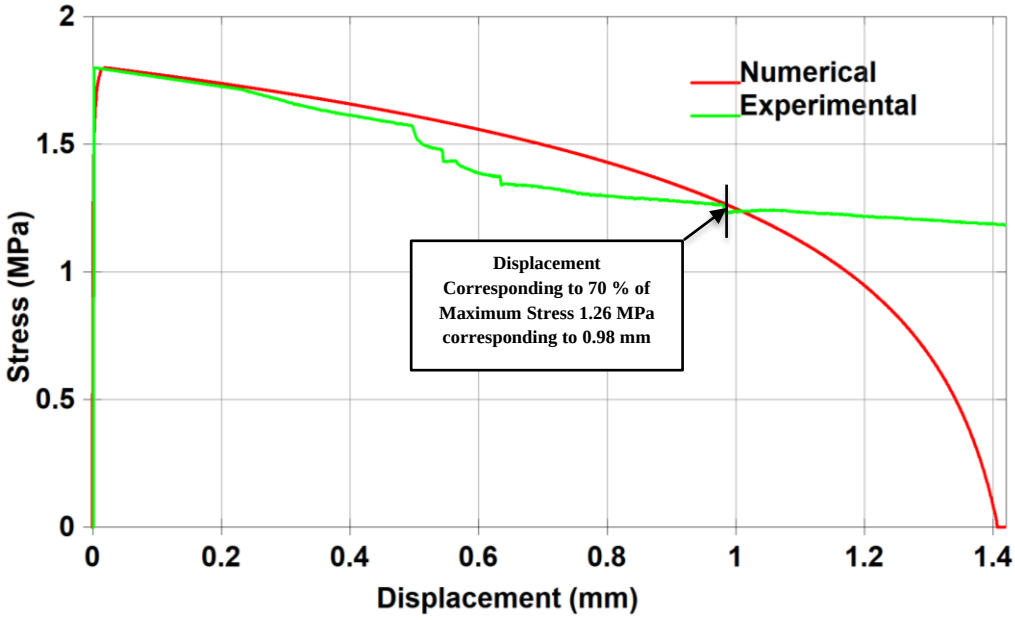


b)

Figure 3.10. Single element result of the numerical analysis of a) DT-M2 and b) DT-M1+PVA mixture

# CHAPTER 4

# FOUR POINT BENDING TESTS

## 4.1. Introduction

The fiber reinforced concrete material improves the tensile and flexural strength, and increases energy absorption and impact resistance (Herrmann et al., 2019; Caggiano et al., 2016; Chasioti and Vecchio 2017; Saatçi and Batarlar 2017; Çankaya and Akan 2023). The numerical simulation of fiber-reinforced concrete requires fracture properties (Wang, Wu, and Wang 2010; Wille, El-Tawil, and Naaman 2014). To investigate this, researchers have generally used uniaxial tension, and four-point bending tests (Kucewicz et al., 2022; Leutbecher and Rebling 2019; Mudadu et al., 2019; Oettel, Schulz, and Haist 2022; Tayfur, Saatcı, and Alver 2018)

In the previous chapter, uniaxial tension tests were used for the material model parameter search using Deep Neural Networks. Four-point bending numerical analysis was used as a verification of these material model parameters and the performance of Deep Neural Networks achieved parameters were investigated in this chapter. Experimental force-displacement, absorbed energy and damage behaviors were compared with the numerical results.

## 4.2. Four Point Bending Tests

Four-point bending tests on FRC panels were done by Aloui (2020). They have tested 1.25x0.5x0.05 m specimens with different fiber content under quasi-static bending loading. General view of the four-point bending test setup is presented in Figure 4.1. Loading at a rate of 1.5 mm/min was applied via two rollers on top with a 350 mm distance. Bottom supports were arranged to have simply supported boundary conditions with 900 mm clear space between them as presented in Figure 4.2. Load was applied by a displacement-controlled hydraulic actuator. Displacement was measured with two linear resistive position transducers at the midspan. Experimental tests were

done with a single specimen for each mixture. Material properties of the specimens are in Table 4.1.

Figure 4.1. Four-point bending test setup of (Aloui, 2020)

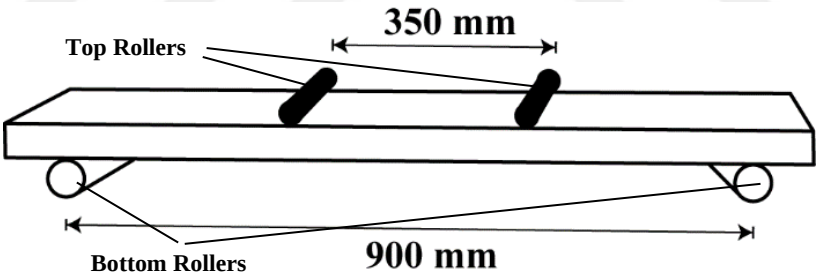


Figure 4.2. Dimension of the four-point bending experimental test setup

Table 4.1. Mixture properties of FRC mixtures of Aloui (2020)

| Specimen Name | Steel Fiber Ratio (%) | Steel Fiber Type | PVA Ratio (%) | Compressive Strength (MPa) |
|---|---|---|---|---|
| FB-M2 | 0.75 | 65/60 3D | - | 38.52 |
| FB-M1+PVA | 0.75 | 35/45 3D | 0.25 | 39.87 |

## 4.3. Numerical Modelling

The bending behavior of the beam was modeled with Karagozian and Case (K&C) material model in LS-DYNA. The parameters of the K&C material model were taken from the Deep Neural Network parameter search and the same parameters were used in the four-point bending modeling of FB-M2 and FB-M1+PVA specimens. The list of the individual parameters is given in Table 3.5 and Table 3.8 in Chapter 3. The omega and the localization width parameters used in the DNN search were used in the bending analysis.

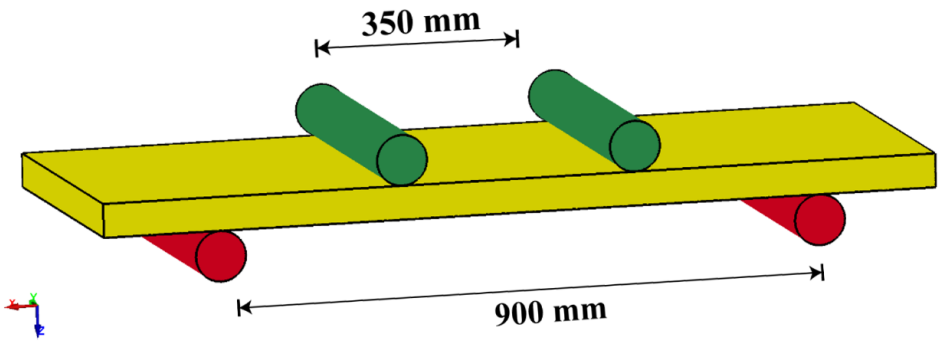


Figure 4.3. The illustration of four-point bending model

The dimensions and simply supported boundary conditions of the four-point bending tests were modeled exactly like the experimental tests using LS-PREPOST software. The complete numerical model in Figure 4.3 was presented for illustrative purposes.

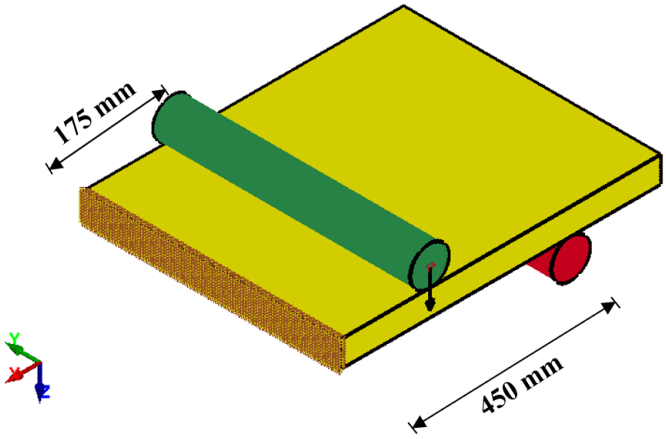


Figure 4.4. Symmetric boundary and the loading nodes of the bending numerical model

The presented numerical investigation and the results were done using a half four-point bending numerical model with symmetrical boundary conditions. Thus, the computational time was decreased by almost 50 % by cutting the model in half. The half model can be found in Figure 4.4. Eight-node 5 mm hexahedron elements were used to model the beam specimen which has the dimensions of 625x500x50 mm.

In the experimental tests, the distance between the top rollers was 350 mm and between the bottom rollers was 900 mm. The dimensions in the symmetrical model were taken as 175 from the top rollers to the symmetric boundary conditions, and 450 mm from the bottom rollers to the symmetric boundary conditions. MAT_ELASTIC card was prescribed to the top and bottom rollers with steel material properties.

LS-DYNA explicit solver has been used for the quasistatic bending analysis. The loading was applied in terms of velocity as 0.05 mm/ms. The method of time-scaling was applied to decrease to computational time. Mass scaling was not applied to the explicit analysis.

The BOUNDARY_ PRESCRIBED_ MOTION card in LS-DYNA helps impose rotational or translational velocity, acceleration, or displacement to a specified set of nodes (Manual 2013). A curve must also be prescribed for the motion. The top rollers were prescribed in a downward direction with the BOUNDARY_ PRESCRIBED_ MOTION card.

The contact card AUTOMATIC_SURFACE_TO_SURFACE is a two-way treatment contact that checks for penetration on the slave and master segments. It was prescribed between the panel and the rollers, as slave and master segments, respectively.

The contact stiffness is generally represented by linear springs between the adjacent slave and master segments. The default (SOFT = 0) contact stiffness in LS-DYNA is affected by the material properties of contacting sides, global time step size, and the mesh size. Thus, due to dissimilarities between the contacting materials in the four-point bending models, a soft constraint-based approach (SOFT = 2) (Belytschko and Neal 1991) was used for contact stiffness calculation. The soft-constraint method uses the nodal masses and the global time step size to calculate the contact stiffnesses.

Static and dynamic frictions were provided with contact definitions. High friction coefficients, 0.9 for both, were selected due to rough interaction surfaces between the steel boundary elements and the FRC surfaces (Tian et al., 2021; Kucewicz, Baranowski, and Małachowski 2020; Y. Wu et al., 2014; Rasmussen et al., 2020, Mardalizad et al., 2019).

To compare the force-displacement results with Aloui (2020), the CONTACT_FORCE_ TRANSDUCER card was adopted with the DATABASE_RCFORC card. Midpoint displacement was acquired with DATABASE_HISTORY_NODE and DATABASE_ NODOUT cards.

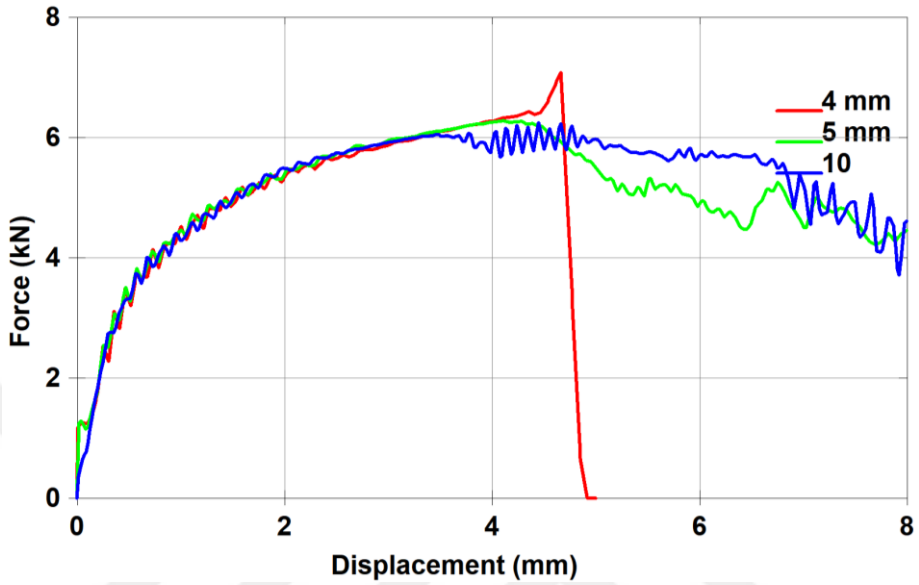


Figure 4.5. Force displacement graph of 4, 5 and 10 mm mesh sizes

Mesh sensitivity is an issue for concrete-like materials, and the behavior can change with the selected mesh size. As mentioned in Chapter 3.2, K&C material model proposes to be non-mesh dependent when its parameters are automatically generated. Such a process is done by regularizing the fracture energy by scaling the damage function according to Magallanes et al. (2010). However, because the K&C damage parameters were altered, the effect of mesh sizes at various values was tried and results are presented in Figure 4.5. Mesh sensitivity study, especially at smaller mesh values, is quite costly in terms of computational time. Thus, it was concluded for the mixture FB-M1+PVA, and 5 mm mesh size was selected for both FB-M1+PVA and FB-M2 mixtures.

## 4.4. Numerical Results

The following section contains the numerical results from the four-point bending analysis of FB-M2 and FB-M1+PVA mixtures in terms of force-displacement graphs, absorbed energy values and damage distributions in terms of tensile strains. The numerical and experimental results were evaluated to determine the performance of material parameter search using Deep Neural Networks with FRC material.

### 4.4.1. Displacement Histories

The experimental and numerical force-displacement graphs of four-point bending are given in Figure 4.6 and Figure 4.7. The maximum force values in numerical analysis and experimental tests are presented in Table 4.2 for FB-M2 and FB-M1+PVA mixtures.

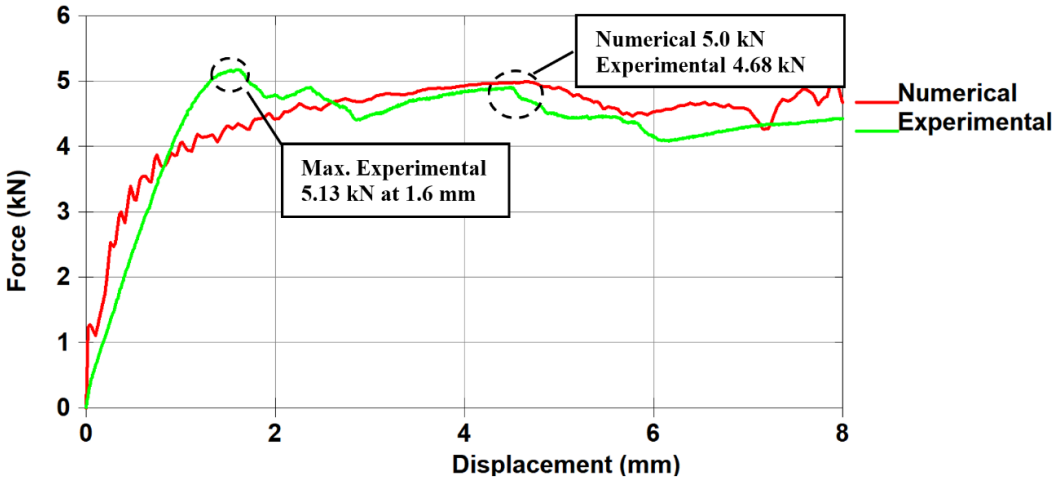


Figure 4.6. Force displacement graph of experimental and numerical four-point bending of FB-M2 mixture

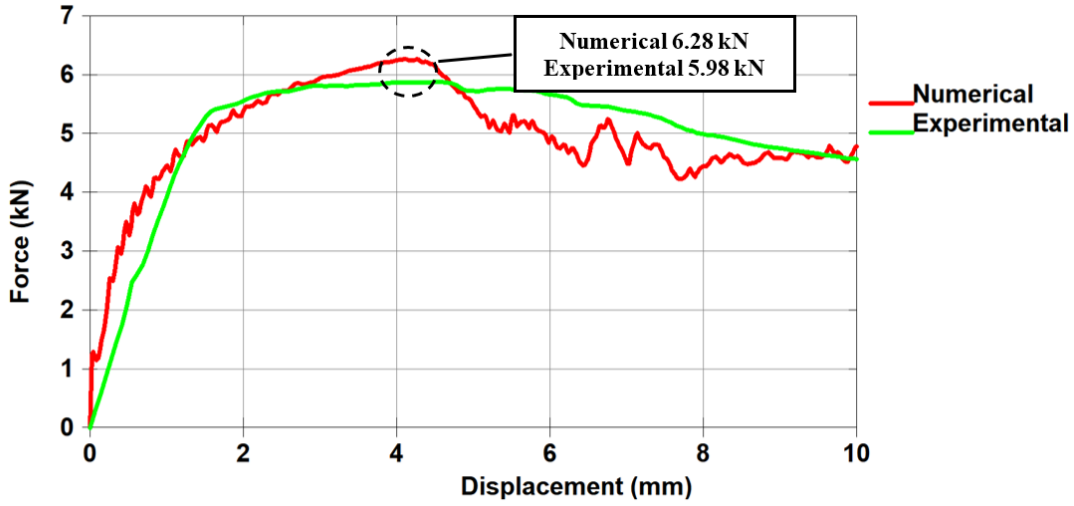


Figure 4.7. Force displacement graph of experimental and numerical four-point bending of FB-M1+PVA mixture

The numerical force-displacement results adequately reflect the experimental FRC bending behavior. Nevertheless, both FB-M2 and FB-M1+PVA mixtures' experimental force-displacement behavior show a stiff increase at the initial phase which lasts till a deflection of 4mm. The force values begin to drop slightly at the beginning of cracking due to the presence of fibers making the behavior ductile. This way, specimens show increased energy consuming capacity.

Table 4.2. The maximum force values in numerical analysis and experimental tests

| Specimen Name | Numerical Maximum Force (kN) | Experimental Maximum Force (kN) | Max Force Difference in % | Numerical Max. Force Displacement (mm) | Experimental Max. Force Displacement (mm) |
|---|---|---|---|---|---|
| FB-M2 | 5.0 | 5.13 | 2.5% | 4.68 | 1.6 |
| FB-M1+PVA | 6.28 | 5.98 | 5% | 4.28 | 4.58 |

The experimental maximum force result for the FB-M1+PVA mixture is 6.28 kN at 4.28 mm. The numerical analysis maximum force is 5.98 kN at 4.58 mm which shows a 5 % difference compared to maximum experimental value. The corresponding instances of the maximum force is really close for the numerical and the experimental case.

The maximum force in FB-M2 mixture goes up to 5 kN in the numerical analysis and displays a 3 % difference compared to experimental tests. However, the

corresponding displacement for the maximum force is quite different with 4.68 mm in the numerical analysis and 1.6 mm in the experimental result. The FB-M2 force - displacement graph in Figure 4.6 shows that there is a steep increase in the experimental result until 1.6 mm, then a strain-softening phase is observed due to multiple cracking in fiber hybridization. The location of the numerical maximum force value corresponds to 4.68 mm and the experimental value there is 4.87 kN which shows a 3 % discrepancy with the maximum numerical force.

There are quite a few reasons why experimental and numerical bending results may differ. Mainly, the shrinkage effects are present in the concrete during the drying and handling process and this causes microcracks in the concrete (Özcan et al., 2009). Said effect is not included in the numerical modeling process. Another reason could be the interaction between the fibers and mortar cause slipping and multiple cracking in the experimental tests. The numerical model takes a smeared approach and neglects these finer cracks.

### 4.4.2. Experimental and Numerical Absorbed Energy

The absorbed energy was calculated from the area under the force-displacement graphs. During the bending experiments of FB-M2, the maximum deflection was recorded as 8 mm. For consistency, the consumed energies of both the FB-M2 and FB-M1+PVA mixtures were investigated until 8 mm of deflection. The numerical and experimental energy absorptions of FB-M2 and FB-M1+PVA mixtures are listed in Table 4.3.

Table 4.3. The absorbed energy of FB-M2 and FB-M1+PVA mixtures at 8 mm deflection

| Specimen Name | Numerical Absorbed Energy (Joule) | Experimental Absorbed Energy (Joule) | Difference % |
|---|---|---|---|
| FB-M2 | 35.5 | 34.0 | 4.2 % |
| FB-M1+PVA | 40.5 | 41.0 | 1.2 % |

The numerical analysis of the FB-M2 mixture over approximates the absorption capacity by 4.4 %. On the other hand, the FB-M1+PVA mixture's numerical energy

absorption capacity underestimates it by 1.2 %. The observations show that the numerical analysis is very capable of capturing the energy absorption capacity.

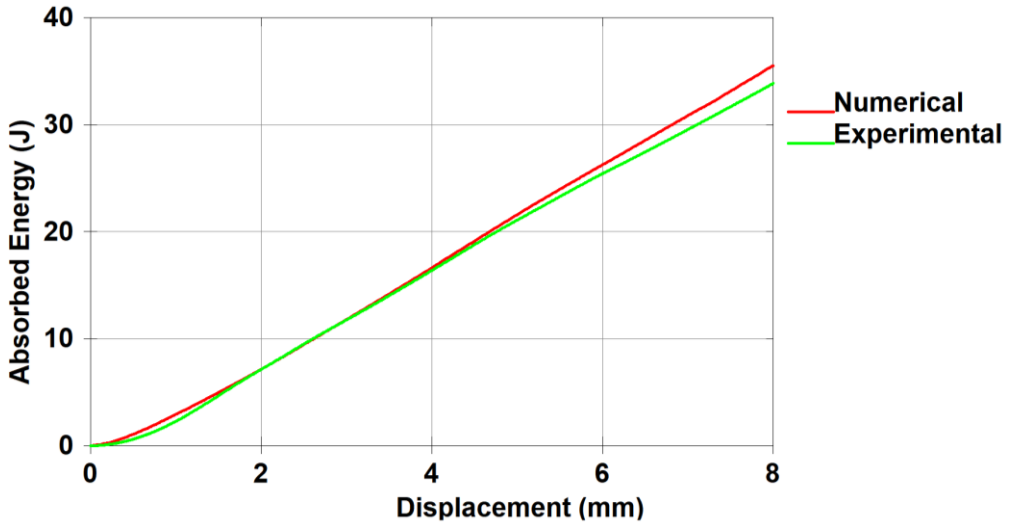


a)

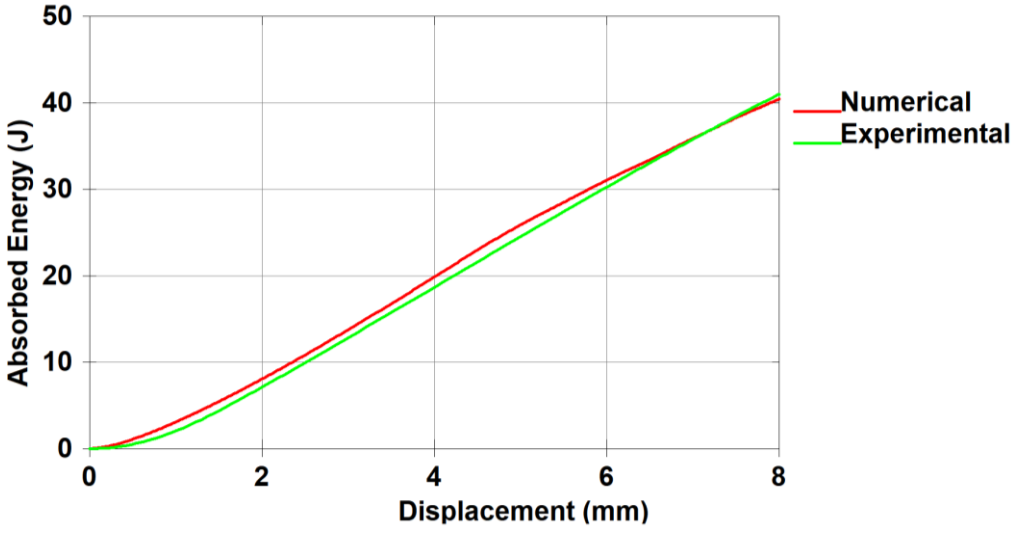


b)

Figure 4.8. Absorbed energy-displacement graph of a) FB-M2 and b) FB-M1+PVA mixture

Figure 4.8 shows the absorbed energy as a function of displacement for mixture FB-M2 and FB-M1+PVA. For both mixtures the numerical absorbed energy is quite similar to the experimentally achieved energy levels.

The initial absorbed energy is higher for the numerical model, because the numerical results include a stiff initial phase. The difference closes after 2 mm of displacement for FB-M2 mixture. However, for the FB-M1+PVA mixture the slight

difference between the numerical and experimental energies continues until 6mm of displacement. Nevertheless, the absorbed energy progress is quite parallel and even overlaps in certain locations. It could be said that the numerical models are quite capable of catching the absorbed energy levels.

### 4.4.3. Experimental and Numerical Damage Distributions

The experimental crack paths and the numerical damage distributions of the four-point bending tests were compared in the following section. The strain in the direction of the x axis was selected to be compared with the experimental crack paths. The x-direction strain corresponds to tension and shows distinct damage distributions. While the K&C material model is capable of showing the damage through the "Effective Plastic Strain" fringe, the individual cracks observed in the experiments were too smeared with the Effective Plastic Strain fringe.

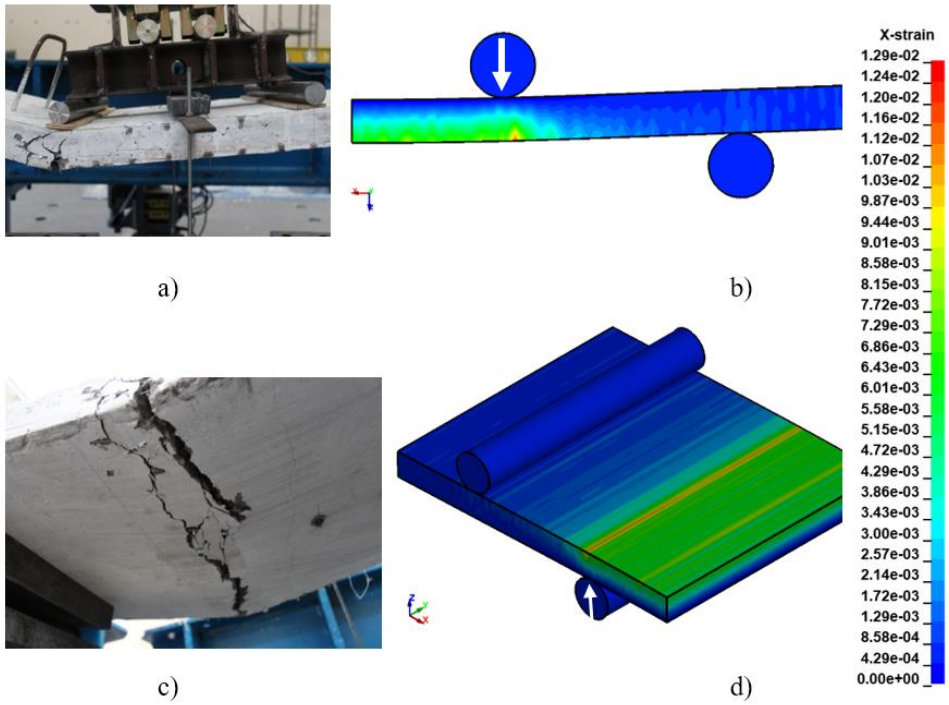


Figure 4.9. Tensile strains and crack paths of FB-M2 mixture, a) Crack path from the front view, b) Tensile strain localization at the side, c) Crack path from the bottom view, d) Tensile strain localization at the bottom

The FB-M2 specimen failed due to a large crack forming under the top during the experiments. Figure 4.9.a and Figure 4.9.c show multiple crack paths starting from the load applying pin towards the underneath of the specimen. Multiple cracking has given some ductility to the flexural behavior of FB-M2 specimen as seen from the force-displacement graph.

The numerical damage distribution shows a close fit to the experimental crack paths for the FB-M2 mixture. The strain in the x-direction shows the tensile strain localizations, which can be observed in Figure 4.9.b. The numerical model accurately captures the large crack formation under the top roller. The microcracks in the experiments were reflected on the side and bottom of the numerical damage distributions as well.

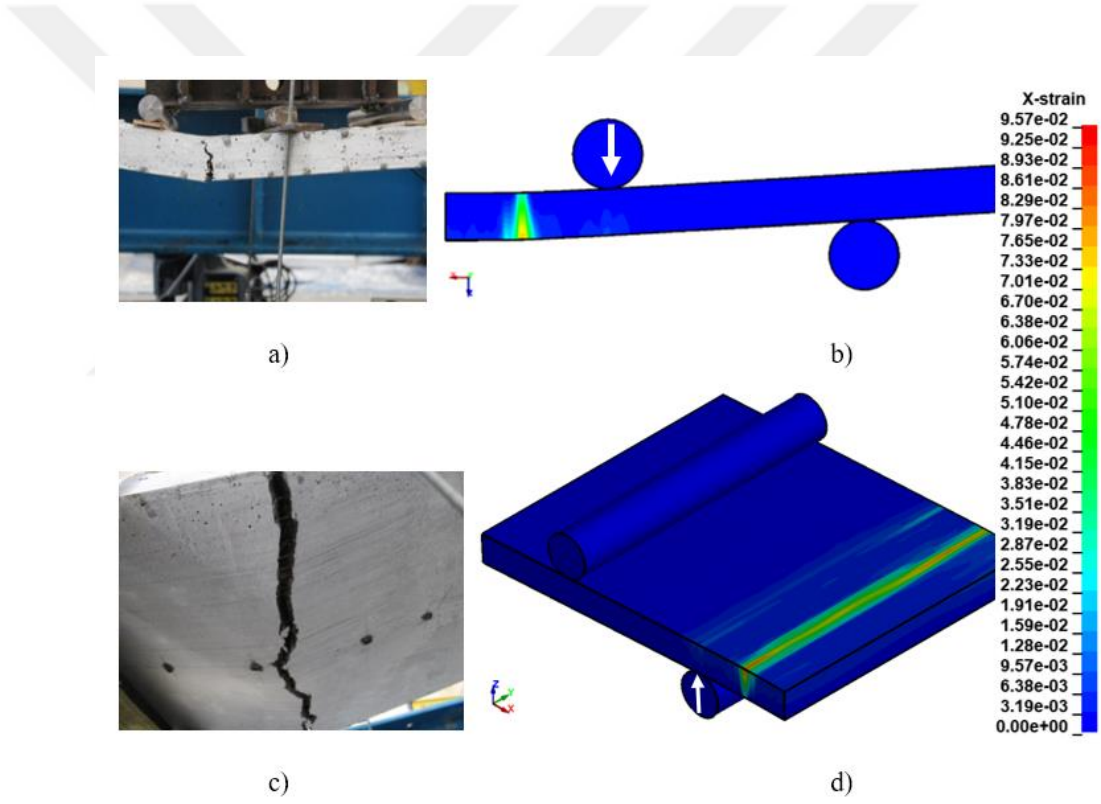


Figure 4.10. Tensile strains and crack paths of FB-M1+PVA mixture, a) Crack path from the front view, b) Tensile strain localization at the side, c) Crack path from the bottom view, d) Tensile strain localization at the bottom

The four-point bending experiment of the FB-M1+PVA specimen has failed with a large crack occurring at the constant moment region. The experimental observations show no multiple cracking. The force-displacement graph of the FB-

M1+PVA bending test (Figure 4.7) displays a very ductile behavior even though no multiple cracking has occurred. The ductility could have occurred due to the hybridization effect which happens when more fiber types show their positive attributes in one mixture. The numerical strain localization on the FB-M1+PVA specimen occurs in the constant moment region which is consistent with the experimental observations in Figure 4.10. The Figure 4.10.b shows that the crack path and the tensile strain localization are very compatible from the front angle. The numerical damage under the FB-M1+PVA specimen shows the single cracked line which matches the bottom of the FB-M1+PVA specimen in the experimental tests.

The experimental bending tests were done with single specimen for each mixture type. Thus, some possible irregularities have to be considered when experimental results are inspected such as uneven fiber distribution, cracking due to transportation or microcracks due to shrinkage effect. These irregularities are evident underneath the specimens in the experimental crack paths. The crack paths at the bottom side are ragged and don't coincide while the numerical damage localizes more like a straight line underneath the specimen.

In general, it can be said that DNN-acquired material model parameters yield decent results for loading conditions that they have not been trained for. The reason for the similarity between experimental and numerical results in bending can be attributed to the fact that the bending indirectly reflects the behavior of tension. Further study will investigate the DNN-acquired material model parameters on dynamic loading cases.

# CHAPTER 5

# SHOCK TUBE TESTS

## 5.1. Introduction

Under high-strain rates, fiber reinforced concrete (FRC) can exhibit different ductility, strain hardening, and energy absorption behavior compared to regular concrete. Numerical modeling is a good tool to investigate the structural behavior of FRC material. Current study verifies the numerical model of FRC panels subjected to impulsive blast loads generated by a shock tube. Employed concrete material model parameters were explicitly investigated with deep neural networks to reflect the fiber reinforced concrete behavior. Acquired experience enables the analysis and design of fiber reinforced concrete panels under blast loading through numerical modeling.

## 5.2. Shock Tube Tests

Using a shock tube to assess the blast performance of structural specimens is a reliable method that is also cost-effective and safe. Compared to open-field explosions, the shock tube test design enables more data acquisition during the blast phase and is reproducible. Depending on the test setup, shock tube tests can be performed on columns (Lloyd, 2011), beams (Jacques and Saatcioglu, 2020), walls (Bruhl, 2015) and slabs specimens (Kristoffersen et al., 2016; Jacques, Lloyd, and Saatcioglu, 2013; Thiagarajan et al., 2015) just to name a few. Researchers have used shock tube blast testing to investigate the behavior of steel fiber reinforced concrete columns (Burrell 2012), steel fiber reinforced concrete beams (Lee et al., 2018), reinforced concrete columns retrofitted with carbon fiber reinforced polymer (Lloyd, 2011), and ultra-high performance fiber-reinforced concrete jacketing with reinforced concrete columns (Lee et al., 2020).

In order to investigate the FRC panel behavior under blast loading, Alkabbani (2021) used concrete panel specimens with hybrid synthetic and steel fibers. 1900x1900x50 mm panel specimens were tested under blast load using a shock tube test

device (Figure 5.1). Specimens ST-M1+PVA (Shock Tube Mix 1 with PVA) and ST-M2 (Shock Tube Mix 2) mixture properties are given in Table 5.1.

Table 5.1. Mixture properties of FRC mixtures of (Alkabbani, 2021)

| Specimen Name | Steel Fiber Ratio (%) | Steel Fiber Type | PVA Ratio (%) | Compressive Strength (MPa) |
|---|---|---|---|---|
| ST-M2 | 0.75 | 65/60 3D | - | 46.8 |
| ST-M1+PVA | 0.75 | 35/45 3D | 0.25 | 47.1 |

The panel specimens were provided with simply supported boundary conditions on the test frame of the shock tube test setup. Three holes were drilled on specimen's each side to pass steel rods through. Rods were then connected to a rigid setup frame with spherical washers that provide rotational freedom to the specimen but restrict movement in the normal direction. Detail of the support point with spherical washer is in Figure 5.2.

a)

b)

Figure 5.1. General view of the shock tube, a) back view, b) top view

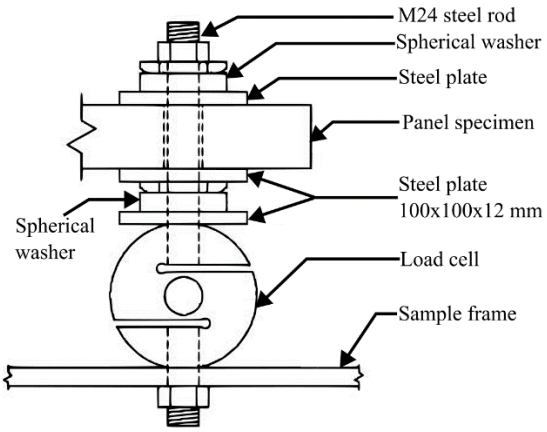


Figure 5.2. Detail of the support point with spherical washer (Alkabbani, 2021)

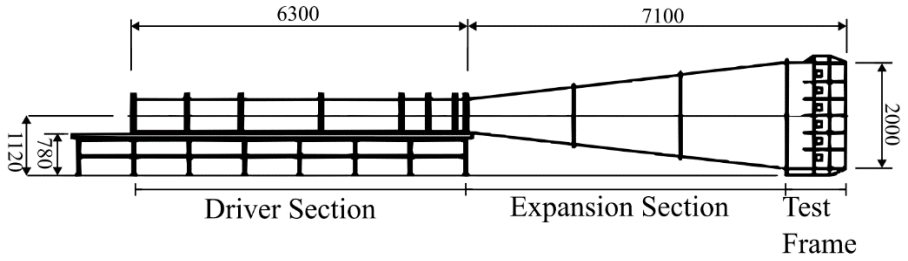


Figure 5.3. Shock tube sections (all dimensions in mm)

The shock tube test setup is capable of simulating blast loads in laboratory conditions. It is comprised of driver, expansion, and end frame sections (Figure 5.3). The high-pressure air is filled to the air-tight driver section by a compressor. The driver section has various length options, to vary the total generated impulse, with a maximum length of 6.3 m. Driver can be pressurized up to 11 bars. At the end of the driver section, aluminum sheets are attached to divide the driver from the expansion section. When these sheets rupture at their predetermined strengths, high-pressure air goes through the expansion section and hits the specimen. The expansion section provides a uniform pressure instead of a spherical pressure wave. Panel specimen is mounted to the far end of the expansion section, equipped with 12 loadcells, 5 resistive linear position transducers (RLPT), 8 accelerometers, and 2 surface pressure gages. During the experiment, data was gathered with a high-speed data acquisition system that can save data at a speed of 250000 data/channel/second.

Pressure sensors on the specimens recorded reflected pressures at the middle and corner points of the specimens. Both recordings generally gave almost identical results, indicating a uniform pressure distribution on specimens. Recorded reflected pressure –

time graphs are presented in Figure 5.4 for ST-M2 and ST-M1+PVA blasts. Displayed pressure data is the average of two surface pressure gages that was set through low-pass filter at 400 Hz.

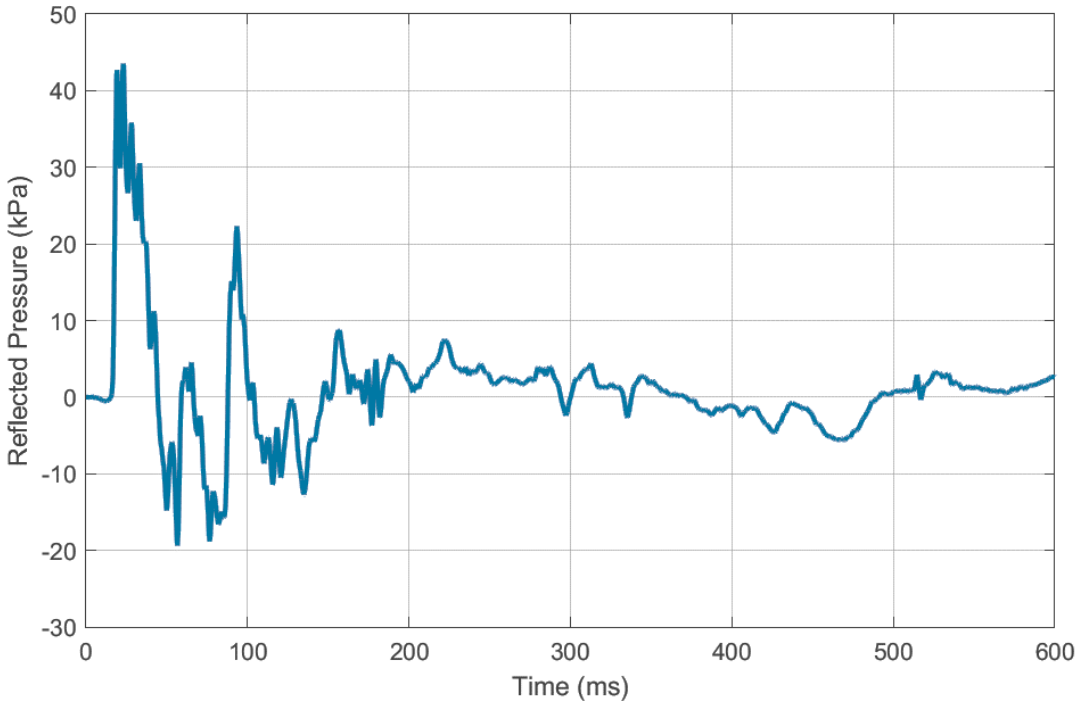


a)

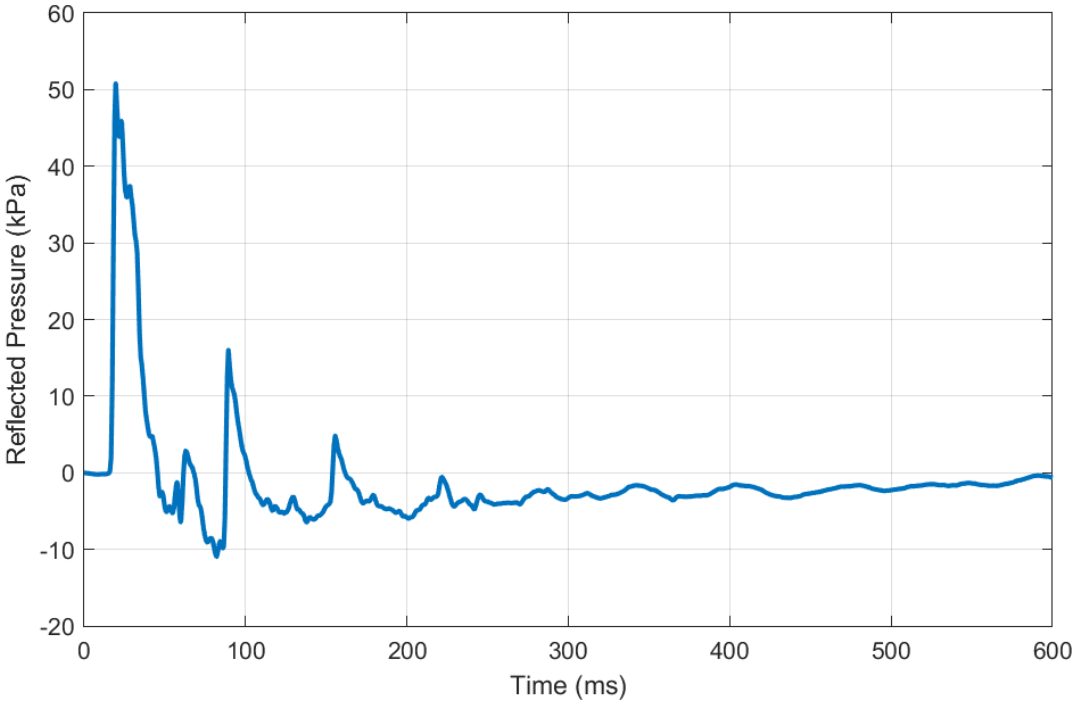


b)

Figure 5.4. Reflected pressure-time graphs of the a) ST-M2 blast b) ST-M1+PVA blast

Subsequently, the chapter investigates the numerical analysis of FRC panels under blast loads using the Karagozian and Case (K&C) material model parameters that were calibrated through Deep Neural Networks (DNN). For that process, an idealized linearly decreasing triangular pressure profile was not preferred, as this oversimplification approach neglected the negative pressure effect of the experiment. Thus, the current numerical process includes the complete reflected pressure-time data as blast loading. This way, higher accuracy was achieved in the numerical simulation.

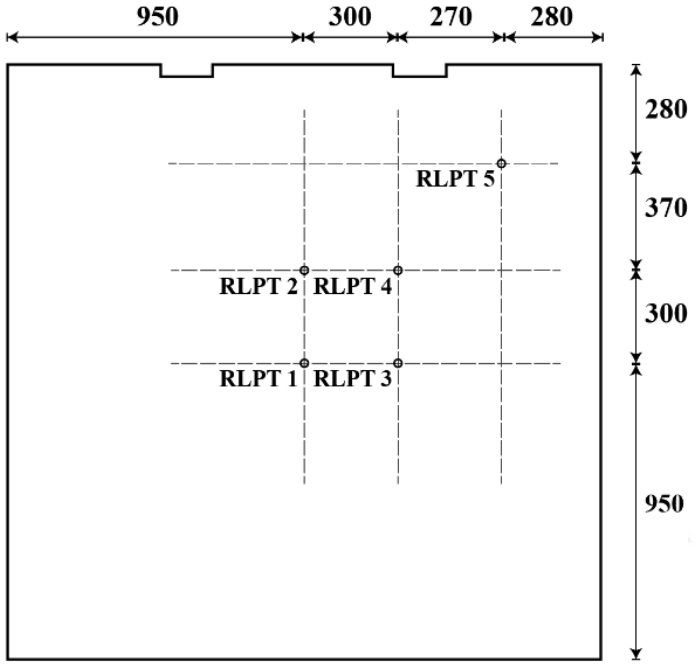


Figure 5.5. RLPT locations on the specimen (all dimensions in mm)

The displacement profile of FRC specimens were recorded through 5 RLPTs displayed in Figure 5.5. Displacements achieved from the experimental tests are given in Figure 5.6 and Figure 5.7. In some cases, RLPTs' capacity was exceeded during blast tests, and the full displacement profile was not captured. As a consequence, the acceleration recording was converted to a displacement value by the direct integration method. The maximum midpoint displacement of ST-M1+PVA specimen was calculated with the mentioned method as 117 mm.

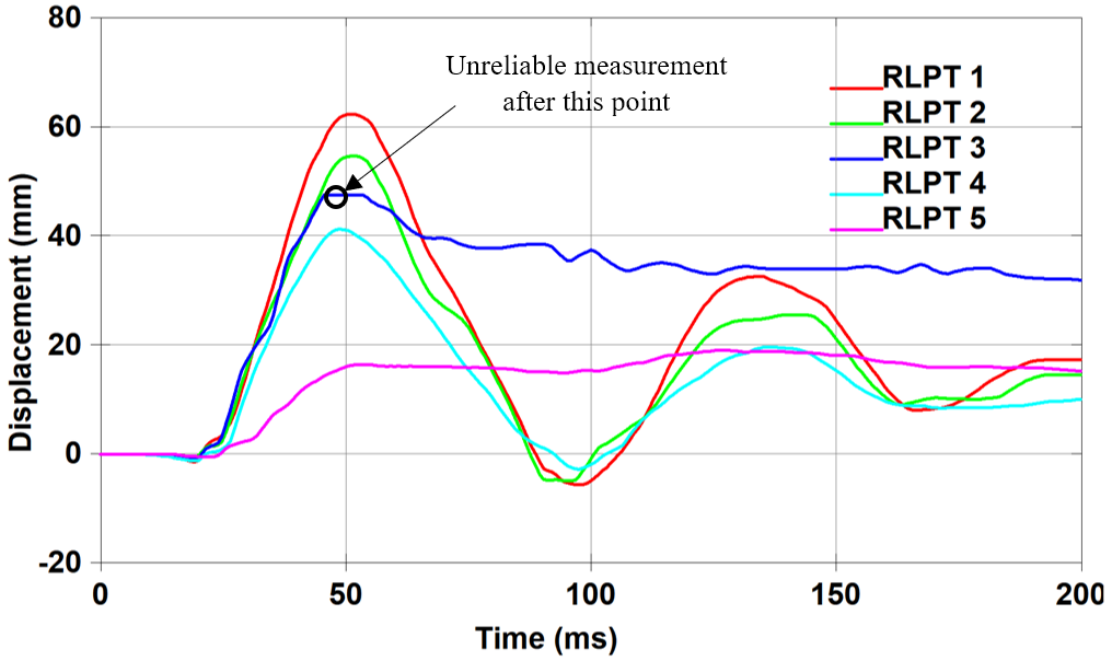


Figure 5.6. Experimental displacement profiles of ST-M2

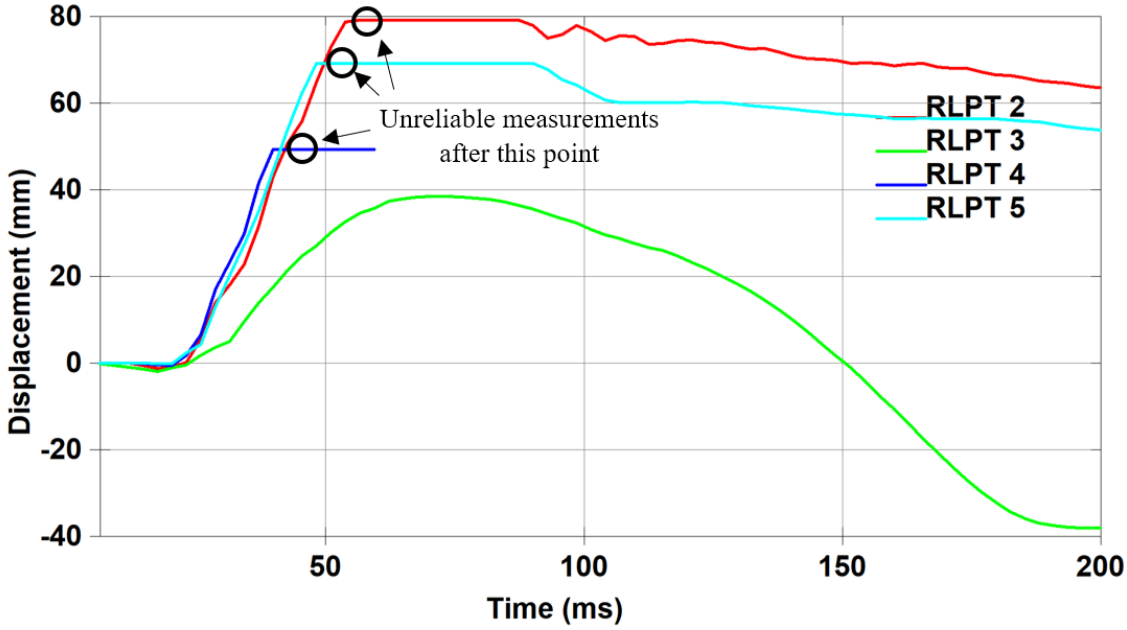


Figure 5.7. Experimental displacement profiles of ST-M1+PVA

## 5.3. Numerical Modelling

Numerical modeling is a good tool to investigate the blast load of FRC panels. Kristoffersen et al. (2018) have used LS-DYNA to model concrete slabs under shock tube induced blast load and included a parametric study with tensile and compressive strength variants. Nawar et al. (2015) investigated the shock-tube tested laminated glazing using LS-DYNA. Sherif et al. (2022) demonstrated the performance of ultra-high performance fiber reinforced concrete under shock-tube induced blast loading with numerical modeling. Maazoun et al. (2018) numerically investigated the carbon fiber reinforced polymer retrofitting to reinforced concrete slabs with LS-DYNA.

The previously described shock tube tests of Alkabbani (2021) were numerically investigated below. FRC panel specimens were modeled with the finite element program LS-DYNA. 1900x1900x50 mm specimen was constructed with 10x10x10 mm eight-node hexahedron elements.

During the experimental specimen manufacturing process, voids were left in the formwork for anchoring transportation hooks. These voids were generated in the numerical model as well, as seen in Figure 5.8, since experimental crack paths have shown that damage initiates from these locations.

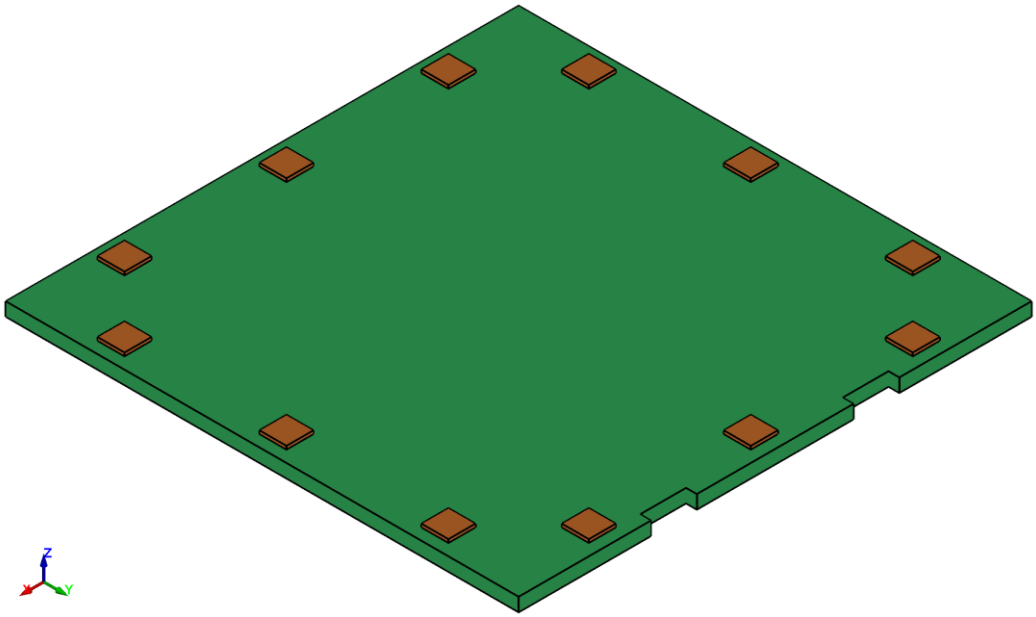

Figure 5.8. General view of the numerical model

The panel specimens were provided with simply supported boundary conditions. Corresponding to the support points of the experimental test setup, 10x10 cm steel plates were modeled on the top and bottom of the panel. 3 mm distance was kept between the steel plates and the panel to prevent any prestressing condition during blast loading. Massless rivets were defined between the node pairs of top and bottom steel plates (Figure 5.9) using CONSTRAINED_RIVET card. Thus, the distance between the top and bottom steel plates was kept constant during loading while allowing rotations. The top middle points of the steel plates were restricted in translational movement but rotations were allowed. MAT_ELASTIC was assigned to the top and bottom steel plates with steel material properties.

The Karagozian and Case (K&C) material model was used for the reinforced concrete panels. FRC mixtures' material properties were taken as identical to the parameter set found from the DNN calibration in Chapter 3 Table 3.5 and Table 3.8. The Tabulated Compaction Equation of State was selected for the mixtures as well, and their parameter set was selected equal to DNN calibration. LCRATE parameter in the K&C material model was changed to "-1" to incorporate the strength enhancement under high-strain rate effects (Y. Wu and E.Crawford 2015). The omega and the localization width parameters were taken as 0.9 and 55, respectively. A sensitivity study was done to select these values.

Between the steel plates and panel specimen, the CONTACT_AUTOMATIC_ SURFACE_ TO _SURFACE contact card was assigned, with static and dynamic friction coefficients of 0.9 and 0.9. The contact card and friction coefficients specified in this study are consistent with the numerical modeling details of the FRC four-point bending numerical analysis presented in Chapter 4.

Reflected pressure-time data, as presented in Figure 5.4, was applied to panel surface nodes as force. LOAD_NODE card was used to apply the force to the nodes. CONTROL_ENERGY and CONTROL_HOURGLASS cards are also added to the numerical model as control cards.

Five nodes were prescribed to the DATABASE_HISTORY_NODE and DATABASE_ NODOUT cards at RLPT locations as displayed in Figure 9. Due to technical problems, the midpoint displacement (RLPT1) of ST-M1+PVA mixture was not captured. Thus, only the maximum displacement value calculated from acceleration data was used for comparison for this location.

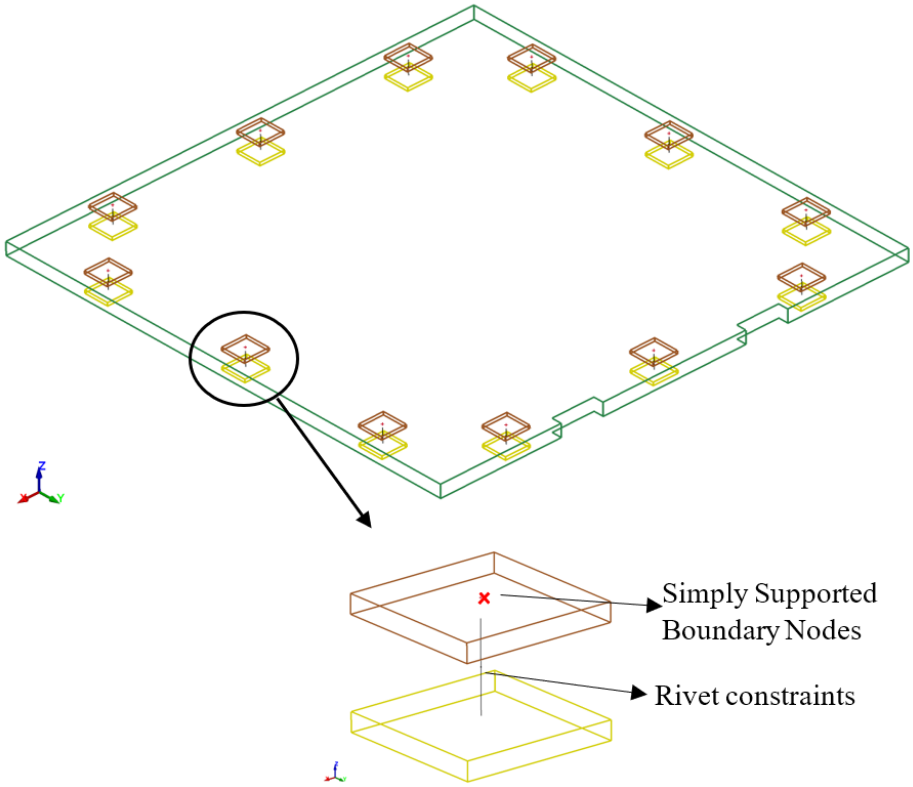


a)

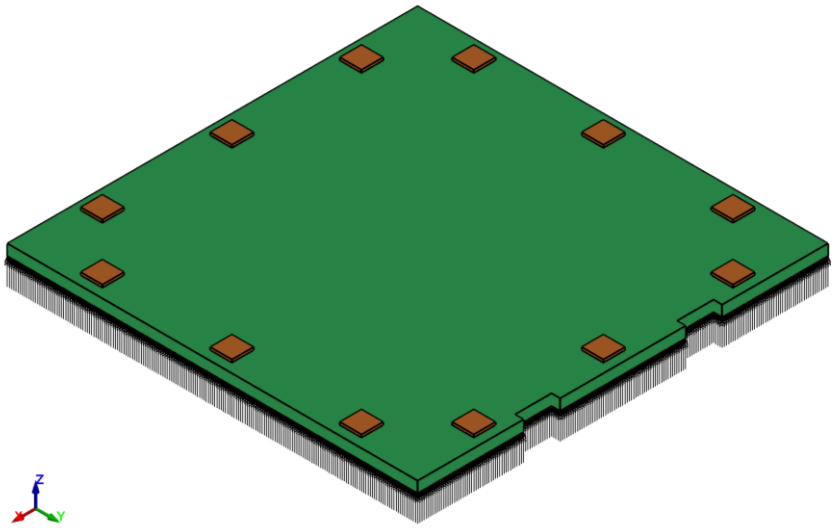

b)

Figure 5.9. a) Boundary properties with close-up and b) applied load details of the numerical model

## 5.4.Numerical Results

The experimental and numerical displacement results are given in Figure 5.10 through Figure 5.18. The maximum displacements and their corresponding times are given in Table 5.2 and Table 5.3 with the differences between the numerical and experimental values. The damage distribution from the numerical analysis and the experimental crack paths are shown in Figure 5.19 through Figure 5.26.

### 5.4.1. Displacement Histories

The RPLT results of experimental and numerical displacements fit well in terms of initial stiffness. The estimation of maximum displacements with the numerical analysis gives acceptable results. The best estimation is RLPT 5 in ST-M2 mixture with 2 % discrepancy, whereas the discrepancy for RLPT 3 and 4 reached up to 48%. The peak displacement instances of the experimental and the numerical results fit very well.

Table 5.2. ST-M2 Numerical and experimental differences in peak displacements

| | **Numerical Maximum Displacement (mm)** | **Experimental Maximum Displacement (mm)** | **Displacement Difference in %** | **Numerical Max. Displacement Time (ms)** | **Experimental Max. Displacement Time (ms)** |
|---|---|---|---|---|---|
| **RLPT1** | 85.6 | 62.3 | 37% | 50.4 | 49.3 |
| **RLPT2** | 69 | 54.7 | 26% | 50.4 | 49.3 |
| **RLPT3** | 70.3 | >47.5 | - | 50.4 | 50.9 |
| **RLPT4** | 61.3 | 41.5 | 48% | 50.4 | 48.9 |
| **RLPT5** | 16 | 16.3 | 2% | 47.6 | 48.6 |

Table 5.3. ST-M1+PVA Numerical and experimental differences in peak displacements

| | Numerical Maximum Displacement (mm) | Experimental Maximum Displacement (mm) | Displacement Difference in % | Numerical Max. Displacement Time (ms) | Experimental Max. Displacement Time (ms) |
|---|---|---|---|---|---|
| **RLPT1** | 132 | 117 | 13% | - | - |
| **RLPT2** | 117 | >79.1 | - | - | - |
| **RLPT3** | 111 | >69.2 | - | - | - |
| **RLPT4** | 102 | >49.3 | - | - | - |
| **RLPT5** | 30.2 | 38.5 | 22% | 64.4 | 63.5 |

During experimental tests, some RLPT capacities were exceeded, as presented in Figure 5.12, Figure 5.15, Figure 5.16, and Figure 5.17. The initial stiffness of the experimental displacement results fit well with the numerical findings. Additionally, the RLPT 1 record of the ST-M1+PVA specimen was not obtained because its capacity was exceeded. The maximum midpoint was calculated as 117 mm through direct integration of the acceleration data.

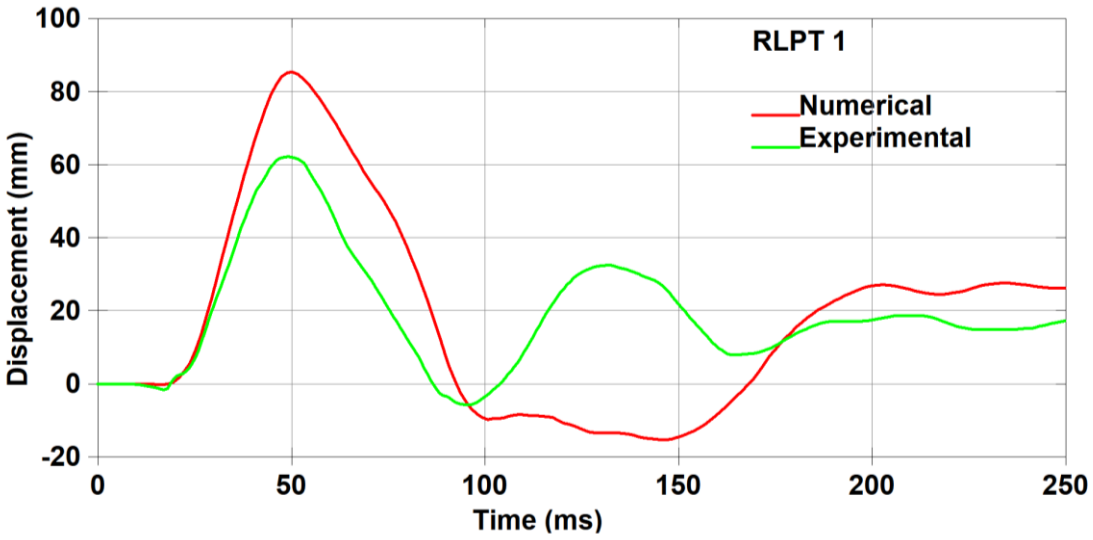


Figure 5.10. ST-M2 specimen's numerical and experimental displacements at RLPT 1

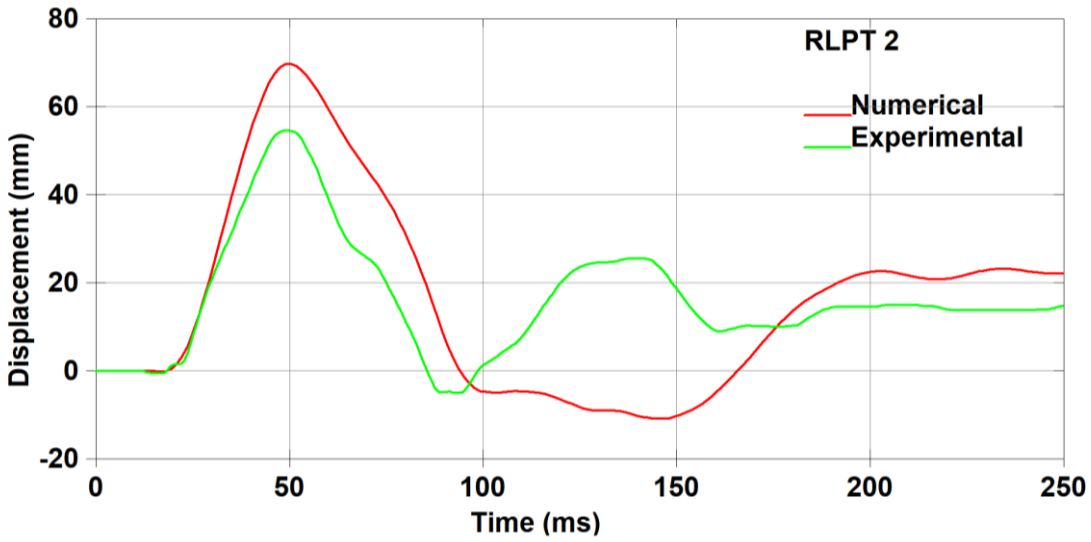


Figure 5.11. ST-M2 specimen's numerical and experimental displacements at RLPT 2

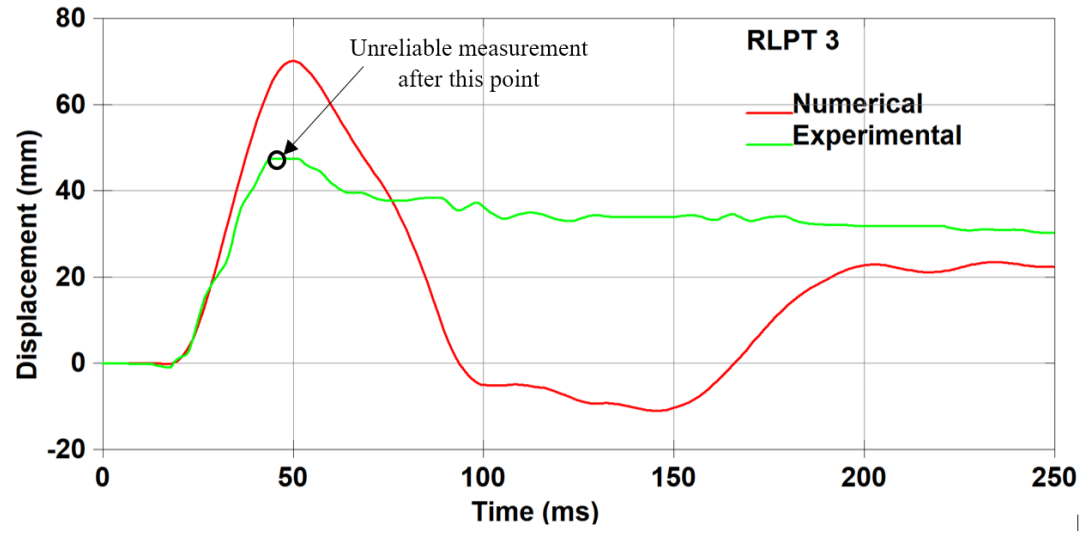


Figure 5.12. ST-M2 specimen's numerical and experimental displacements at RLPT 3

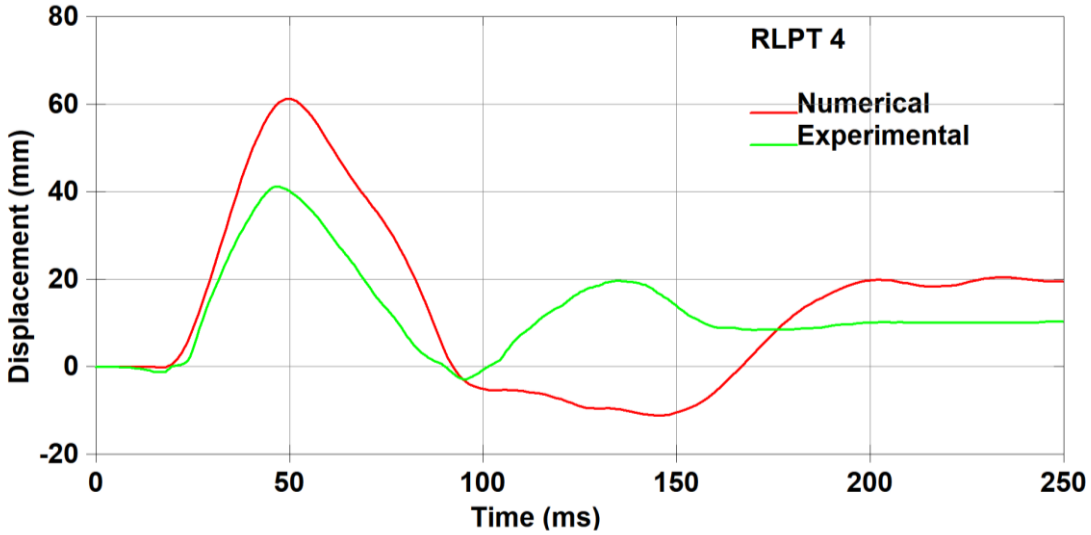


Figure 5.13. ST-M2 specimen's numerical and experimental displacements at RLPT 4

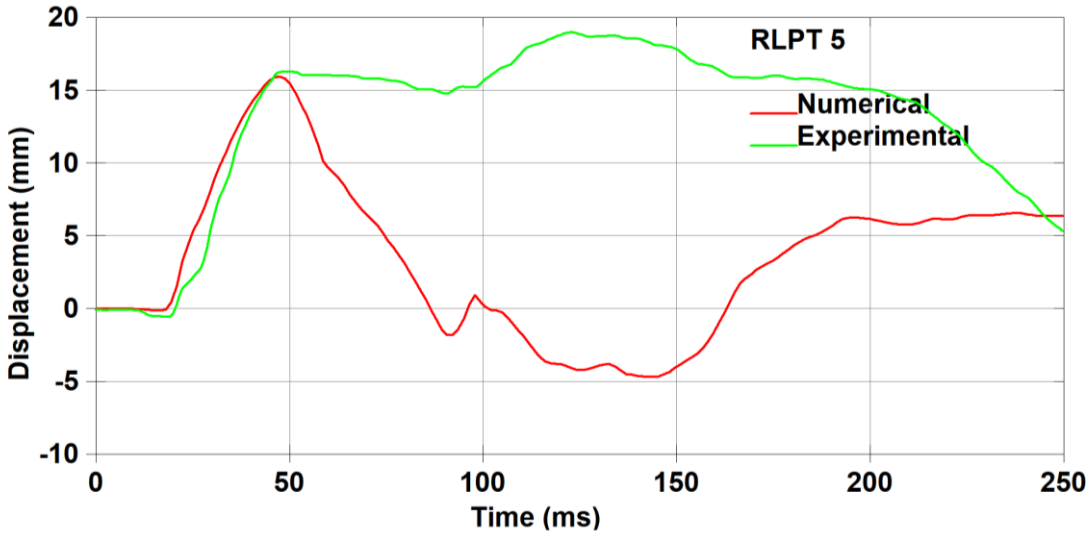


Figure 5.14. ST-M2 specimen's numerical and experimental displacements at RLPT 5

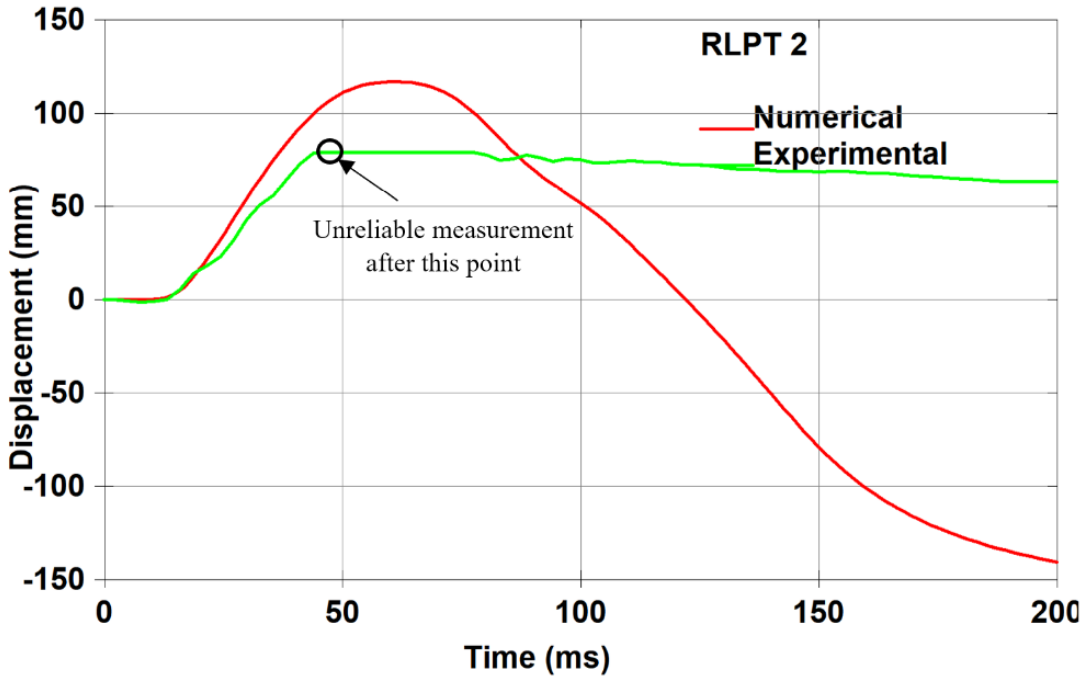


Figure 5.15. ST-M1+PVA specimen's numerical and experimental displacements at RLPT 2

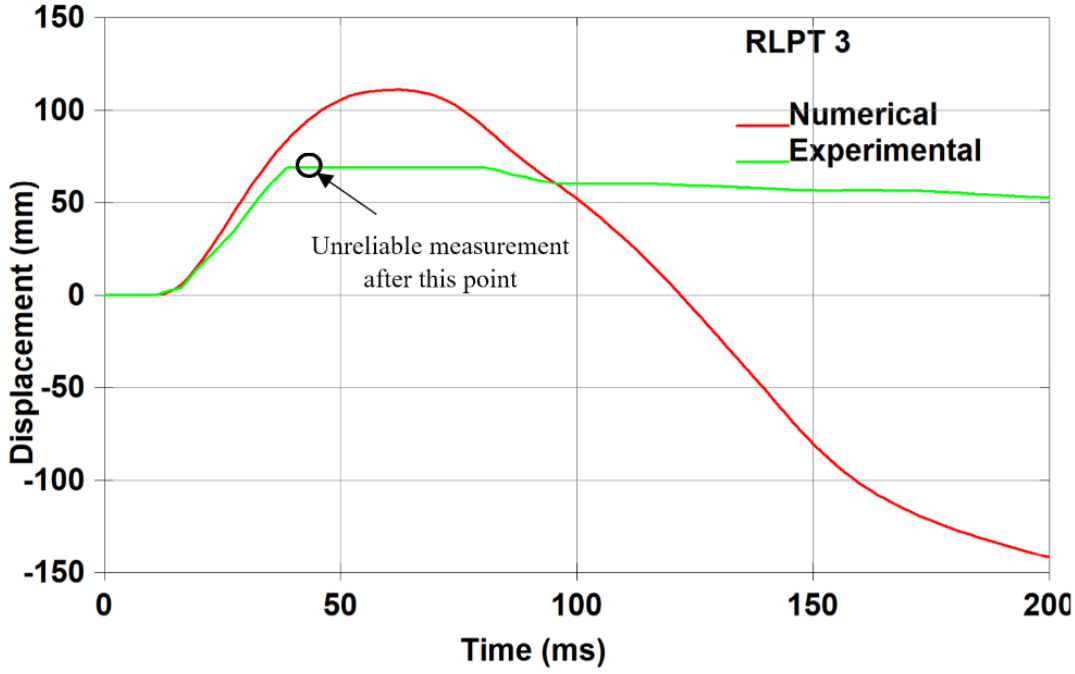


Figure 5.16. ST-M1+PVA specimen's numerical and experimental displacements at RLPT 3

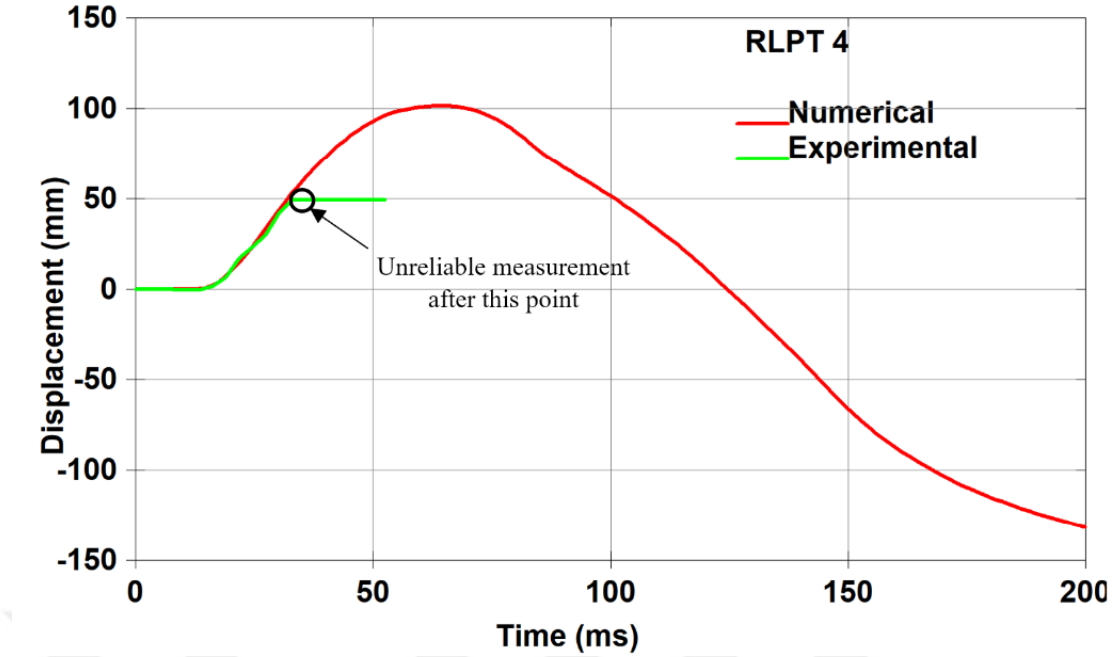


Figure 5.17. ST-M1+PVA specimen's numerical and experimental displacements at RLPT 4

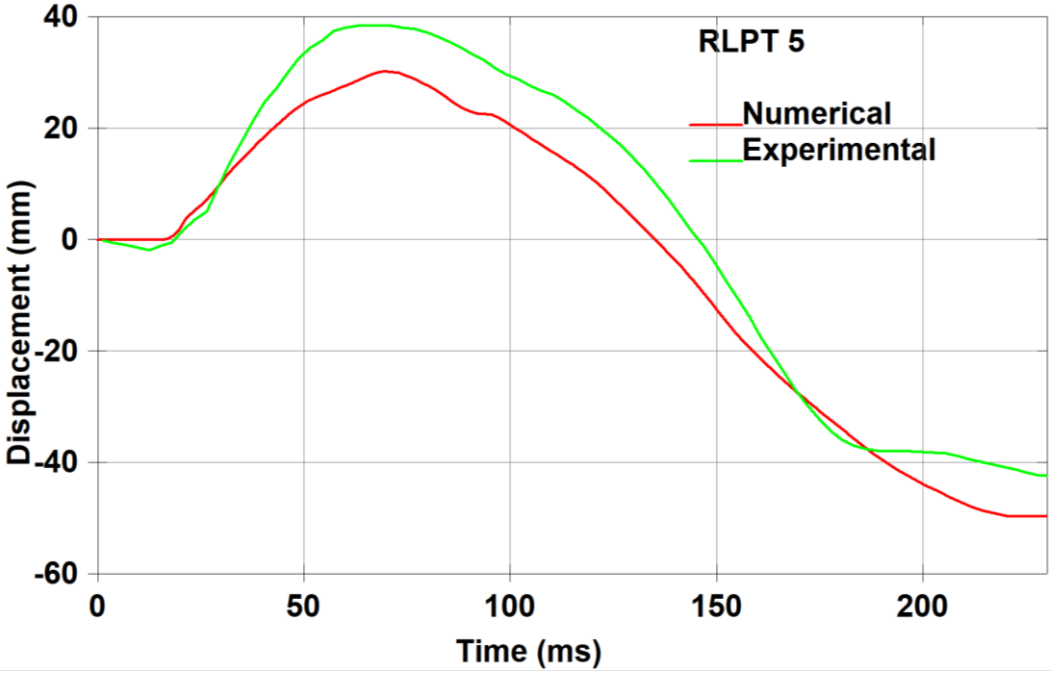


Figure 5.18. ST-M1+PVA specimen's numerical and experimental displacements at RLPT 5

### 5.4.2. Numerical Damage Distribution

The K&C material model is capable of providing effective plastic strain fringe plots, which indicate each element's damage levels. 0 to 1 indicates the failure surface reaching the maximum strength surface, and 1 to 2 means reaching the residual strength surface. Below, the numerical damage distributions were discussed, followed by the experimental crack and numerical damage comparisons.

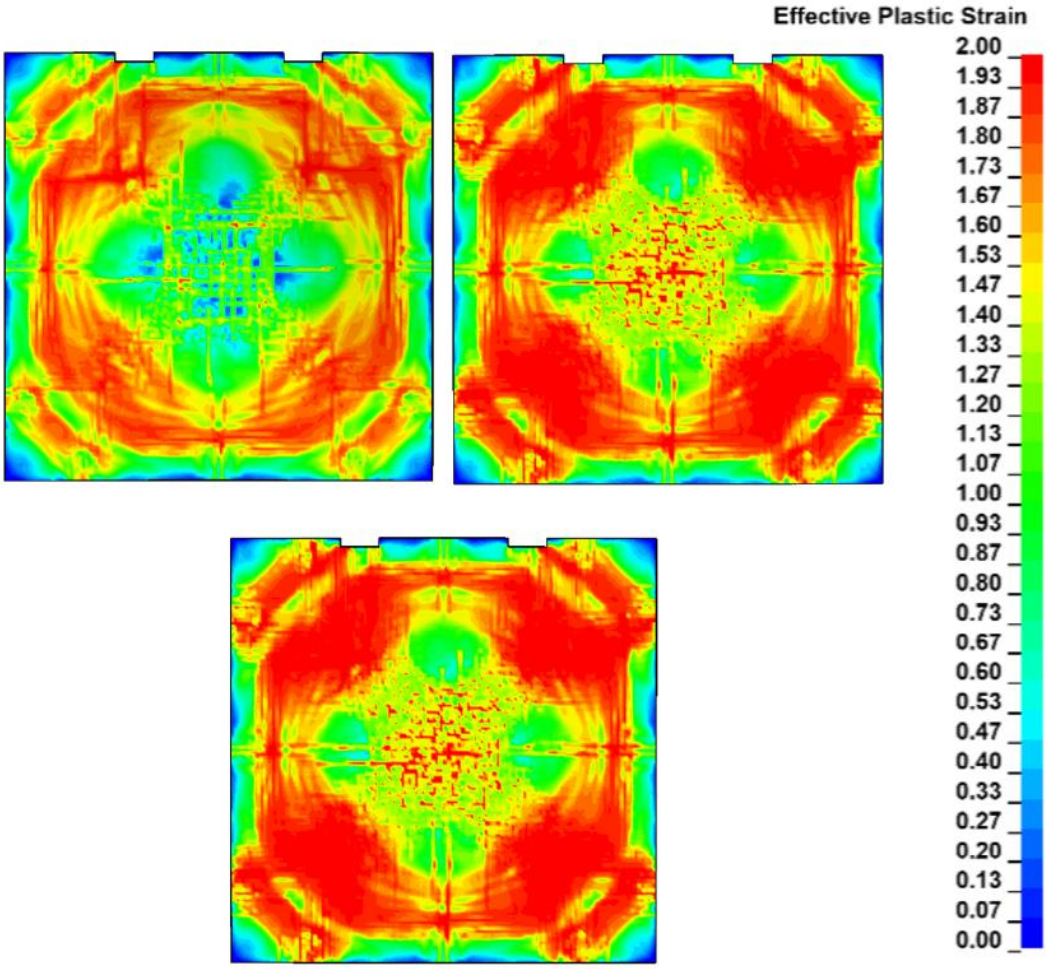


Figure 5.19. Numerical damage distributions of ST-M2 specimen's front face, at 67 ms, 300 ms, and 450 ms

The blast loading was applied directly to the specimen's front side as a normal force. The numerical damage distributions on ST-M2 specimen's front side show a circular shape during the loading phase (Figure 5.19). The holding places on the specimen cause additional crack paths leading to diagonal cracks. The middle part on specimen's front side shows dispersed damage levels though not complete damage. At

450 ms, specimen's front side shows approximately unified large areas of damage, although the middle of the specimen still shows dispersed in complete damage. The steel plates, which were used as the boundary elements in the experimental phase, cause stress concentration beginning from peripheral sides towards the middle of the specimen.

The numerical damage at specimen's front face displays the damage is mainly caused by boundary locations. The full scope of specimen's capacity is not used, which corresponds with experimental tests where another blast loading was done to the specimen.

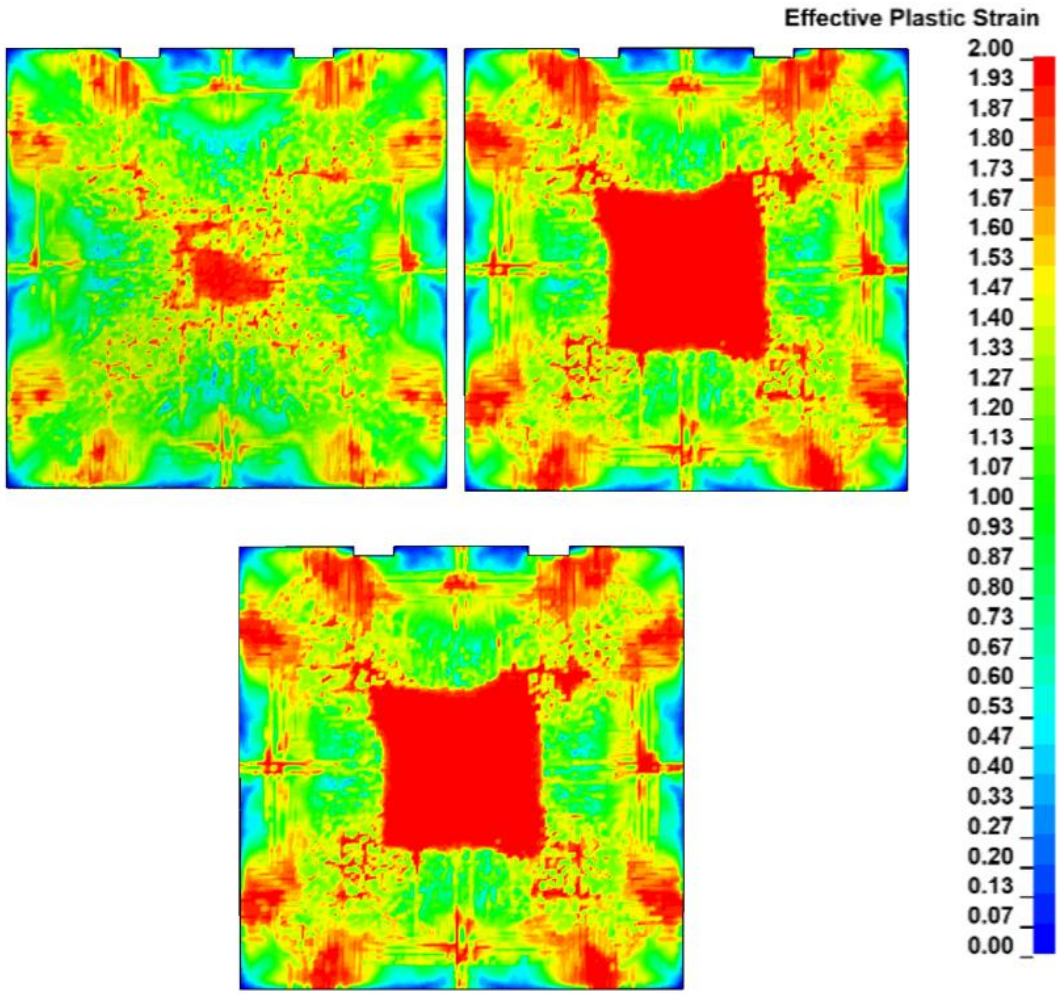


Figure 5.20. Numerical damage distributions of ST-M2 specimen's back face, at 67 ms, 300 ms, and 450 ms

ST-M2 Specimen's back side shows explicit damage localized around boundary locations and specimen's mid-point (Figure 5.20). The back side of the specimen is

where tensile stresses were dominant, especially at the instance of loading. Thus, the middle of the specimen displays a widely damaged area focused on a rectangle shape. After 300 ms, damage did not progress further at specimen's back face.

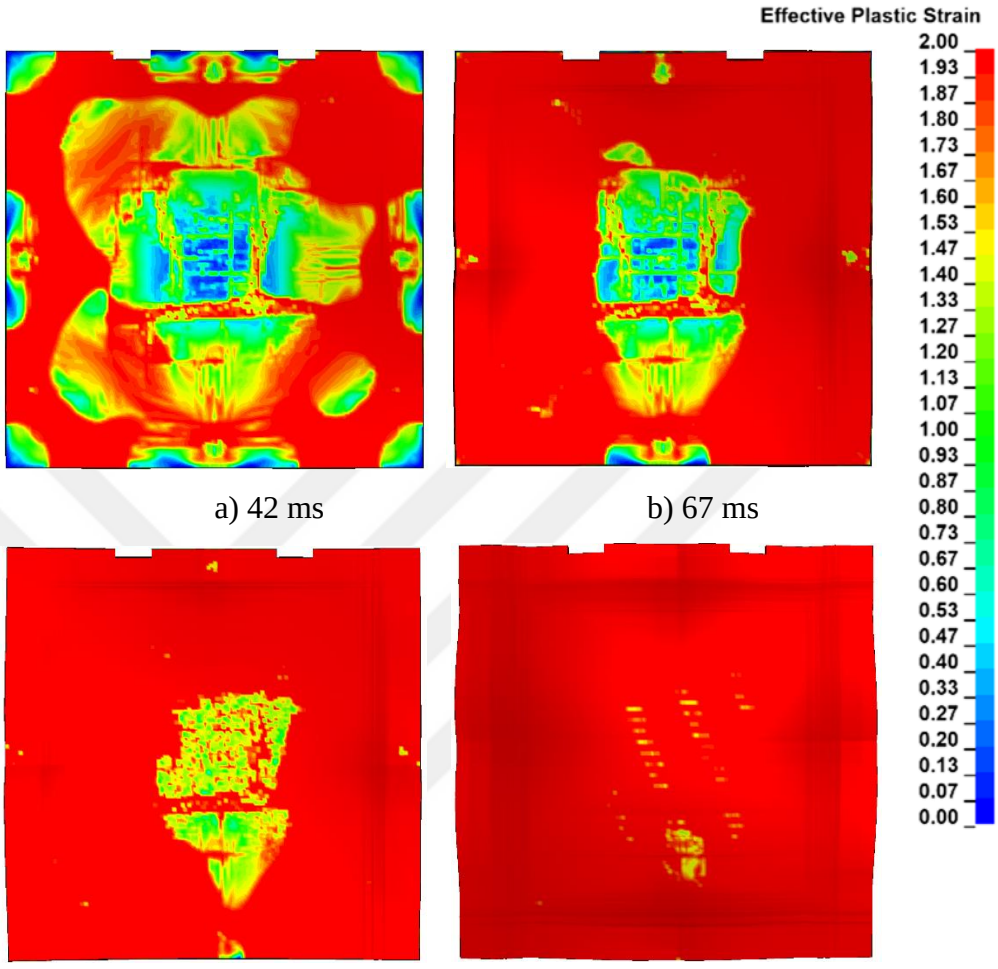


a) 42 ms b) 67 ms

c) 100 ms d) 400 ms

Figure 5.21. Numerical damage distributions of ST-M1+PVA specimen's front face, at a) 42 ms, b) 67 ms, c) 100 ms, and d) 400 ms

ST-M1+PVA specimen's front face was the side where the blast load was applied. The numerical damage distribution shows that the boundary locations are where the damage localizes then the damage moves toward the edges (Figure 5.21). An asymmetrical damage distribution is present due to the nature of the explicit analysis. The middle part of the specimen's front side shows damage at the later stages of blast loading towards 100 ms. At 400 ms, the specimen's front side is fully damaged. This founding corresponds with the experimental test phase as only one blast load was done to the ST-M1+PVA specimen.

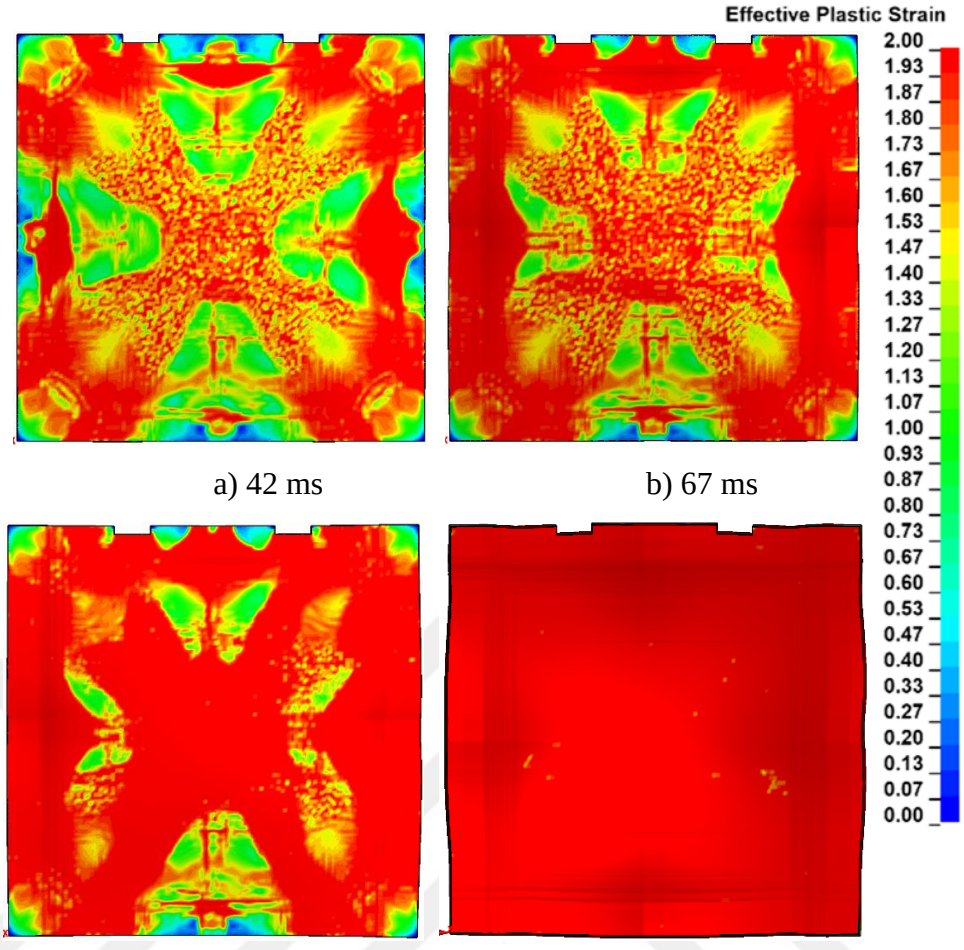


a) 42 ms b) 67 ms

c) 100 ms d) 400 ms

Figure 5.22. Numerical damage distributions of ST-M1+PVA specimen's back face, at a) 42 ms, b) 67 ms, c) 100 ms, and d) 400 ms

ST-M1+PVA specimen's back face (Figure 5.22) shows more symmetrical damage distribution compared to specimen's front side (Figure 5.21). At 42 ms, the corners and the boundary locations show localized damage leading toward specimen's middle. The numerical damage in the middle and along the diagonal path is more dispersed at the beginning of the blast loading. After 100 ms, these diagonal paths are fully damaged, and after 400 ms, specimens full back side is fully damaged as well. Again, the back side of the ST-M1+PVA specimen's numerical damage distribution shows the specimen is fully damaged after the first blast loading and energy capacity of the specimen is finalized, which corresponds with the experimental tests.

### 5.4.3. Numerical Damage and Experimental Crack Distribution Comparison

The experimental crack paths of ST-M2 and ST-M1+PVA specimens are given below. The blast was loaded at the front side of the specimen. The front side of ST-M2 specimen was not photographed after the first blast test.

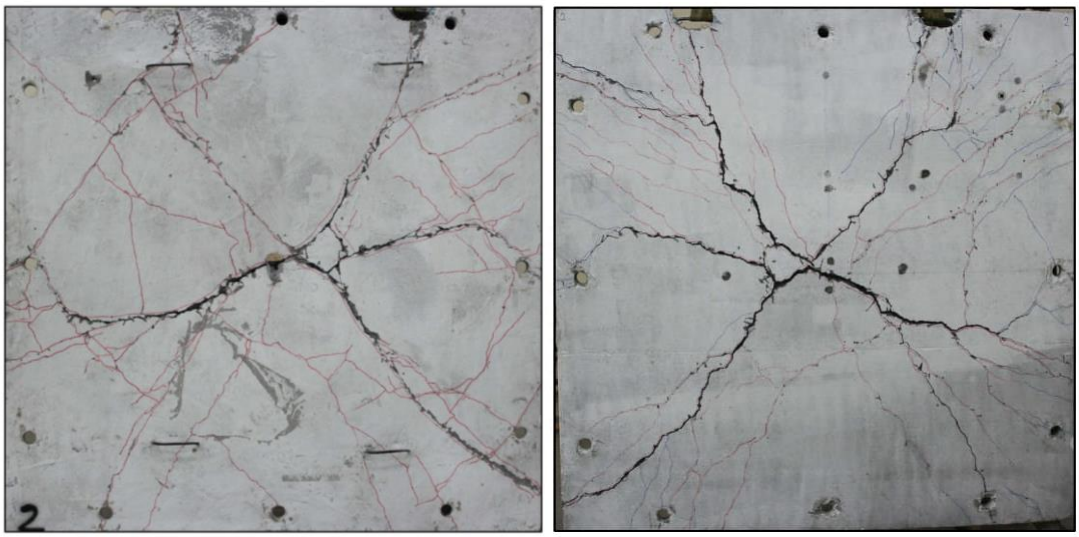


a) b)

Figure 5.23. Experimental crack profile of ST-M2 specimen, a) front (blast-loaded), and b) back faces (Alkabbani, 2021)

The experimental crack profile of ST-M2 specimen is presented in Figure 5.23. ST-M2 specimen was subjected to a blast loading resulting in a peak pressure of 43 kPa (Figure 5.4.a). Specimen's displacement time graphs were recorded and given in Figure 10 through Figure 14. Large diagonal cracks were observed after the blast load along with some hairline cracking. To test the full scope of ST-M2 specimen's blast resistance, another blast load with a peak pressure of 63 kPa was applied to the specimen. Only the first loading was used in the numerical study. The considered numerical results show that in conjunction with the experimental results, the specimen could endure another loading as it was not fully damaged after the first one. The front face of the specimen was photographed after the second blast loading.

a) b)

Figure 5.24. Experimental crack profile of ST-M1+PVA specimen, a) front (blast-loaded), and b) back faces (Alkabbani, 2021)

ST-M1+PVA specimen's blast test was concluded with one blast loading where the peak pressure was recorded as 47 kPa given in Figure 5.4.b. At the midpoint, the RLPT capacity was exceeded and the midpoint displacement of 117 mm was calculated through direct integration of the acceleration data. Wide diagonal cracks were observed as seen in Figure 5.24. Another blast load was not applied because of the high damage levels of the ST-M1+PVA specimen.

The experimental crack distribution was converted to crack paths with translucent bases with grey/black lines. Then, the translucent crack paths were placed on top of the final numerical damage for comparison. The crack distribution of the ST-M2 specimen's front side was captured after the second blast load. That was taken into account in the comparison process.

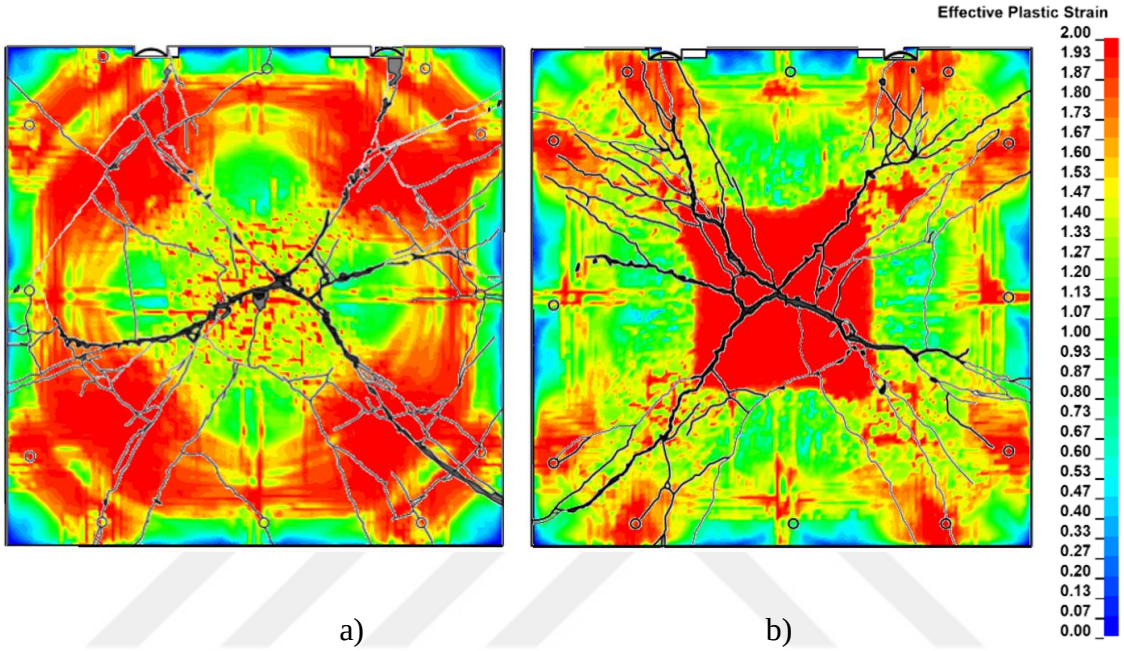


Figure 5.25. ST-M2 specimen's a) front and b) back face damage and crack distributions at the final stage at 450 ms

ST-M2 specimen's front face shows a circular damage distribution which coincides with the experimental circular crack paths (Figure 5.25). The wide diagonal cracks in the middle of the front face from experimental observations were not explicitly reflected in numerical damage distribution, though some damage could be from the second blast loading.

Diagonal cracks and the numerical damage fit well at the back face of the ST-M2 specimen. In the middle, numerical damage accumulates to a square section whereas the crack paths are more individual and wider. Overall, the damage is well represented at the back face compared to the front face which could be because of the lack of front crack paths after the first blast test. Additionally, the numerical damage is not excessive, like the experimental results, and the specimen could sustain another blast load as well.

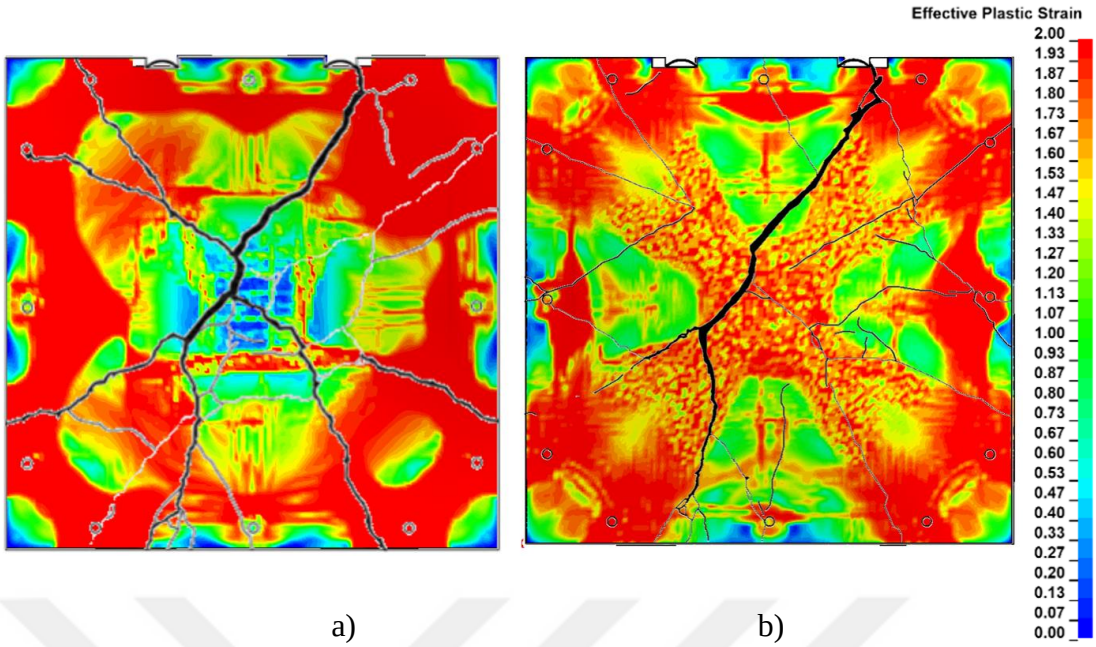


a) b)

Figure 5.26. ST-M1+PVA specimen's a) front and b) back face damage and crack distributions at the final stage at 42 ms

ST-M1+PVA specimen's crack and damage distribution was compared at 42 ms due to the substantial damage that had already occurred in the specimen by 400 ms. The numerical damage distribution of specimen's front side shows peripheral damage which coincides with the experimental crack paths (Figure 5.26). The diagonal cracks were observed in the numerical results in the later stages of the loading though not visible at 42 ms. ST-M1+PVA specimen's back face very clearly represents the diagonal cracks, coming from the boundary locations to the midpoint. The numerical damage distribution shows, in Figure 5.21 and Figure 5.22, that the specimen's blast resistance after the first blast loading is low and another blast test cannot be applied to the specimen. The same conclusion was reached with the experimental tests as well.

# CHAPTER 6

# CONCLUSIONS AND OUTLOOK

Current thesis proposes a new methodology for the numerical representation of fiber reinforced concrete (FRC) materials. A calibration method for fiber reinforced concrete (FRC) using Karagozian and Case (K&C) material model was presented. While the calibration method for a FRC material is very complex and laboursome, the current study uses a simpler and more effective methodology combining uniaxial direct tension test results and Deep Neural Networks (DNN). Calibrated K&C parameters were validated with experimental tests under static and dynamic conditions.

The following conclusions were drawn.

- The proposed methodology offers a practical and accurate representation of the FRC calibration method that can be used under different loading conditions. The use of a simple experimental test as DNN output and Python automation scripts provides fast and accurate calibration practice.
- The quasi-static and strain-rate influenced the behavior of FRC can be represented with a calibrated K&C material model. The parameters of the K&C material model offer flexibility to the user and the DNN approach replaces the need for experimental data fitting of these parameters. The tensile damage (b2) and damage distribution ($\lambda$ and $\eta$) parameters of K&C can provide the tensile strain-softening behavior of the FRC.
- Additional load and mass scaling studies could be concluded to eliminate the scattered behavior in force-displacement diagrams under bending loading. However, the proposed methodology gives the FRC damage, energy and force distribution very similar to experimental observations with a mesh size of 5 mm where here, the element size was selected with a mesh sensitivity study.
- K&C calibration with the proposed methodology can reflect the displacement and damage distribution under shock tube-induced blast

loading even though there are some discrepancies between the maximum displacement values.

- The calibration of a material model using a simple experimental test and DNN scheme can be used for varying the fiber types and percentages of FRC and hybrid fiber reinforced concrete materials. Additionally, other capable concrete material models can be calibrated with the proposed methodology.
- The K&C damage distribution of the FRC behavior was explicitly changed to reflect strain-softening behavior. Thus, the presence of strain-hardening behavior requires additional recalibration.
- Future study recommendations can be given for the calibration of the strain-hardening behavior of FRC through the DNN methodology.
- Additional future study recommendations could include applying the calibration method to the K&C strength surface and compression damage parameters, as well as other multiparameter material models in LS-DYNA.

# REFERENCES


Abadi, Martín, Paul Barham, Jianmin Chen, Zhifeng Chen, Andy Davis, Jeffrey Dean, Matthieu Devin, 2016. "TensorFlow: A System for Large-Scale Machine Learning." *Proceedings of the 12th Usenix Symposium on Operating Systems Design and Implementation, OSDI 2016*, 265–83.

Abbassi, Abderrahim, Niklas Römgens, Franz Ferdinand Tritschel, Nikolai Penner, and Raimund Rolfes. 2022. "Evaluation of Machine Learning Techniques for Structural Health Monitoring Using Ultrasonic Guided Waves under Varying Temperature Conditions." *Structural Health Monitoring-an International Journal*. https://doi.org/10.1177/14759217221107566.

Ahmad, Ayaz, Krisada Chaiyasarn, Furqan Farooq, Waqas Ahmad, Suniti Suparp, and Fahid Aslam. 2021. "Compressive Strength Prediction via Gene Expression Programming (Gep) and Artificial Neural Network (Ann) for Concrete Containing Rca." *Buildings* 11 (8): 324. https://doi.org/10.3390/buildings11080324.

Al-shawafi, Ali, Han Zhu, S. I. Haruna, Zhao Bo, Saleh Ahmed Laqsum, and Said Mirgan borito. 2023. "Experimental Study and Machine Learning Algorithms for Evaluating the Performance of U-Shaped Ultra-High Performance Reinforced Fiber Concrete under Static and Impact Loads." *Journal of Building Engineering* 70 (March): 106389. https://doi.org/10.1016/j.jobe.2023.106389.

Ali, Nur Fahriza Mohd, Ahmad Farhan Mohd Sadullah, Anwar P P Abdul Majeed, Mohd Azraai Mohd Razman, Muhammad Aizzat Bin Zakaria, and Ahmad Fakhri Ab. Nasir. 2021. "Travel Mode Choice Modeling: Predictive Efficacy between Machine Learning Models and Discrete Choice Model." *The Open Transportation Journal*.

Alkabbani, Mouhammed Jalal. 2021. "Structural Behavior of Hybrid-Fiber Reinforced Concrete Panels Under Blast Loads Using Shock Tubes" no. July.

Attard, M. M., and S. Setunge. 1996. "Stress-Strain Relationship of Confined and Unconfined Concrete." *ACI Materials Journal*. https://doi.org/10.14359/9847.

Belytschko, Ted, and Mark O. Neal. 1991. “Contact-impact by the Pinball Algorithm with Penalty and Lagrangian Methods.” *International Journal for Numerical Methods in Engineering* 31 (3): 547–72. https://doi.org/10.1002/nme.1620310309.

Bruhl, Jakob C. 2015. “Behavior and Design of Steel-Plate Composite (SC) Walls for Blast Loads,” 327.

Burrell, Russell. 2012. “Performance of Steel Fibre Reinforced Concrete Columns under Shock Tube Induced Shock Wave Loading,” no. August: 248.

Caggiano, Antonio, Serena Gambarelli, Enzo Martinelli, Nicola Nisticò, and Marco Pepe. 2016. “Experimental Characterization of the Post-Cracking Response in Hybrid Steel/Polypropylene Fiber-Reinforced Concrete.” *Construction and Building Materials* 125 (July 2018): 1035–43. https://doi.org/10.1016/j.conbuildmat.2016.08.068.

Çankaya, Mehmet Alper, and Çetin Akan. 2023. “An Experimental and Numerical Investigation on the Bending Behavior of Fiber Reinforced Concrete Beams.” *Turkish Journal of Civil Engineering* 34 (1): 59–78. https://doi.org/10.18400/tjce.1209152.

Cekić, I, and K Çavdar. 2022. “Detection of the Cracks in Metal Sheets Using Convolutional Neural Network (CNN).” *Null*. https://doi.org/null.

Çetin, Fatma Şirin. 2020. “Mechanical Behavior Of Hybrid Fiber Reinforced Concrete Under Direct Tension,” no. June.

Chamekh, A., H. Bel Hadj Salah, and R. Hambli. 2009. “Inverse Technique Identification of Material Parameters Using Finite Element and Neural Network Computation.” *International Journal of Advanced Manufacturing Technology* 44 (1–2): 173–79. https://doi.org/10.1007/s00170-008-1809-6.

Chasioti, Stamatina G., and Frank J. Vecchio. 2017. “Effect of Fiber Hybridization on Basic Mechanical Properties of Concrete.” *ACI Structural Journal* 114 (3): 375–84. https://doi.org/10.14359/51689479.

Chou, Jui-Sheng, Chih-Fong Tsai, Anh-Duc Pham, and Yu-Hsin Lu. 2014. “Machine

Learning in Concrete Strength Simulations: Multi-Nation Data Analytics." *Construction and Building Materials* 73 (December): 771–80. https://doi.org/10.1016/j.conbuildmat.2014.09.054.

Dozat, Timothy. 2016. "Incorporating Nesterov Momentum into Adam." *International Conference on Learning Representations Workshops*.

Elshafey, Ahmed A., Nabil Dawood, H. Marzouk, and M. Haddara. 2013. "Crack Width in Concrete Using Artificial Neural Networks." *Engineering Structures* 52: 676–86. https://doi.org/10.1016/j.engstruct.2013.03.020.

Entezami, Alireza, Carlo De Michele, C De Michele, Ali Nadir Arslan, and Bahareh Behkamal. 2022. "Detection of Partially Structural Collapse Using Long-Term Small Displacement Data from Satellite Images." *Sensors*. https://doi.org/10.3390/s22134964.

Entezami, Alireza, Hashem Shariatmadar, and Carlo De Michele. 2022. "Non-Parametric Empirical Machine Learning for Short-Term and Long-Term Structural Health Monitoring." *Structural Health Monitoring* 21 (6): 2700–2718. https://doi.org/10.1177/14759217211069842.

Farnam, Yaghoob, Soheil Mohammadi, and Mohammad Shekarchi. 2010. "Experimental and Numerical Investigations of Low Velocity Impact Behavior of High-Performance Fiber-Reinforced Cement Based Composite." *International Journal of Impact Engineering* 37 (2): 220–29. https://doi.org/10.1016/j.ijimpeng.2009.08.006.

Géron, Aurélien. 2017. *Hands-on Machine Learning with Scikit-Learn , Keras & TensorFlow*. Sebastopol, CA: O'Reilly Media.

Goyal, Vinay K, E R Johnson, and Carlos G Dávila. 2004. "Irreversible Constitutive Law for Modeling the Delamination Process Using Interfacial Surface Discontinuities." *Composite Structures* 65: 289–305.

Grigorescu, Sorin Mihai, Bogdan Trasnea, Tiberiu T Cocias, and Gigel Macesanu. 2019. "A Survey of Deep Learning Techniques for Autonomous Driving." *Journal of Field Robotics* 37: 362–86.

Gu, Shihao, Bryan T Kelly, and Dacheng Xiu. 2018. “Empirical Asset Pricing Via Machine Learning.” *NBER Working Paper Series*.

Gupta, Tanuja, and Meesala Chakradhara Rao. 2022. “Prediction of Compressive Strength of Geopolymer Concrete Using Machine Learning Techniques.” *Structural Concrete* 23 (5): 3073–90. https://doi.org/10.1002/suco.202100354.

Hamouche, Elia, and Evripides G Loukaides. 2018. “Classification and Selection of Sheet Forming Processes with Machine Learning.” *International Journal of Computer Integrated Manufacturing*. https://doi.org/10.1080/0951192x.2018.1429668.

Herrmann, H., R. Boris, O. Goidyk, and A. Braunbrück. 2019. “Variation of Bending Strength of Fiber Reinforced Concrete Beams Due to Fiber Distribution and Orientation and Analysis of Microstructure.” *IOP Conference Series: Materials Science and Engineering* 660 (1). https://doi.org/10.1088/1757-899X/660/1/012059.

Hürkamp, André, Sebastian Gellrich, Antal Dér, Christoph Herrmann, Klaus Dröder, and Sebastian Thiede. 2021. “Machine Learning and Simulation-Based Surrogate Modeling for Improved Process Chain Operation.” *The International Journal of Advanced Manufacturing Technology*. https://doi.org/10.1007/s00170-021-07084-5.

Ibrahim, Ahmed, Hani Salim, and Ian Flood. 2011. “Damage Prediction for RC Slabs under Near-Field Blasts Using Artificial Neural Network.” *International Journal of Protective Structures* 2 (3): 315–32. https://doi.org/10.1260/2041-4196.2.3.315.

Jacques, Eric, Alan Lloyd, and Murat Saatcioglu. 2013. “Predicting Reinforced Concrete Response to Blast Loads.” *Canadian Journal of Civil Engineering* 40 (5): 427–44. https://doi.org/10.1139/l2012-014.

Jacques, Eric, and Murat Saatcioglu. 2020. “High-Strain-Rate Response of Reinforced Concrete Lap-Spliced Beams.” *Journal of Structural Engineering* 146 (1): 04019165. https://doi.org/10.1061/(asce)st.1943-541x.0002463.

Karypidis, Dimitrios. 2019. “Structural Health Monitoring of Concrete Elements Using

Deep Machine Learning," 61. http://studentarbeten.chalmers.se/publication/256959-structural-health-monitoring-of-concrete-elements-using-deep-machine-learning.

Kaur, Kirandeep, Akhil Garg, Xujian Cui, Surinder Singh, and Bijaya Ketan Panigrahi. 2021. "Deep Learning Networks for Capacity Estimation for Monitoring <scp>SOH</Scp> of Li-ion Batteries for Electric Vehicles." *International Journal of Energy Research* 45 (2): 3113–28. https://doi.org/10.1002/er.6005.

Kina, Ceren, Kazim Turk, and Harun Tanyildizi. 2022. "Estimation of Strengths of Hybrid FR-SCC by Using Deep-Learning and Support Vector Regression Models." *Structural Concrete* 23 (5): 3313–30. https://doi.org/10.1002/suco.202100622.

Kingma, Diederik P., and Jimmy Lei Ba. 2015. "Adam: A Method for Stochastic Optimization." *3rd International Conference on Learning Representations, ICLR 2015 - Conference Track Proceedings*, 1–15.

Koch, David, and André Haufe. 2019. "First Steps towards Machine-Learning Supported Material Parameter Identification." *12th European LS-DYNA Conference*.

Kohar, Christopher P., Lars Greve, Tom K. Eller, Daniel S. Connolly, and Kaan Inal. 2021. "A Machine Learning Framework for Accelerating the Design Process Using CAE Simulations: An Application to Finite Element Analysis in Structural Crashworthiness." *Computer Methods in Applied Mechanics and Engineering* 385: 114008. https://doi.org/10.1016/j.cma.2021.114008.

Kong, Xiangzhen, Qin Fang, Q.M. Li, Hao Wu, and John E. Crawford. 2017. "Modified K&C Model for Cratering and Scabbing of Concrete Slabs under Projectile Impact." *International Journal of Impact Engineering* 108 (October): 217–28. https://doi.org/10.1016/j.ijimpeng.2017.02.016.

Kong, Xiangzhen, Qin Fang, Hao Wu, and Yong Peng. 2016. "Numerical Predictions of Cratering and Scabbing in Concrete Slabs Subjected to Projectile Impact Using a Modified Version of HJC Material Model." *International Journal of Impact Engineering* 95: 61–71. https://doi.org/10.1016/j.ijimpeng.2016.04.014.

Kristoffersen, Martin, Karoline Osnes, Sondre Rydtun Haug, Vegard Aune, and Tore Børvik. 2016. “Shock Tube Testing and Numerical Simulations of Concrete Slabs.” *1st International Conference on Impact Loading of Structures and Materials*, no. May: 4–8.

Kristoffersen, Martin, Jon Eide Pettersen, Vegard Aune, and Tore Børvik. 2018. “Experimental and Numerical Studies on the Structural Response of Normal Strength Concrete Slabs Subjected to Blast Loading.” *Engineering Structures* 174 (July): 242–55. https://doi.org/10.1016/j.engstruct.2018.07.022.

Kucewicz, Michał, Paweł Baranowski, Roman Gieleta, and Jerzy Małachowski. 2022. “Investigation of Dolomite’ Rock Brittle Fracture Using Fully Calibrated Karagozian Case Concrete Model.” *International Journal of Mechanical Sciences* 221 (March). https://doi.org/10.1016/j.ijmecsci.2022.107197.

Kucewicz, Michał, Paweł Baranowski, and Jerzy Małachowski. 2020. “Determination and Validation of Karagozian-Case Concrete Constitutive Model Parameters for Numerical Modeling of Dolomite Rock.” *International Journal of Rock Mechanics and Mining Sciences* 129 (March). https://doi.org/10.1016/j.ijrmms.2020.104302.

Kurumatani, Mao, Kenjiro Terada, Junji Kato, Takashi Kyoya, and Kazuo Kashiyama. 2016. “An Isotropic Damage Model Based on Fracture Mechanics for Concrete.” *Engineering Fracture Mechanics* 155: 49–66.

Lee, Jin Young, Hassan Aoude, Young Soo Yoon, and Denis Mitchell. 2020. “Impact and Blast Behavior of Seismically-Detailed RC and UHPFRC-Strengthened Columns.” *International Journal of Impact Engineering* 143 (July 2019): 103628. https://doi.org/10.1016/j.ijimpeng.2020.103628.

Lee, Jin Young, Hyun Oh Shin, Doo Yeol Yoo, and Young Soo Yoon. 2018. “Structural Response of Steel-Fiber-Reinforced Concrete Beams under Various Loading Rates.” *Engineering Structures* 156 (November 2017): 271–83. https://doi.org/10.1016/j.engstruct.2017.11.052.

Leutbecher, Torsten, and Jan Rebling. 2019. “Predicting the Postcracking Strength of Ultra-High Performance Fiber Reinforced Concrete by Means of Three-Point Bending Tests According to EN 14651.” *Structural Concrete* 20 (6): 2081–95.

https://doi.org/10.1002/suco.201900070.

Levi-Hevroni, David, Eytan Kochavi, Boaz Kofman, Shimon Gruntman, and Oren Sadot. 2018. “Experimental and Numerical Investigation on the Dynamic Increase Factor of Tensile Strength in Concrete.” *International Journal of Impact Engineering* 114 (December 2017): 93–104. https://doi.org/10.1016/j.ijimpeng.2017.12.006.

Li, Victor C, Shuxin Wang, and Cynthia Wu. 2001. “Tensile Strain - Hardening Behavior of Polyvinyl Alcohol Engineered Cementitious Composite (PVA-ECC) in Engineering.” *Aci Materials Journal*. https:// doi.org/10.14359/10851.

Lin, Xiaoshan, and Rebecca J. Gravina. 2017. “An Effective Numerical Model for Reinforced Concrete Beams Strengthened with High Performance Fibre Reinforced Cementitious Composites.” *Materials and Structures* 50 (5): 212. https://doi.org/10.1617/s11527-017-1085-8.

Liusko, Timofei. 2021. “An Artificial Intelligence Framework for Vehicle Crashworthiness Design By.”

Lloyd, Alan. 2011. “Blast Retrofit of Reinforced Concrete Columns,” no. February.

LSTC. 2007. *LS-DYNA Keyword User ’ s Manual: Volume II Material Models*. Vol. II. https://doi.org/10.1016/j.chemosphere.2011.02.019.

Maalej, Mohamed, S T Quek, Ser Tong Quek, and Jing Zhang. 2005. “Behavior of Hybrid-Fiber Engineered Cementitious Composites Subjected to Dynamic Tensile Loading and Projectile Impact.” *Journal of Materials in Civil Engineering*. https://doi.org/10.1061/ (asce)0899-1561(2005)17:2(143).

Maazoun, Azer, Stijn Matthys, Stijn Matthys, Bachir Belkassem, David Lecompte, and John Vantomme. 2018. “Numerical Analysis of Retrofitted RC Slabs with CFRP Strips under Blast Loading.” *Null*. https://doi.org/null.

Magallanes, Joseph M., Youcai Wu, L. Javier Malvar, and John E. Crawford. 2010.

"Recent Improvements to Release III of the K&C Concrete Model." *11th International LS-DYNA User Conference*, no. 1: 37–48. https://www.dynalook.com/international-conf-2010/Simulation-1-4.pdf.

Mahajan, Lomesh, Sariputt Bhagat, and Eng Struct. 2022. "An Artificial Neural Network for the Prediction of the Strength of Supplementary Cementitious Concrete." *Research on Engineering Structures and Materials* 8 (2): 421–30. https://doi.org/10.17515/resm2022.341st0918tn.

Malvar, L.Javier, John E. Crawford, James W. Wesevich, and Don Simons. 1997. "A Plasticity Concrete Material Model for DYNA3D." *International Journal of Impact Engineering* 19 (9): 847–73. https://doi.org/10.1016/S0734-743X(97)00023-7.

Manual, Keyword User S. 2013. *Keyword User ' S Manual Volume I*. Vol. I.

Mao, Lei, Stephanie Barnett, David Begg, Graham Schleyer, and Gavin Wight. 2014. "Numerical Simulation of Ultra High Performance Fibre Reinforced Concrete Panel Subjected to Blast Loading." *International Journal of Impact Engineering* 64 (February): 91–100. https://doi.org/10.1016/j.ijimpeng.2013.10.003.

Mardalizad, Aria, Marco Caruso, Andrea Manes, and Marco Giglio. 2019. "Investigation of Mechanical Behaviour of a Quasi-Brittle Material Using Karagozian and Case Concrete (KCC) Model." *Journal of Rock Mechanics and Geotechnical Engineering* 11 (6): 1119–37. https://doi.org/10.1016/j.jrmge.2019.01.005.

Mardalizad, Aria, Andrea Manes, and Marco Giglio. 2017. "The Numerical Modelling of a Middle Strength Rock Material under Flexural Test by Finite Element Method-Coupled to-SPH." *Procedia Structural Integrity*. https://doi.org/10.1016/j.prostr.2017.04.050.

Mardalizad, Aria, Riccardo Scazzosi, Andrea Manes, and Marco Giglio. 2018. "Testing and Numerical Simulation of a Medium Strength Rock Material under Unconfined Compression Loading." *Journal of Rock Mechanics and Geotechnical Engineering*. https://doi.org/10.1016/j.jrmge.2017.11.009.

Markovich, Natalia, Eytan Kochavi, and Gabi Ben-Dor. 2011. “An Improved Calibration of the Concrete Damage Model.” *Finite Elements in Analysis and Design* 47 (11): 1280–90. https://doi.org/10.1016/j.finel.2011.05.008.

Martinelli, Enzo, Antonio Caggiano, and Hernán Xargay. 2015. “An Experimental Study on the Post-Cracking Behaviour of Hybrid Industrial/Recycled Steel Fibre-Reinforced Concrete.” *Construction and Building Materials*. https://doi.org/10.1016/j.conbuildmat.2015.07.007.

Masi, Filippo, Ioannis Stefanou, Paolo Vannucci, and Victor Maffi-Berthier. 2021. “Thermodynamics-Based Artificial Neural Networks for Constitutive Modeling.” *Journal of the Mechanics and Physics of Solids* 147 (February): 104277. https://doi.org/10.1016/j.jmps.2020.104277.

Meißner, Paul, Hagen Watschke, Jens Winter, and Thomas Vietor. 2020. “Artificial Neural Networks-Based Material Parameter Identification for Numerical Simulations of Additively Manufactured Parts by Material Extrusion.” *Polymers* 12 (12): 2949. https://doi.org/10.3390/polym12122949.

Meißner, Paul, Jens Winter, and Thomas Vietor. 2022. *Methodology for Neural Network-Based Material Card Calibration Using LS-DYNA MAT_187_SAMP-1 Considering Failure with GISSMO*. *Materials*. Vol. 15. https://doi.org/10.3390/ma15020643.

Misaka, Takashi, Jonny Herwan, Seisuke Kano, Hiroyuki Sawada, and Yoshiyuki Furukawa. 2020. “Deep Neural Network-Based Cost Function for Metal Cutting Data Assimilation.” *International Journal of Advanced Manufacturing Technology* 107 (1–2): 385–98. https://doi.org/10.1007/s00170-020-04984-w.

Mitchell, Tim. 1997. “Machine Learning.” *Machine Learning* 45 (13): 40–48.

Mudadu, Antonio, Giuseppe Tiberti, Giovanni A. Plizzari, and Alessandro Morbi. 2019. “Post-Cracking Behavior of Polypropylene Fiber Reinforced Concrete under Bending and Uniaxial Tensile Tests.” *Structural Concrete* 20 (4): 1411–24. https://doi.org/10.1002/suco.201800224.

Naaman, Antoine E, and Hans W Reinhardt. 2007. “Proposed Classification of HPFRC

Composites Based on Their Tensile Response." *Materials and Structures*. https://doi.org/10.1617/s11527-006-9103-2.

Nawar, M, H Salim, B Lusk, and S Kiger. 2015. "Modeling and Shock Tube Testing of Architectural Glazing Systems for Blast Resistance." *Journal of Structural Engineering* 141 (7): 04014174. https://doi.org/10.1061/(ASCE)ST.1943-541X.0001130.

Nguyen, Tuan Ngoc. 2019. "A Novel Experimental-Computational-Data Driven Framework for Advancing the Understanding of Lightweight Concrete," no. November.

Oettel, Vincent, Markus Schulz, and Michael Haist. 2022. "Empirical Approach for the Residual Flexural Tensile Strength of Steel Fiber-Reinforced Concrete Based on Notched Three-Point Bending Tests." *Structural Concrete* 23 (2): 993–1004. https://doi.org/10.1002/suco.202100565.

Özcan, D. Mehmet, Alemdar Bayraktar, Abdurrahman Şahin, Tefaruk Haktanir, and Temel Türker. 2009. "Experimental and Finite Element Analysis on the Steel Fiber-Reinforced Concrete (SFRC) Beams Ultimate Behavior." *Construction and Building Materials* 23 (2): 1064–77. https://doi.org/10.1016/j.conbuildmat.2008.05.010.

Passarello, Marco. 2018. "Parameter Identification on a Carbon-Fiber Reinforced Polymer Using LS-OPT." *Null*. https://doi.org/null.

Pitz, Emil, Sean Rooney, and Kishore Pochiraju. 2023. "Estimation of Spatial Uncertainty in Material Property Distributions within Heterogeneous Structures Using Optimized Convolutional Neural Networks." *Engineering Applications of Artificial Intelligence* 117 (October 2022): 105603. https://doi.org/10.1016/j.engappai.2022.105603.

Rahmani, Tara, Behnam Kiani, Mohammad Shekarchi, and Abdollah Safari. 2012. "Statistical and Experimental Analysis on the Behavior of Fiber Reinforced Concretes Subjected to Drop Weight Test." *Construction and Building Materials*. https://doi.org/10.1016/j.conbuildmat.2012.07.068.

Rasmussen, Jennifer, Gholami, Shayan, Zare-Rami Keyvan, Kim Yong-Rak, 2020. "Evaluation of Concrete Models in LS-DYNA to Develop a Mash Test Level 6 (TL-6) Barrier System" 6.

Ribeiro, Antônio H., Koen Tiels, Luis A. Aguirre, and Thomas B. Schön. 2019. "Beyond Exploding and Vanishing Gradients: Analysing RNN Training Using Attractors and Smoothness." http://arxiv.org/abs/1906.08482.

Saatçi, Selçuk, and Baturay Batarlar. 2017. "Behavior of Steel Fiber Reinforced Concrete Beams without Stirrups." *Journal of the Faculty of Engineering and Architecture of Gazi University* 32 (4): 1143–54. https://doi.org/10.17341/gazimmfd.369512.

Sarmadi, Hassan, Alireza Entezami, Bahareh Behkamal, and Carlo De Michele. 2022. "Partially Online Damage Detection Using Long-Term Modal Data under Severe Environmental Effects by Unsupervised Feature Selection and Local Metric Learning." *Journal of Civil Structural Health Monitoring*. https://doi.org/10.1007/s13349-022-00596-y.

Sarmadi, Hassan, and Abbas Karamodin. 2020. "A Novel Anomaly Detection Method Based on Adaptive Mahalanobis-Squared Distance and One-Class KNN Rule for Structural Health Monitoring under Environmental Effects." *Mechanical Systems and Signal Processing*. https://doi.org/10.1016/j.ymssp.2019.106495.

Sarra Aloui. 2020. "Bending Behaviour of a Hybrid Fiber Reinforced Concrete Beams," no. December.

Schuler, Harald, Christoph Mayrhofer, and Klaus Thoma. 2006. "Spall Experiments for the Measurement of the Tensile Strength and Fracture Energy of Concrete at High Strain Rates." *International Journal of Impact Engineering* 32 (10): 1635–50. https://doi.org/10.1016/j.ijimpeng.2005.01.010.

Schulte, Robin, Cavid Karca, Richard Ostwald, and Andreas Menzel. 2022. "Machine Learning-Assisted Parameter Identification for Constitutive Models Based on Concatenated Loading Path Sequences." *European Journal of Mechanics - A/Solids* 98: 104854. https://doi.org/10.1016/j.euromechsol.2022.104854.

Shehata, Hesham M., Yasser S. Mohamed, Mohamed Abdellatif, and Taher H. Awad. 2018. “Crack Width Estimation Using Feed and Cascade Forward Back Propagation Artificial Neural Networks.” *Key Engineering Materials* 786 KEM: 293–301. https://doi.org/10.4028/www.scientific.net/KEM.786.293.

Sherif, Mohtady, Hesham Othman, Hesham Marzouk, and Hassan Aoude. 2022. “An Experimentally Validated Numerical Analysis of UHP-FRC Subjected to Blast Loading.” *International Journal of Protective Structures*. https://doi.org/10.1177/20414196221120512.

Sorelli, Luca, Alberto Meda, and Giovanni Plizzari. 2005. “Bending and Uniaxial Tensile Tests on Concrete Reinforced with Hybrid Steel Fibers.” *Journal of Materials in Civil Engineering*. https://doi.org/10.1061/(asce)0899-1561(2005)17:5(519).

Tayfur, Sena, Selçuk Saatcı, and Ninel Alver. 2018. “Determination of the Behavior of Steel Fiber Reinforced Concrete Beams without Stirrups under Bending by Nonlinear Finite Element Analysis.” *Pamukkale University Journal of Engineering Sciences* 24 (3): 397–402. https://doi.org/10.5505/pajes.2017.98700.

Thai, Duc Kien, Duy Liem Nguyen, and Duy Duan Nguyen. 2020. “A Calibration of the Material Model for FRC.” *Construction and Building Materials* 254: 119293. https://doi.org/10.1016/j.conbuildmat.2020.119293.

Thiagarajan, Ganesh, Anirudha V. Kadambi, Stephen Robert, and Carol F. Johnson. 2015. “Experimental and Finite Element Analysis of Doubly Reinforced Concrete Slabs Subjected to Blast Loads.” *International Journal of Impact Engineering* 75: 162–73. https://doi.org/10.1016/j.ijimpeng.2014.07.018.

Tian, Huiwen, Zhen Zhou, Yang Wei, and Yongquan Wang. 2021. “Behavior of FRP-Confined Ultra-High Performance Concrete under Eccentric Compression.” *Composite Structures* 256 (August 2020): 113040. https://doi.org/10.1016/j.compstruct.2020.113040.

Tu, Zhenguo, and Yong Lu. 2009. “Evaluation of Typical Concrete Material Models Used in Hydrocodes for High Dynamic Response Simulations.” *International Journal of Impact Engineering* 36 (1): 132–46. https://doi.org/

10.1016/j.ijimpeng.2007.12.010.

Vellido, Alfredo. 2020. “The Importance of Interpretability and Visualization in Machine Learning for Applications in Medicine and Health Care.” *Neural Computing and Applications*, 1–15.

Wang, Z. L., J. Wu, and J. G. Wang. 2010. “Experimental and Numerical Analysis on Effect of Fibre Aspect Ratio on Mechanical Properties of SRFC.” *Construction and Building Materials* 24 (4): 559–65. https://doi.org/10.1016/j.conbuildmat.2009.09.009.

Weerheijm, J., and J. Cam. Van Doormaal. 2007. “Tensile Failure of Concrete at High Loading Rates: New Test Data on Strength and Fracture Energy from Instrumented Spalling Tests.” *International Journal of Impact Engineering* 34 (3): 609–26. https://doi.org/10.1016/j.ijimpeng.2006.01.005.

Weg, B. P. van de, L. Greve, M. Andres, T. K. Eller, and B. Rosic. 2021. “Neural Network-Based Surrogate Model for a Bifurcating Structural Fracture Response.” *Engineering Fracture Mechanics* 241 (March 2020): 107424. https://doi.org/10.1016/j.engfracmech.2020.107424.

Weichert, Dorina, Patrick Link, Anke Stoll, Stefan Rüping, Steffen Ihlenfeldt, and Stefan Wrobel. 2019. “A Review of Machine Learning for the Optimization of Production Processes.” *International Journal of Advanced Manufacturing Technology* 104 (5–8): 1889–1902. https://doi.org/10.1007/s00170-019-03988-5.

Wille, K., S. El-Tawil, and A. E. Naaman. 2014. “Properties of Strain Hardening Ultra High Performance Fiber Reinforced Concrete (UHP-FRC) under Direct Tensile Loading.” *Cement and Concrete Composites* 48: 53–66. https://doi.org/10.1016/j.cemconcomp.2013.12.015.

Wu, Shaoju, Wei Zhao, and Songbai Ji. 2022. “Real-Time Dynamic Simulation for Highly Accurate Spatiotemporal Brain Deformation from Impact.” *Computer Methods in Applied Mechanics and Engineering*. https://doi.org/10.1016/j.cma.2022.114913.

Wu, Youcai, John E. Crawford, Shengrui Lan, and Joseph M. Magallanes. 2014.

"Validation Studies for Concrete Constitutive Models with Blast Test Data." *13th International LS-DYNA Users Conference*, 1–12.

Wu, Youcai, John E Crawford, and Joseph m. Magallanes. 2012. "Performance of LS-DYNA Concrete Constitutive Models." *12th International LS-DYNA Users Conference*, no. 1: 1–14.

Wu, Youcai, and John E.Crawford. 2015. "Numerical Modeling of Concrete Using a Partially Associative Plasticity Model." *Journal of Engineering Mechanics* 141 (12): 1–24. https://doi.org/10.1061/(ASCE)EM.1943-7889.0000952.

Xu, L. Y., H. Xu, and H. M. Wen. 2019. "On the Penetration and Perforation of Concrete Targets Struck Transversely by Ogival-Nosed Projectiles - a Numerical Study." *International Journal of Impact Engineering* 125 (June 2018): 39–55. https://doi.org/10.1016/j.ijimpeng.2018.11.001.

Xu, Shenchun, Pengtao Wu, and Chengqing Wu. 2020. "Calibration of KCC Concrete Model for UHPC against Low-Velocity Impact." *International Journal of Impact Engineering* 144 (May): 103648. https://doi.org/10.1016/j.ijimpeng.2020.103648.

Yoo, Yeongmin, Chang-Kyu Park, and Jongsoo Lee. 2022. "Deep Learning-Based Efficient Metamodeling via Domain Knowledge-Integrated Designable Data Augmentation with Transfer Learning: Application to Vehicle Crash Safety." *Structural and Multidisciplinary Optimization*. https://doi.org/10.1007/s00158-022-03290-1.

Yuan, Siqi, Zhao Liu, Teng Tong, and Chung C. Fu. 2022. "Bond Behaviors between UHPC and Normal-Strength Concrete: Experimental Investigation and Database Construction." *Journal of Materials in Civil Engineering* 34 (1): 1–16. https://doi.org/10.1061/(asce)mt.1943-5533.0004038.

Zheng, Dong, Rongxing Wu, Muhammad Sufian, Nabil Ben Kahla, Miniar Atig, Ahmed Farouk Deifalla, Oussama Accouche, and Marc Azab. 2022. "Flexural Strength Prediction of Steel Fiber-Reinforced Concrete Using Artificial Intelligence." *Materials* 15 (15). https://doi.org/10.3390/ma15155194.

# VITA

**Name – Surname:** Yonca YAŞAYANLAR

## Educational Information:

| Graduation Degree | Institution | Graduation Year |
|---|---|---|
| BSc. | Celal Bayar University | 2011 |
| MSc. | Izmir Institute of Technology | 2014 |
| PhD. | Izmir Institute of Technology | 2023 |

## Publications:

Yaşayanlar Y., Saatci S., Aloui S., 2021. ”Experimental and Numerical Investigation of Hybrid Fiber Reinforced Concrete Beams Under Three and Four Point Bending”. 14th International Congress on Advances in Civil Engineering

Yaşayanlar Y., Saatci S., 2021. ”Modeling of Reinforced Concrete Panels Under Blast Loading ”. 2nd International Workshop on Plasticity, Damage and Fracture of Engineering Materials

Saatci S., Yaşayanlar S., Yaşayanlar Y., Batarlar B., 2019. ”Celik fiber katkısının farklı boyuna donatı oranına sahip betonarme dosemelerin zımbalama davranısı”. Gazi University Faculty of Engineering and Architecture Magazine

Saatci S., Batarlar B., Yaşayanlar (Arsan) Y., Yaşayanlar S., 2015. ”Darbe Yuklerine Maruz Kalan Dosemelerin Davranısı ve Kayma Donatısının Darbe Davranısına Etkisi”. National Structural Mechanics Laboratories Meeting

Saatci S., Yaşayanlar (Arsan) Y., 2014. ”Effects of Shear Reinforcement on the Behavior of Reinforced Concrete Slabs Subjected to Impact Loading”. 11th International Congress on Advances in Civil Engineering